Relatório Final de Pesquisa
CNPq – PVE 2014

Fabrication of hybrid SiC and nanodiamond particles with immobilized photoreceptors and their bio-analytical application for controlled drug delivery

Researcher team:
Prof. Volodymyr Zaitsev (coordinator)
Prof. Sabine Szunerits (PVE)
Prof. Omar Pandoli
Prof. Luiz Alves
Dr. Eloah Pereira Ávila (PDJ)
Dr. Mykhailo Nazarkovskyi (PDJ)
Miss Olena Artiushenko (PhD student)
Miss Albina Mikhraliieva (PhD student)
Mr. Volodymyr Turcheniuk (PhD student)
Mr. Dmytro Korytko (PhD student)
    Collaborators:
Sergey Alekseev, Manakamana Khanal,
Alexandre Barras, Rabah Boukherroub, and
Aloysius Siriwardena, Kostiantyn Turcheniuk

Rio de Janeiro, janeiro de 2019

1. Content

2. Resumo

O projeto é sobre a preparação de novas nanopartículas com nenhuma ou menos citotoxicidade. É uma das principais direções no desenvolvimento de novos sistemas para a entrega de medicamentos.

As nanopartículas têm sido utilizados em vastas aplicações, desde o armazenamento de energia até a biotecnologia. A natureza versátil destes materiais está ligada à possibilidade de adaptar de forma controlada as propriedades físicas e químicas dos materiais. Materiais inorgânicos demonstraram apresentar estabilidade química e estrutural superior em comparação com materiais orgânicos. Assim, materiais nanoestruturados inorgânicos ganharam considerável importância em diversas aplicações biotecnológicas relacionadas a materiais compósitos para implantes, sensores e liberação de fármacos. Os sistemas de administração de fármacos desempenham vários papéis, tais como melhorar a fraca solubilidade, aumentar a estabilidade in vivo e otimizar a biodistribuição e a farmacocinética dos medicamentos. Eles também podem ser usados para direcionar tecidos específicos e tipos de células através da funcionalização apropriada. No entanto, sua aplicação biotecnológica ainda é bastante limitada que se deve à eventual citotoxicidade e baixa estabilidade coloidal da maioria destas partículas. Entre estas partículas, as estruturas baseadas em carbono chamam a atenção de diversos grupos de pesquisas devido à biocompatibilidade, alta área de superfície e estabilidade. Deste modo, se faz necessário a preparação de novas nanopartículas que apresentam baixa citotoxicidades, condições essenciais para direcionar o desenvolvimento de novos sistemas para administração de medicamentos. Entre os materiais à base de carbono, as partículas de nanodiamante (NDs) começaram a emergir como novas candidatas para aplicações promissoras no campo da nano-biotecnologia, como sonda de imagens e transportadoras de medicamentos. Os NDs não apresentam citoxicidades quando comparados a outros tipos de nanopartículas, como por exemplo, partículas de ouro. Entre as estratégias não penetrantes do tratamento antineoplásico, as terapias fotodinâmica (PDT) e fototérmica (PTT) são consideradas as mais eficazes para o futuro. Até agora, o desenvolvimento de PDT e PTT é limitado pela capacidade da penetração da luz no tecido. Esta pesquisa está focada na elaboração e investigação de novos nanomateriais híbridos que podem ser usados na terapia invasiva estabelecida mais recentemente, com base no tratamento ultrassonográfico (Sonodinâmica) e de raios-X moles (Fotodinâmica) do câncer. Neste projeto, uma abordagem de preparação de nanocompósitos de NDs funcionalizados foi realizada. A ideia do projeto é baseada na funcionalização de NDs com grupos fotorremovíveis que, na presença de radiação UV, pode liberar fármacos de modo seletivo para dentro da célula. A imobilização covalente de foto-sensibilizadores e componentes bioativos na superfície de nanocompósitos via linker foto-clivável é planejada para garantir sua liberação controlada. Outro suporte promissor para a imobilização por arrasto são as nanopartículas de carboneto de silício (nSiC). Tem cristalinidade semelhante aos NDs e também possui baixa citotoxicidade.

Existem vários aspectos importantes na aplicação de nanopartículas em biotecnologia:

1) baixa citotoxicidade, 2) tamanho nanométrico das partículas que permite o livre movimento na corrente sanguínea, 3) liberação do fármaco alvo.

O projeto cobre todos esses aspectos e particularmente:

1) Nova metodologia para preparação de nSiC a baixas temperaturas foi elaborada. As partículas nSiC foram caracterizadas e suas propriedades químicas são investigadas;
2) Diferentes tipos de DEs foram estudados como suporte potencial para a imobilização de fármacos. Várias abordagens foram usadas para obter a suspensão estável em água dos NDs. Estabilidade coloidal excepcionalmente alta em solução fisiológica modelo demonstrou suspensão mista de

SiO2 / NDs que pode ser usada para desenvolvimento adicional dos transportadores de fármaco.
3) Diferentes procedimentos de ativação superficial de NDs nativos foram investigados antes da imobilização de grupos funcionais,
4) Nova estratégia para imobilização covalente de grupos funcionais com fragmentos fotoactivos foi desenvolvida. A estratégia permite usar a abordagem simples de química de cliques disponível nos hospitais
5) A libertação de fármaco desencadeada é conseguida sob tratamento com UV de NDs tendo fármacos modelo imobilizados.

3. Abstract

The project is about preparation of new nanoparticles having no or less cytotoxicity. It is one of the major directions in development of novel systems for drug-delivery.

Nanoparticles have been used in vast applications ranging from energy storage to biotechnology. However, its biotechnological application is still quite limited due to the eventual cytotoxicity and low colloidal stability of most of these particles. Among these particles, carbon-based structures attract the attention of various research groups due to biocompatibility, high surface area and stability. Thus, it is necessary to prepare new nanoparticles that have low cytotoxicities, essential conditions to direct the development of new systems for administering drugs. Among carbon-based materials, nanodiamond particles (NDs) have begun to emerge as new candidates for promising applications in the field of nano-biotechnology, such as imaging and drug carriers. Among the non-penetrating strategies of antineoplastic treatment, photodynamic (PDT) and photothermal (PTT) therapies are considered the most effective for the future. So far, the development of PDT and PTT is limited by the ability of light penetration into tissue. This research is focused on the elaboration and investigation of new hybrid nanomaterials that can be used in these most recently established invasive therapy treatment of cancer. The idea of the project is based on the functionalization of NDs with photolabile groups that can release drugs into the cell under light-radiation treatment. The covalent immobilization of photosensitizers and bioactive components on the surface of nanocomposites via photo-cleavable linker is planned to guarantee their controlled release.

Other promising support for the drag immobilization is silicon carbide nanoparticles (nSiC). It has similar crystallinity as NDs and it is also possess low cytotoxicity.

There are several important aspects in application of nanoparticles in biotechnology:
1) low cytotoxicity, 2) nanometric size of the particles that allows free movement in the blood stream, 3) target drug release.

The project covers all these aspects and particularly:
1) New methodology for low-temperature nSiC preparation has been elaborated. The nSiC particles have been characterized and their chemical properties is investigated;
2) Different types on NDs have been studied as potential support for drug immobilization. Various approaches were used for obtaining of water-stable suspension of NDs. Unusually high colloidal stability in model physiological solution demonstrated SiO_2/NDs mixed suspension that can can be used for further development of the drug carriers.
3) Different surface activation procedures of native NDs were investigated prior immobilization of functional groups,
4) New strategy for covalent immobilization of functional groups having photo-active fragments has been developed. The strategy allows use simple click-chemistry approach available in the hospitals
5) Triggered drug release is achieved under UV-treatment of NDs having immobilized model drugs.

4. The project objectives

4.1. **The project targets.**

Hybrid organo-mineral nanoparticles suitable for bio-analytical application and particularly for drug monitoring delivery with low cytotoxicity and intrinsic fluorescence that has been provided by using silicon carbide and nanodiamonds as a support, and with triggered drug release that has been ensured by photolabile immobilization of the target drugs.

4.2. **The project general objectives**

1) Develop procedures for electrochemical and chemical preparation of silicon carbide (n**SiC**) and silicon (**nSi**) nanoparticles at PUC-Rio;
2) Develop procedures for activation (**ND**s and n**SiC)** and stabilisation (**nSi**) of the particle surface;
3) Synthesis and characterization of photoactivable linkers;
4) Functionalization the particles modified with photoactive linkers

    a. Covalent immobilisation
    b. Non-covalent immobilisation

5) Bio-functionalisation of the particles with target molecules
    a. With models compounds (horse radish peroxidase, lectin and mannose)
    b. With project-important bio-molecules (insulin, cephalosporin and amphotericin B (tuberculosis), Doxorubicin and Paclitaxel (as anticancer drug)
6) Investigation of the particles behaviour and drag release to the model environmental by UPLC-MS/MS, Raman confocal microscope and other technics.

5. The project plan.

The project was organized in six work packages, Table 5-1.

Table 5-1 The project Work Packages (WP)

Work package number	1	Start date:	Month 1
Work package title	SiC nanoparticles and nanowires		

Specific objectives:
    a) Development of the procedures for high-temperature synthesis of SiC from SiO2 and carbon sources
    b) Development of the procedures for low-temperature matrix-based synthesis of silicon carbide (nSiC) nanoparticles from polycarbosilane
    c) Optimization of SiC powder and SiC nanowires thermochemical treatments for removal impurities (SiO_2, C)

Researchers
Prof. Volodymyr Zaitsev – supervisor
Dr. Mykhailo Nazarkovskyi (PDJ)
Prof. Sergey Alekseev (Collaborator, Ukraine)
Miss Olena Artiushenko (PhD student)
Mr. Dmytro Korytko (PhD student)
Dr. Igor Bezverkhyy (Collaborator, France)
Dr. Kostiantyn Turcheniuk (Collaborator, France)

Work package number	2	Start date:	Month 1
Work package title	SiC particles activation and characterization		

Specific objectives:
   a) Study influence of the preparation conditions on textural properties of low-temperature SiC
   b) Study the influence of the polycarbosilane (PCS):SiO$_2$ ratio and the PCS type on the SiC parameters
   c) Study the influence of the pyrolysis temperature on the textural parameters, structure and properties of SiC
   d) Understanding the chemical processes occurs at low-temperature SiC preparation
   e) Study structural characteristics and porous properties of SiC nanowires

Researchers
Prof. Volodymyr Zaitsev – supervisor
Dr. Mykhailo Nazarkovskyi (PDJ)
Dr. Eloah Pereira Ávila (PDJ)
Miss Albina Mikhraliieva (PhD student)
Dr. Kostiantyn Turcheniuk (Collaborator, France, USA)

Work package number	3	Start date:	Month 1
Work package title	**Synthesis of photoactive binding molecules**		

Specific objectives:
   a) Preparation of photoremovable linkers (PRL)
   b) Development of click-chemistry procedures for immobilization of PRL
   c) Preparation of model compounds in solution (1,2,4-triazole derivative) using Click-chemistry approach

Researchers
Prof. Sabine Szunerits (PVE) – supervisor
Dr. Eloah Pereira Ávila (PDJ)
Dr. Mykhailo Nazarkovskyi CAPES postdoc
Dr. Kostiantyn Turcheniuk (Collaborator, France)

Work package number	4	Start date:	Month 12
Work package title	NDs particles activation and characterization		

Specific objectives:
   a) Study surface chemistry of NDs depending from provider
   b) Development of the procedures for characterization of ND surface
   c) Development of the procedures for activation (carboxylation/alkoxylation) of NDs

Researchers
Prof. Volodymyr Zaitsev – supervisor
Dr. Eloah Pereira Ávila (PDJ)
Miss Albina Mikhraliieva (PhD student)
Dr. Mykhailo Nazarkovskyi CAPES postdoc

Work package number	**5**	Start date:	Month 12
Work package title	Immobilization of functional groups on ND surface. Functionalization the particles modified with photoactive linkers		

Specific objectives:
  a) Functionalization of NDs with -OH groups on the surface
  b) Functionalization of NDs with -COOH groups on the surface

Description of work
Development of the procedure for linking of photolabile molecules onto NDs
Development of the procedure for subsequent linking of biomolecules on ND surface

Deliverables
D5.1. Protocol for linking of photolabile linkers to NDs
D5.2. Protocol for linking acid and amine-functionalized molecules to photolabile linker

Researchers
Prof. Sabine Szunerits (PVE) – supervisor
Dr. Eloah Pereira Ávila (PDJ)
Dr. Mykhailo Nazarkovskyi CAPES postdoc
Dr. Kostiantyn Turcheniuk (Collaborator, France)

Work package number	6	Start date:	Month 18
Work package title	Biomedical application of NDs		

Specific objectives:
  a) Investigation of suspension stability of NDs and hybrid materials (with TiO_2/SiO_2) in water and in physiological solutions
  b) Cell-toxicity of NDs

Researchers
Prof. Sabine Szunerits (PVE) – supervisor
Prof. Luiz Alves (FioCruz, Brazil)
Dr. Eloah Pereira Ávila (PDJ)
Dr. Mykhailo Nazarkovskyi (CAPES)
Dr. Kostiantyn Turcheniuk (Collaborator, France, USA)
Dr. Rabah Boukherroub (Collaborator, France)
Dr. Aloysius Siriwardena (Collaborator, France)
Mr. Volodymyr Turcheniuk (PhD student)

6. State of the Art of the project

Nanostructured materials have found widespread applications in diverse fields ranging from catalysis to energy storage to biotechnology. The versatile nature of these materials is linked to the possibility to tailor in a controlled way the physical and chemical properties of the materials. Inorganic materials have shown to exhibit superior structural and chemical stability compared to organic materials. Thus, inorganic nanostructured materials have gained considerable importance in several biotechnological applications related to composite materials for implants, sensing and drug delivery. Drug delivery systems serve a variety of roles, such as improving poor solubility, enhancing *in vivo* stability, and optimizing the bio-distribution and pharmacokinetics of drugs. They can also be used to target specific tissues and cell types through appropriate functionalization.

There are two main categories of drug delivery systems, which have been developed over the years. The first group consists of capsule-like vehicles, including micelles and liposomes. These systems have the ability to encapsulate a relatively large amount of drug within their self-assembled structures [1]. The second family of carriers are those to which to drugs are appended on the outside. Among this category, nanoparticles (NPs) and nanostructured materials (NSm) have been investigated as carriers. At the forefront have been polymer-based NSm that offer opportunities for prolonged delivery of a drug while maintaining blood concentrations within therapeutic limits. Several types of polymeric and polymer/metal are currently under investigation as sustained release vehicles. Silica and gold NPs are also proposed as versatile drug carriers [2]. A wide variety of functional bio-nanoconjugates have been obtained including NPs modified with peptides, proteins, antibodies, sugars and nucleic acid.

However, due to possible cytotoxicity of gold nanoparticles and pyrogenic effect of silica, the importance in biological applications of carbon-based materials such as fullerenes, carbon nanotubes and carbon NPs has been recently recognized. Nanodiamond particles (often referred to simply as nanodiamonds, NDs) have emerged as especially promising candidates in the field of nano-biotechnology [3]. The therapeutic potential of NDs as drug carriers was first shown by the Ho group [3] that succeeded in fabricating NDs, surface adsorbed with doxorubicin [4]. Moreover, it was demonstrated that NDs themselves did not show the toxicity often observed with other NPs, and notably that of Au NPs further reinforcing their suitability as nanoscale drug delivery and imaging platforms. In our primary research we demonstrated that silicon carbide nanoparticles (nSiC) has the same potential as imaging platform for monitoring as ND [5]. Particularly, it was demonstrated that incubating of surface-modified nSiC in fibroblast culture does not destroyed the living cell and fluorescent nanoparticles are present in both cytoplasm and nuclei of the cells.

Diabetes and cancer are but two examples where treatment with drug functionalized NDs may have a real therapeutic potential. Insulin, surface adsorbed onto NDs, was shown to desorb over time. It follows that this latter system could potentially serve as a controlled release therapy for diabetics, thus negating the need for insulin injections [6]. Covalent attachment of the potent anticancer drug paclitaxel, which required a complex surface modification process of oxidation, alkylation and amination, led to the formation of a cytotoxic nanocomposite that delivered multiple active drug molecules to lung carcinoma cells [7]. Of the two methods of drug attachment – strong but reversible adsorption or covalent linkage. The type of bond formed between the drug and the ND or nSiC surface has to be carefully chosen so that dissociation, and drug-release, is triggered by disease-related conditions, such as the unusually low pH or the presence of specific up-regulated enzymes often associated with cancerous cells. Triggered drug-release would guarantee that any functionalised ND and nSiC would be at the site of action of any given drug prior to its being liberated/activated. In this sense the NDs would be performing the well-established role of prodrugs, "smuggling" a "silent" but active compound to their targets whereupon they would, through a controlled bond cleavage, be liberated and rendered active.

NDs and nSiC possess several other attractive properties for their biomedical applications:

i) They are much more stable than metal and silica NPs for aggregation and bio-degradation;

ii) Their functionalization and biomolecule immobilization is readily accomplished;

iii) ND carbon cores and SiC-core are capable of fluorescing due to point defects [8] and so can be used for monitoring of drug delivery, labelling of therapeutic agents and imaging of targets;

iv) Triggered drug release from the particles surface can be achieved by immobilisation of photoactive linkage groups (such as *o*-nitrophenol derivatives) that will bind the target drug with the particle surface. Because of high photoactivity of the particles (ND and nSiC) such linkers can be activated in immobilised state that will lead to the drug release [9].

7. The project results

The project has been organized according to the project objectives and structured in 6 work packages (**WP**). These WPs are essentially aimed at organizing activities, so as to schedule the deadlines and milestones, and to define the responsibilities. The activities within the work packages has been carried out in close synergy with each other. It is anticipated that there has been a strong feedback and interconnections between the different WPs.

7.1. WP1. Develop of the procedures for chemical preparation of silicon carbide (nSiC) nanoparticles
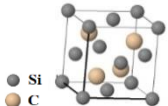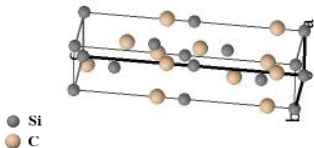
7.1.1. Abstract

Commercial bulk powder of SiC and SHS-synthesized SiC nanowires were studied. Basic properties, such as crystalline structure, phase composition, morphology and photocatalytic activity with the quantitative analysis of the reaction products, were determined. Obtained silicon carbides are crystalline materials of hexagonal (commercial SiC) and cubic (synthesized SiC nanowires) structures. No gold phase has been detected as a separate crystalline component in both Au-modified samples. The gold-containing SiC nanowires demonstrated an essential enhancement of photocatalytic activity keeping Au nanoparticles on the surface after the reaction.

7.1.2. Introduction

Silicon carbide SiC is an outstanding non-oxide ceramic material, having diverse industrial and scientific applications due to high hardness and strength, thermal stability, high melting point, and oxidation resistance. These properties are well-known and extensively explored for various forms of SiC – films, mesoporous structures, powders, nanowires. It is a component of catalytic systems, epoxy-composites, oxidation-protective coatings, electrical and semiconductor devices – in a word, the multiplicity of applied characteristics is proven and prolifically reflected in the decade-by-decade published experimental [10,11,20,12–19] and theoretical [21–25] studies.

Approximately 250 crystalline structures (polytypes) of SiC have been discovered and classified within cubic, hexagonal and rhombohedral configurations. Some authors indicate that SiC polytypes feature in the seed orientation in terms of crystallography, whereas this phenomenon was supposed to be associated with different surface energies of Si and C faces [26]. The most common polytypes are listed as 3C (E_g = 2.3 eV), 4H (E_g = 3.2 eV) and 6H (E_g = 3.0 eV) forms which are under scientific focus of various research groups (Table 7-1) [27–32]

Table 7-1. Crystal structure data for 3C, 4H and 6H polytypes of SiC

Polytype	Space group	Cell parameters	Visualisation
3C (PDF 29-1129)	F-43m, cubic	a = b = c = 4.358 Å α = β = γ = 90°	
4H (PDF 29-1127)	P6$_3$mc, hexagonal	a = b = 3.082 Å, c = 15.118 Å α = β = 90°, γ = 120°	

6H (PDF 29-1128) P6$_3$mc, hexagonal	a = b = 3.073 Å, c = 10.053 Å	
	α = β = 90°, γ = 120°	
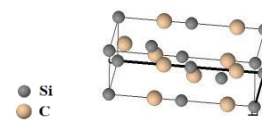
To such a promising matter, like SiC nanowires, was dedicated a big deal of publications elucidating a great variety of synthesis techniques, i.e. arc discharge, carbon nanotube confined reaction, high-frequency induction heating, laser ablation, a sol-gel combined with carbothermal processing and CVD – in all summarized cases, 3C-SiC as the crystalline phase was reported by Zhou *et al.* in the review [33]. Likewise, by Gundiah *et al.* [34], who synthesized SiC nanowires by means of sol-gel/carbothermal methods using TEOS, ethylene glycol and citric acid (method 1) and heating silica with activated carbon (method 2), cubic silicon carbide is communicated. The incipiency of crystalline 3C-SiC is due to its highest stability at low-growing temperatures in comparison to the rest of polytypes [35]. As theoretical simulations on zigzag SiC showed, at smaller diameter, that respective nanotubes adsorb more CO_2 molecules, i.e. decrease in surface curvature brings lowered energy of CO_2 adsorption [36].

7.1.3.   High-temperature SiC synthesis

High-temperature synthesis of nSiC particles from silica and carbon-containing samples (citric acid, starch) at different activation (150-250 C) and crystallization (1200-1500 C) temperatures was stablished in PUC-Rio with collaboration with department of Physics.

A large variety of papers was published on SiC synthesis since its production was initiated in 1892 – depending on a form, different ways to manufacture SiC are considered. The most commonly used methods for SiC synthesis are physical vapour deposition (PVT), chemical vapour deposition (CVD), sol-gel, liquid phase sintering (LPS) or mechanical alloying (MA).

As catalysis is aimed in the present study, the sol-gel method is preferable. The advantages of the sol-gel approach are the formation of high-purity products with uniform and disperse microstructures. Furthermore, the sol-gel process is an effective way for synthesis of nanopowders and it can be adapted to production of films, fibers, and bulk pieces of SiC. To obtain SiC, generally, a mixture of silica sols (pre-hydrolyzed silicon alkoxides) and carbon source (starch, activated carbon, organic acids, saccharose) is used, which is exposed to drying (air) and calcination (argon).

Procedure for SiC nanoparticles synthesis.

A dry sample of nanosilica, SiO_2 (1 g, Sigma Aldrich) was introduced to 10 mL of citric acid water solution, $H_8C_6O_7$ (3.55 g, Proquimios, analytical grade) at molar C/Si ratio 4 : 1. The obtained suspension was sonicated for 3 min using an ultrasonic processor UP200S at a 0.5 s pulse pause.

The suspension was halved. Both portions were exposed to drying at 250 °C (6 h). One part (SiC_1) was dried on air, whereas another one (SiC_2) underwent heating at the same temperature in a vacuum chamber.

Dried samples are differently colorized (Figure 7-1), which means that in SiC_1 citric acid totally decomposed, and nano-silica particles in SiC_2 are uniformly covered by dry citric acid.

Figure 7-1 Intermediate dried samples of SiO$_2$-citric acid xerogels: SiC_1 (right) and SiC_2 (left).

The samples were finely ground and heated at 1400 °C under inert atmosphere (Ar) during 3 h. Argon was purged for 15 min prior to the introduction of the powdered sample in a tubular chamber.

The thermally processed samples were dipped into concentrated HF (1 h), HF : C2H5OH (10 : 90 v/v) (20 h) to eliminate traces of SiO$_2$ and free carbon.

To analyze textural properties of SiC film and SiC nanowires (S_{BET}, porosity), low-temperature N$_2$ adsorption–desorption (Micrometrics ASAP 2405N) was used. The total pore volume, V_p, was determined at the maximal adsorption point, i.e. at p/p0 = 0.98 - 0.99. Specific surface area, S_{BET}, was calculated from the standard BET method described in and parameters of textural porosity, e.g. incremental pore size distribution (IPSD), were estimated by application of the self-consisted regularization (SCR) under non-negative conditions of the pore size distribution function, i.e. $f(R_p) > 0$ at any pore radius R_p and at the set regularization parameter a = 0,01.

X-Rays spectra were recorded using a D8 Discover diffractometer (Bruker) at λ = 0.154 nm (Cu$_{K\alpha}$). The SEM images were recorded by means of a JEOL JSM-6700F scanning electron microscope.

Discussions

The mechanism of carbothermal treatment of SiO$_2$-C or SiO$_2$-citric acid samples may be described as follows[34]:

SiO$_2$ (s) + C (s) → SiO (vap) + CO (g)

SiO (vap) + 2C (s) → SiC (s) + CO (g)
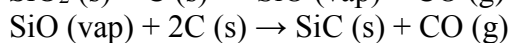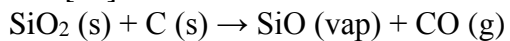
The samples did not demonstrate any difference in morphology and phase composition (Figure 7-2 and Figure 7-3). The X-rays patterns indicate that negligible amount of crystalline SiC is formed in parallel to huge amorphous phase.
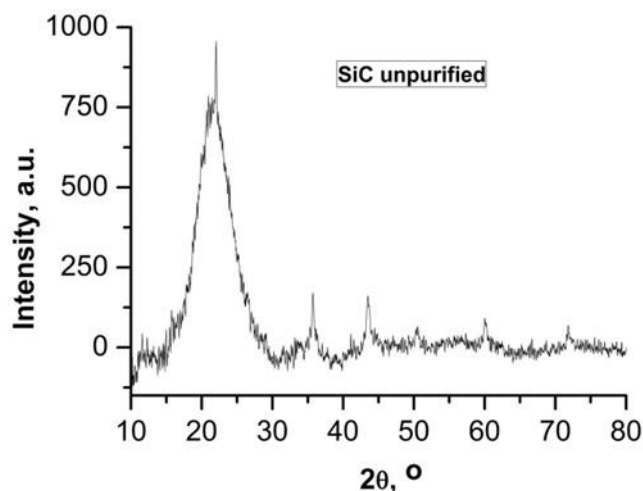
Figure 7-2 Phase composition of SiC_1 (analogous X-rays patterns are observed for SiC_2)

Figure 7-3 SiC_1 after high-temperature processing (analogous view of SiC_2)

Further processing with the help of HF has shown that amorphous phase is related to carbon left in a residue.

7.1.4. Low-temperature matrix-based synthesis

The procedure for preparation of porous SiC with uniform sized (12 nm and 22 nm) and with spherical porosity was developed in collaboration. SiC was synthesized from nanocomposites of polycarbosilane (PCS) preceramic polymer and xerogels of Ludox® SiO_2 nanoparticles as templates. The influence of PCS type, PCS : SiO_2 ratio, pyrolysis temperature, and addition of Ni complex to the preceramic composite was studied with respect to the SiC porous morphology, crystalline structure and chemical properties. We found that the pore walls of Ni-free SiC are composed of relatively large (20 nm) crystallites embedded inside a poorly crystalline $SiC/SiC1+x$ phase. Increasing the pyrolysis temperature resulted in an increase of the large crystallites fraction, as well as of the stability with regard to air oxidation.

Introduction

Porous SiC (por-SiC) can be synthesized by not only by a) direct interaction between silicon and carbon-containing compounds as it is described here above, but by b) thermal decomposition of polycarbosilane (PCS) polymer inside the pores of a solid template (commonly SiO_2), followed by template removal in either HF or alkaline solutions.

The later one allows obtaining mesoporous SiC with inverse replica structure. Using silica-based mesoporous molecular sieves (such as SBA-15 and KIT-6) as templates resulted in SiC samples with large (up to $1000 m^2 g^{-1}$) surface area and well-ordered mesopores with a diameter of 3– 4 nm. However, low crystallinity and relatively small pore size (below 3 nm) arising from the template structural peculiarities (thin SiO_2 pore walls) may result in diffusion limitations once the SiC hosts NPs with a 3– 10 nm size range.

In this research we have made an attempt to synthesize por-SiC with large surface area and uniformly-sized mesopores possessing highly crystalline pore walls. Xerogels of SiO_2 NPs prepared from commercially available Ludox® sols were used as templates for PCS nanocasting. In particular, the influence of the PCS molecular weight, PCS:SiO_2 ratio, template nanoparticle size and pyrolysis temperature were investigated for the porous SiC morphological parameters, crystallinity and oxidation stability. Furthermore, we also explored the addition of Ni(acac)2 complex to the initial PCS:SiO_2 nanocomposite to improve the crystallinity of por-SiC without degradation of its porous morphology.

Synthetic procedures

Xerogels were prepared by coagulation of Ludox sols with CTAB to protect the SiO_2 NPs from agglomeration and cross-linking. In a typical procedure, 5 g of CTAB was dissolved in 20 ml of warm (50 °C) H_2O, and rapidly added to 100 ml of the Ludox sol preheated to the same temperature. The mixture was vigorously stirred for 20 min; the resulting precipitate was washed with H_2O, and then dried at 100 °C. The white xerogel powder was ground and the sieved fraction with particles <0.25 mm was calcined in air at 550 °°C for 5 h using a heating ramp of 2 °C min^{-1} up to this temperature.

Nanocomposites PCS:SiO2.

The PCS:SiO_2 mass ratio in nanocomposites was varied in the 0.3–1.0 range. Desired quantities of PCS were dissolved in tetrahydrofurane (3 ml per 1 g of SiO2) and added to the xerogel. To prepare Ni-containing PCS:SiO_2 samples, the toluene solution of Ni(acac)$_2$ was added to PCS solutions so as to obtain a Ni : PCS mass ratio in the range of 0–5 wt %. The mixture of the xerogel and PCS solution was sonicated for 30 min under N_2 and then slowly (approx. 2 h) evaporated using mild heating and intense mixing under N_2. The composites were ground and initially dried at 110 °C in N2. Porous SiC samples. Pyrolysis of the composites was performed in Ar according to a temperature program described by Shi et al. as follows: 2 °C min_1 to 300 °C, then 5 h at 300 °C, followed by a ramp of 0.5 °C min^{-1} to 700 °C, and 2 °C min^{-1} to the maximum temperature (1200, 1300 or 1400 °C) at which the samples were kept for 10 h. Finally, the ceramics were cooled down in Ar, and then ground in an agate mortar. The SiO2 was leached by HF (40%) solution, and then by HF : EtOH (1 : 1, v/v), washed with EtOH : H_2O (1 : 9), and dried in air at 110 °C, providing dark-grey to black powders of por-SiC. Dried samples were checked for the absence of SiO2 template residues by FTIR spectroscopy.

7.1.5. SiC nanowires

A designed technique of Self-Propagating High-Temperature Synthesis (SHS) was used to obtain SiC NW. The concept of SHS lies in the exothermic, self-sustainable process initiated by the resistive heating of homogenous stoichiometric mixture of powdered silicon Si and polytetrafluoroethylene – $(CF_2)_n$– at and terminated within few seconds (Figure 7-4).

Figure 7-4 The experimental set-up for SHS - left, the light signal emitted during combustion as an observation via polycarbonate window - middle, and raw sponge-like product – right (Copyright © 2013 WILEY-VCH Verlag GmbH & Co. KGaA, Weinheim) [37].

In addition, the sodium azide NaN_3 was introduced (55 wt.%) to enable forming of bundles. The reaction was carried out under the air atmosphere and assumed to occur through two ways:

$2 Si + 2 -(CF_2)- = SiF_4\uparrow + C + SiC$
$2 NaN_3 + 3 Si + 3 -(CF_2)- = 2NaF + C + 2SiC + 3N_2\uparrow + SiF_4\uparrow$
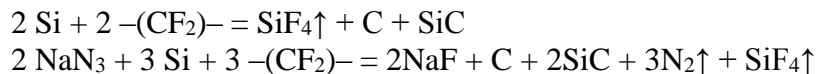
The purification of SiC NW was carried out as follows: raw black nanowires were placed into KOH solution (30 wt.%) and heated at 70-80 °C inside a PTFE jar during 2 h, whereupon cooled down to the room temperature. Obtained alkali suspension was diluted by triple portion (v/v) of distilled water (DW), filtered and washed wth DW under vacuum on a Buechner funnel until pH = 7. Neutralized nanowires were calcined at 680 °C during 2 h. Obtained material had a grey color.

7.2. WP2. SiC particles activation and characterization

Commercial SiC powder (Sigma Aldrich, ≥97.5%, 400 mesh) (SiC SA), SiC nanowires (SiC NW) and low-temperature SiC Nano powder were subjected for purification and characterization.

7.2.1. Methods and instruments

SEM images were recorded using a JEOL JSM-6700F scanning electron microscope and , TEM images of Au@SiC SA and Au@SiC NW samples were made by dint of a JEOL JEM 2010.

To analyze textural properties of SiC NW and SiC SA (S_{BET}, porosity), low-temperature N_2 adsorption–desorption (Micrometrics ASAP 2020) was used. The total pore volume V_p was calculated at the maximal adsorption point, i.e. at p/p_0 = 0.98-0.99, while specific surface area S_{BET} - from the standard BET method. The main parameter of textural porosity, e.g. pore size distribution (PSD), was estimated by application of the self-consisted regularization (SCR) under non-negative conditions of the pore size distribution function, i.e. $f(R_p) > 0$ at any pore radius R_p and at the set regularization parameter α = 0.01. The porosity was assumed as a combination of slits, cylinders and voids among nanowires aggregates formed after heating at 650 °C. The method allows us to estimate the contributions of different pore types based on their size hierarchy: micropores (V_{micro} at $R_p < 1$ nm), mesopores (V_{meso} at 1 nm $< R_p < 25$ nm) and macropores (V_{macro}, $R_p > 25$ nm) by usage of the distribution function $f_v(R_p)$. The method was developed by Nguyen and Do [38,39] and modified by Gun'ko [40,41].

Moreover, CONTIN-based procedure, developed by Provencher in the 1980-s, was involved to calculate the distribution function $f(E)$ of the adsorption energy solving the Fowler–Guggenheim equation [42,43]. The equation rests on description of a localized monolayer adsorption, making allowance for lateral interactions [44,45]:

$$\theta_i(p,E) = \frac{Kp \cdot \exp(\frac{zw\theta}{k_B T})}{1 + Kp \cdot \exp(\frac{zw\theta}{k_B T})}$$

where $K = K_0(T)exp(E/k_B T)$ is Langmuir's constant for adsorption on the energy equivalent sites and the pre-exponential factor $K_0(T)$ is shown as a set of partition functions for isolated gas and surface phases, $z = 4$ is the number of nearest neighbors of adsorbed nitrogen molecule, w is the interaction energy between a pair of nearest neighbors, k_B is the Boltzmann constant. Thus, as a whole, for nitrogen adsorption $zw/k_B = 380$ K.

The distribution function $f(E)$, in turn, is derived from the overall adsorption Θ isotherm on the basis of Fredholm's integral equation using a local isotherm ϑ_1:

$$\Theta(T,p) = \int_0^{E_{max}} \theta_i(T,p,E)f(E)dE$$

where Θ is the experimental amount of N_2 adsorbed. A maximum p/p_0 value corresponds to nearly monolayer coverage $\Theta \sim 0.99$ [46].

The metal colloids were prepared by sputtering deposition on the SiC SA and SiC NW to fabricate Au@SiC SA and Au@SiC NW. The deposition was performed in a sputter coater MED 020 (Bal-Tech), pre-evacuated at 10^{-3} Pa with discharge currents 40 mA for (time), under an argon work pressure of 2 Pa at room temperature. The mass of was measured (1 g) in a cylindrical glass support (3 cm diameter) and placed in the sputter coater horizontally. The SiC samples were located at a distance of 50 mm from the gold target (the matrix of 99.99% purity). The control of deposition rate was performed *in situ* by a quartz crystal film thickness measurement device (QSG 060 - Bal-Tech).

The X-Ray diffraction (XRD) patterns were recorded through the use of a D8 Discover DaVinci diffractometer (Bruker, CuKα, $\lambda = 0.154$ nm). The size of SiC nanocrystallites were determined with the help of Scherrer's equation: $d = K \cdot \lambda/(\beta \cdot cos\theta)$, where $K = 0.94$ (spherical shape) and β is FHWM in radians.

The photocatalytic CO_2 reduction was performed under a 300 W Xe-lamp irradiation in the presence of 20-30 mg of a catalyst (SiC SA, Au@SiC SA, SiC NW or Au@SiC NW) suspended in 2 mL of liquid H_2O saturated with CO_2 during 30 min. The gas phase was sampled manually and analyzed on a gas chromatograph (Agilent, 6890N, TCD) detecting CO or CH_4. To analyze the liquid phase composition after 4 h, the samples were injected in a Thermo Scientific FOCUS Gas Chromatography equipped with a FID detector. The column used was a 30 m Agilent J&W HP-INNOWAX (0.53 mm of internal diameter and 1 μm of film thickness). The conditions used were: oven temperature isothermal at 70 ºC; injection at 200 ºC operated in split mode, with a split ratio of 5; the gas phase was helium with a constant flow of 3 ml min^{-1}; All injections, 2μl, were made by an Thermo Scientific autosampler. External standard calibrations were used.

7.2.2. Influence of the preparation conditions on textural properties of low-temperature porous SiC.

The PSD of SiC film reflects a predominant contribution of mesopores both into total pore volume (V_p) and specific surface area (S_{BET}), indicating an average pore radius at 12.1 nm (Figure 7-5). A negligible share of macropores (10 %) does not change the monomodal distribution, whereas the SCR method is seen to be sensitive to the presence of other pores (maxima at $R_p = 35$ and 90 nm).
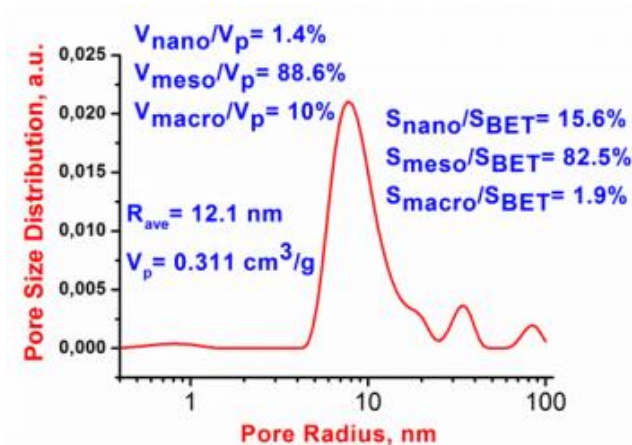
Figure 7-5 The pore size distribution in SiC21-16 film calculated by means of SCR
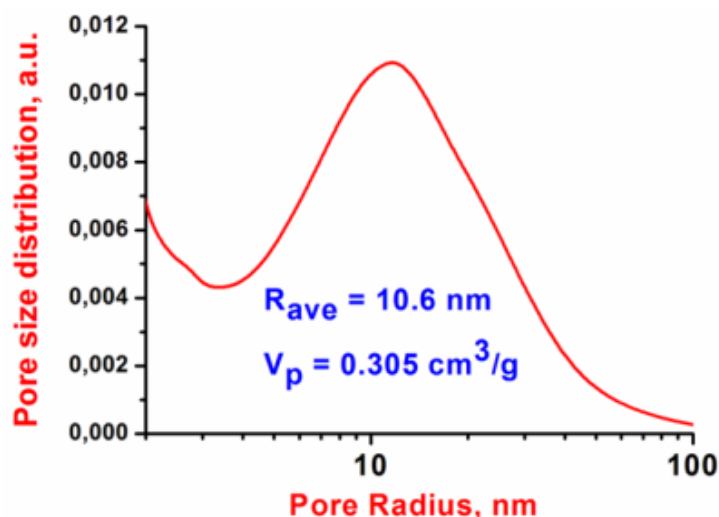

Figure 7-6. The pore size distribution in SiC21-16 film calculated by means of BJH

In parallel, the BJH computation technique is in concordance with the SCR calculations, as shown on the profile of the PSD plot (Figure 7-6). The average pore radius and the total pore volume are similar to the obtained values via SCR. Independently carried out ways of theoretical estimation of porous nature in SiC structure support our assumption about (1) mesoporous morphology, (2) uniform pore distribution, and (3) cylindrical shape of pores.

However, the larger contribution of nanopores to S_{BET} in comparison to macropores leads us to conclusion that their role in surface reactions must be taken in a serious consideration.

According to literature data, thermal decomposition of the PCS at 1200 – 1400 ºC shown in Scheme 1 leads to a SiC reverse replica of the porous SiO_2 template. The results of our FTIR characterizations confirm the SiC formation and completeness of the SiO_2 template removal.

$$[\text{Si}(H)(CH_3)-CH_2]_n \xrightarrow{\ T\ >=1200°C\ } SiC + CH_4 + H_2$$
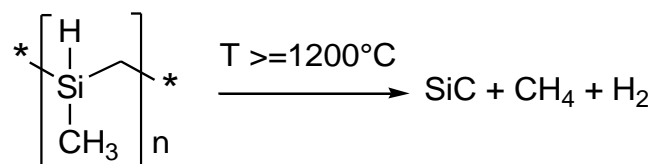
Equation 1. Process of SiC formation from PCS by thermal decomposition

First, nitrogen physisorption isotherms of prepared silica xerogels were collected prior to their mixing with polycarbosilane. They were considered as a type IV of the IUPAC classification with narrow hysteresis loops. These parameters along with the SEM data for the TM40 and TEM data for the HS30 silica template allowed considering the Ludox SiO_2 xerogels as aggregates of loosely and irregularly packed SiO_2 spheres with the relatively narrow size distribution. Note that the porosity of xerogels is caused by interparticular voids; measured pore volumes are of near the same values for both, HS30 and TM40 series, whereas the surface area is much lower and the pore size is higher for the latter one.

7.2.3.   Influence of the PCS:SiO₂ ratio and the PCS type on the por-SiC parameters

To study the influence of the PCS:SiO₂ ratio and the PCS type on the por-SiC parameters, a series of the SiC samples was prepared by 1200 ºC pyrolysis of the composites based on the Ludox HS30 xerogel. Obtained SiC samples demonstrate mesoporosity, high pore volume and surface area making them suitable for biomedical applications (see Table 7-2). Their N_2 isotherms belong to a type IV with the H3 type (for low PCS:SiO₂ ratio) or H1 type (for the PCS:SiO₂= 0.6-1) hysteresis loops (see Figure 7-7).
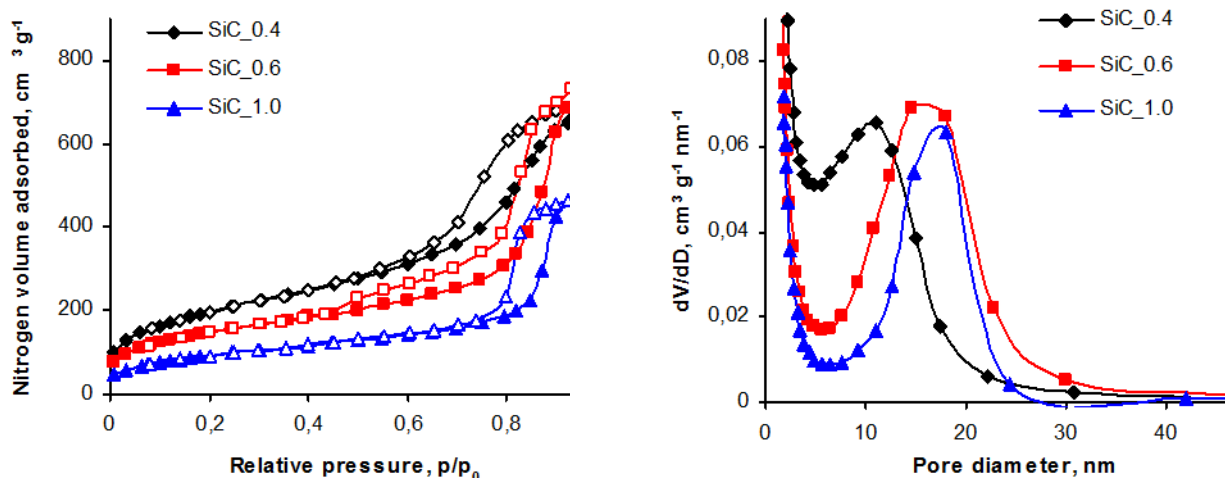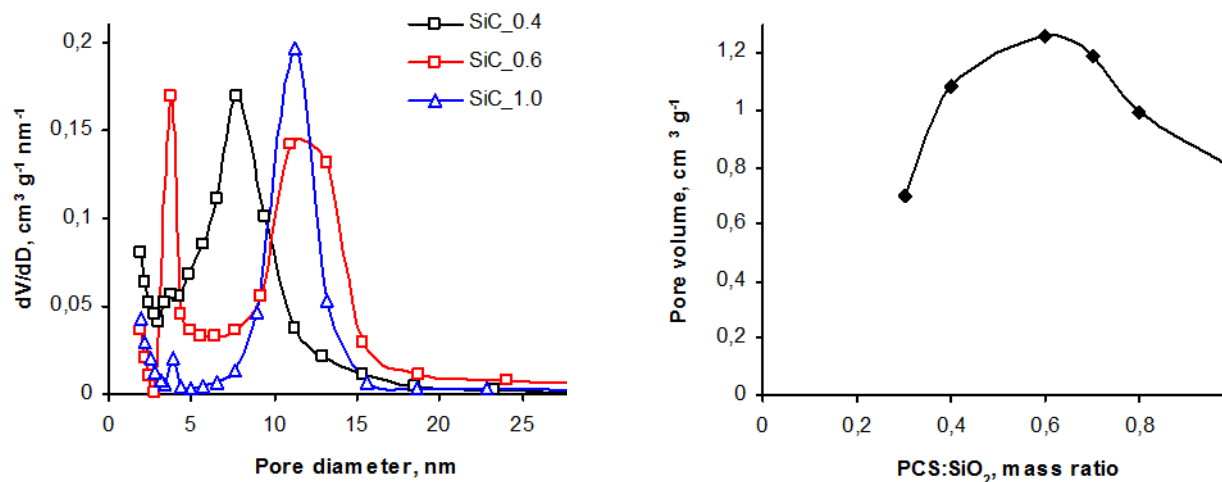
Figure 7-7 (A) Nitrogen physisorption isotherms for por-SiC formed at 1200 ºC from the PCS800 and Ludox HS30 xerogel; BJH pore size distributions calculated from adsorption (B) and desorption (C) branches of isotherms; (D) pore volume versus PCS:SiO₂ ratio. Index in the curve name means the PCS:SiO₂ mass ratio.

The PSDs maximums of the samples with PCS:SiO$_2$= 0.6-1 correlate well with the size of the SiO$_2$ NPs template; whereas the samples with low PCS:SiO$_2$ ratio demonstrate a decrease in the pore size expecting a slit-like geometry according to the shape of their hysteresis loops. A maximum pore volume was obtained using the PCS800:SiO$_2$ ratio of 0.6, corresponding to the PCS filling of approximately 70% of the template pore volume (Figure 7-7 D). Thus, the structure of por-SiC made of the composites with PCS:SiO$_2$= 0.6-1 can be represented as a reverse replica of the template, while the low PCS content led to collapsing of the final structure network, similarly as it was found before for the PCS:SiO$_2$ composites made of Ludox SiO$_2$ NPs organosols.

Table 7-2 Textural characteristics of initial xerogels and porous SiC samples, prepared from Ludox HS30 template at 1200 ºC.

| Sample code*	SBET, m2 g^{-1}	Vs, cm3 g-1	Dads, nm	Ddes, nm	DBET, nm
SiO$_2$-TM40	120	0.65	28	23	21.6
SiC8-HS-1200-0.3	437	0.70	9.2	5.6	6.4
SiC8-HS-1200-0.4	702	1.08	11.0	7.7	6.2
SiC8-HS-1200-0.6	518	1.26	16.5	12.0	9.7
SiC8-HS-1200-0.7	527	1.19	14.6	10.3	9.1
SiC8-HS-1200-0.8	449	0.99	16.3	11.4	8.8
SiC8-HS-1200-1.0	334	0.80	17.0	11.4	9.5
SiC-HS-1200-0.6	436	1.16	12.3	8.8	10.7
SiC-HS-1200-1.0	293	0.62	12.5	9.0	8.5

*The samples marked as "SiC8" were synthesized from PCS800 while PCS2000 was used for "SiC" preparation. Other characters in the code means the template type, PT and PCS : SiO$_2$ mass ratio in initial nanocomposite, correspondingly;

S_{BET} is the surface area; V_s is the pore volume at $p/p_0 = 0.98$; D_{ads} and D_{des} are the maxima of pore size distributions from adsorption and desorption branches of the isotherm, respectively; D_{BET} is the average pore size, calculated from the cylindrical pore model by formula $4V_s/S_{BET}$.

The por-SiC replicas prepared from the polycarbosilanes with different molecular weights demonstrate some difference of the textural parameters. According to the simplified "ink-bottle" pore model, the PSDs maximums from the adsorption and desorption parts of the isotherm correspond to the size of the pore necks and pore voids, respectively. For the low-molecular polycarbosilane (PCS800) the size of the SiO_2 template NPs matches the size of the SiC pore necks, whereas for PCS2000 it coincides with the size of pore voids. The difference between two polycarbosilanes was referred to a partial evaporation of the PCS800 during the pyrolysis procedure. Note that some of the viscous liquid was found in the cold end of the tube after the pyrolysis of the composites based on PCS800 and Ludox xerogel. Collected FTIR spectrum of that substance revealed the structure of used PCS precursor. Due to partial evaporation of the PCS800 the products of its pyrolysis do not cover completely the surface of SiO_2 NPs, and a SiC replica with the pore entrances corresponding to the template NPs and enlarged pore voids are formed. The use of PCS2000 and nanocomposites of PCS800:SiO_2 NPs prepared from the organosols inhibits the PCS evaporation thanks to higher molecular weight of the PCS2000, and due to the PCS800 encapsulation inside relatively large (up to 5 mm) non-porous particles of the composite, respectively. Obtained replicas mimic the pore size and shape of the initial SiO_2 NPs. Another difference between the PCS of different M_w is an absence of the micropores in porous SiC prepared from PCS800 while a small fraction of them was present in the case of the PCS2000 precursor. Micropores are probably formed due to the evolution of the gaseous products (CH_4, H_2) through the continuous solid phase. However, their fraction is negligibly small ($V_{micro} < 0.025$ cm^3 g^{-1} in all studied samples). Thus, the PCS2000 was chosen for all further experiments as one providing better template replicas.

An influence of the template particle size on the por-SiC textural parameters is illustrated by the isotherms and their PSDs of the samples prepared from PCS:SiO_2 nanocomposites pyrolysed at 1300 °C (Figure 7-8). For obtained SiC samples the size of the pore voids (11 and 22 nm) appeared equal to the template particle size, whereas the size of the pore necks ("windows") is significantly smaller (6.5 and 11.5 nm, respectively). Wide hysteresis loops of the H1 type and narrow PSDs allow to describe the SiC texture as uniformly-sized spherical mesopores, which are interconnected to each other through the "windows" of smaller sizes, similarly as it was demonstrated for the organosol-based por-SiC.

Electronic microscopy images confirm the presence of spherical mesopores in the por-SiC samples duplicating the size of initial SiO_2 template, Figure 7-9. However, the pore size and shape uniformity as well as space distribution in the xerogel-based por-SiC are significantly less regular as compared to the organosol-based por-SiC.
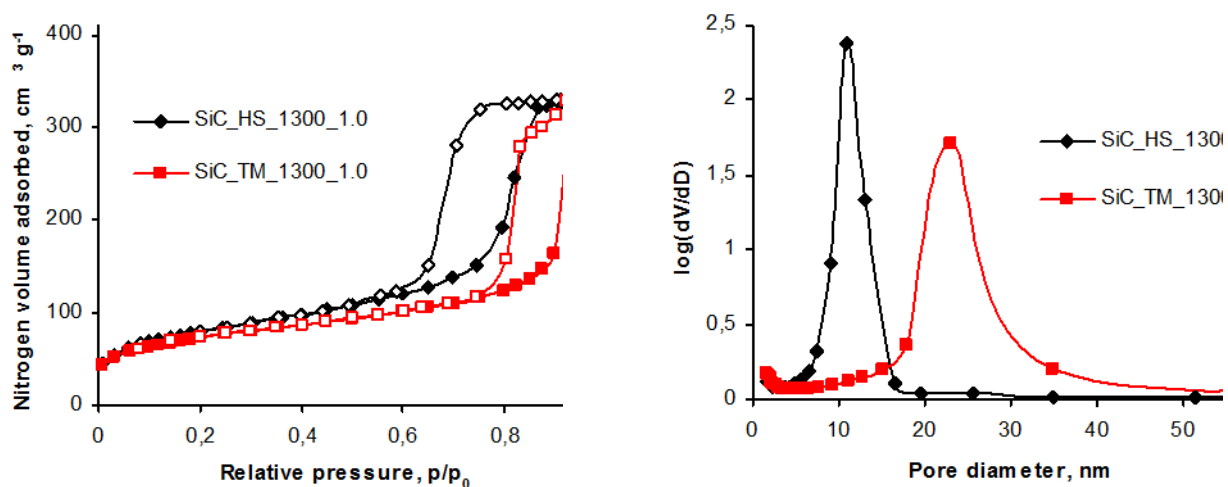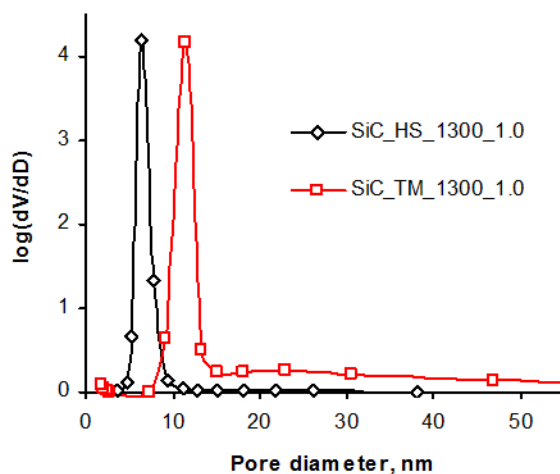
Figure 7-8 Nitrogen physisorption isotherms (A) and BJH pore size distributions calculated from adsorption (B) and desorption (C) branches of isotherms.

The SiC pore walls consisted of small (2-10 nm) crystallites with the interplanar distance matching the plane (111) of 3C-SiC. A negligible admixture of the SiC nanowires (one is clearly seen in Figure 7-8A) is caused by the side gas-phase reaction between the SiO and CO. In general, the xerogel-derived por-SiC samples possess an irregular sponge-like texture with the significant fraction of spherical mesopores originating from the template silica NPs. The values of textural parameters are determined by the diameter of Ludox SiO_2 NPs, the PCS : SiO_2 ratio in initial composites and the PT.
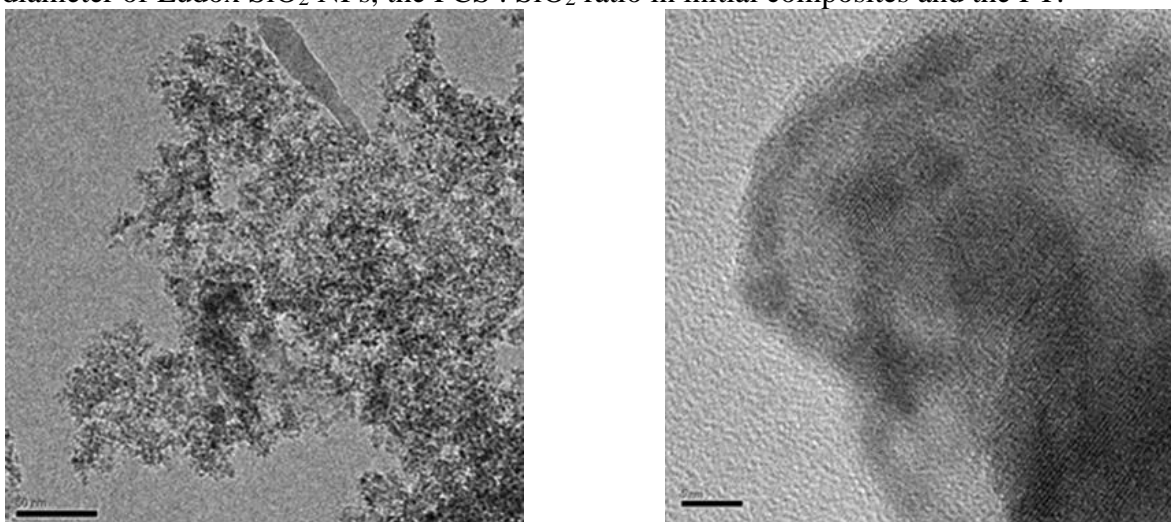

Figure 7-9 Electronic microscopy images of por-SiC TEM images: (A) SiC-HS-1300-1.0; (B) SiC-HS-1400-1.0

7.2.4.   Influence of the pyrolysis temperature on the textural parameters, structure and properties of por-SiC

In general, the PT influences the crystalline ordering of por-SiC, its chemical nature, textural parameters and overall properties. Textural characteristics of por-SiC samples prepared by the pyrolysis at different temperatures are listed in

Table 7-3, their typical powder XRD patterns (for SiC-HS-0.6 series) are shown in Figure 7-10.
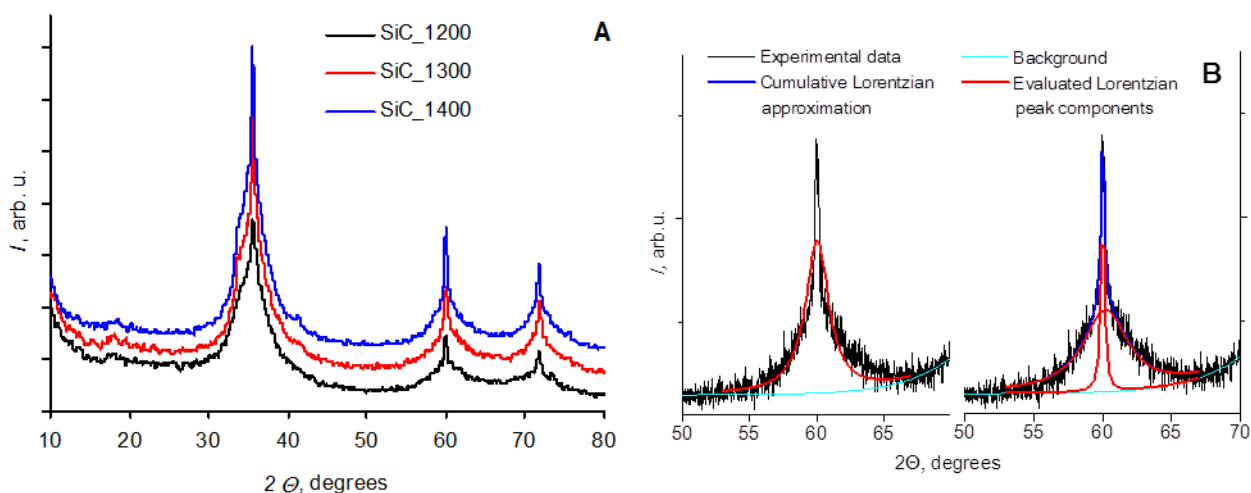
Figure 7-10 A) Powder diffraction patterns of the SiC-HS-0.6 samples formed at different temperatures and (B) Lorentzian deconvolution of the (022) peak of SiC-HS-1400-0.6.

Table 7-3 Textural characteristics of the por-SiC prepared at different temperatures.

Sample code	S_{BET}, m^2 g^{-1}	V_s, cm^3 g^{-1}	D_{ads}, nm	D_{des}, nm	D_{BET}, nm
SiC-HS-1200-0.6	436	1.16	12.3	8.8	10.7
SiC-HS-1300-0.6	434	1.07	12.7	9.4	9.9
SiC-HS-1400-0.6	380	0.94	14.0	11.0	9.9
*SiC-1200-O$_2$_HF	344	0.52	-	3.5	6.1
*SiC-1400-O$_2$_HF	372	0.94	17	13.5	10
SiC-HS-1200-1.0	293	0.62	12.5	9.0	8.5
SiC-HS-1300-1.0	286	0.58	13.0	9.2	8.1
SiC-HS-1400-1.0	304	0.58	14.0	10.2	7.7
SiC-TM-1200-0.7	438	0.97	22	13	8.9
SiC-TM-1300-0.7	426	0.89	22.4	11.6	8.4
SiC-TM-1400-0.7	351	0.72	22.1	13.1	8.2
SiC-TM-1300-1.0	249	0.59	23.0	11.4	9.5

All parameters and sample encoding are the same as used in

Table 7-3.

*The samples are prepared from corresponding SiC-HS-0.6 samples using 2 h air oxidation (500 °C) followed by HF leaching treatment.

Positions of the XRD peaks (CuK$_\alpha$, 2θ = 35.62, 60.06 and 71.85 deg.) correspond to (111), (022) and (113) planes of the 3C-SiC phase, respectively. A shoulder of the (111) peak at 2θ=34 deg indicates a presence of the hexagonal SiC admixtures. The shape of the XRD peaks can be adequately fitted only by two Lorentzian curves of the same positions and different FWHMs, while a single Lorentzian curve does not fit the experimental data as shown in Figure 7-10B. This unusual shape of the peak was explained by a simultaneous presence of the relatively large (approx. 20-25 nm by a simple Scherrer estimation) and small (2 nm) crystallites. A rise in the PT led to an increase of the narrow components intensities indicating a rise in the fraction of large crystallites. The shape of the XRD peaks shown on Figure 7-10, significantly differs from the literature data for the PCS-derived por-SiC samples, where

only relatively wide single Lorentzian peaks, corresponding to few nanometer-sized crystallites were present in XRD patterns. The difference is probably caused by formation of open three-dimensional structure of our PCS:SiO_2 nanocomposites. The growth of relatively large nanocrystallites is not confined in such composites, while it is spatially hindered for the composites of PCS with mesoporous molecular sieves, SiO_2 NPs from the organosols or other templates.

Increase of the PT led to some decrease of the surface area, pore volume, and average pore size estimated by the cylindrical pore model (Table 7-1). Moreover, the SiC samples prepared from 12 nm Ludox HS template demonstrate less uniformity in the PSDs, and their maximums shift to higher values (see Figure 7-11), while for the 22 nm silica template the PSDs and the maximum positions remain practically unchanged.
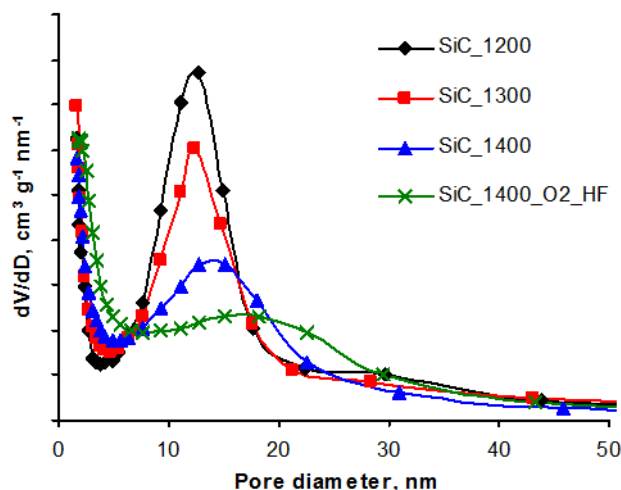

Figure 7-11 BJH pore size distributions calculated from the adsorption part of the isotherm for the series of SiC-HS-0.6 and SiC-1400-O₂_HF samples (
Table 7-3).

These changes are caused by: i) growth of the SiC crystallites size with temperature, and ii) high-temperature side reactions between the SiO_2 template and PCS decomposition products. Both of these factors resulted in an overall shrinkage of the structure (i.e. the V_s and D_{BET} decrease), vanishing of the thinnest SiC pore walls while filling the space between the SiO_2 NPs (i.e. the decrease of S_{BET}) and transformation of the SiC texture from the closely packed spherical pores to irregular 3D network of pores approximating the template NPs size. The temperature impact appeared greater for the SiC-HS samples with thinner pore walls than for the SiC-TM samples having coarse texture.

Influence of the PT on the evolution of the por-SiC crystalline structure was also studied by ^{29}Si MAS-NMR spectroscopy (see Figure 7-12 A). A broad signal at -14,8 ppm with shoulders at -18 and -22 ppm is present in the spectrum of SiC-HS-1300-0.6, and well-defined signals at -15.6, -19.4 and -23.3 ppm could be seen for the SiC-HS-1400-0.6 sample; no other signals such as ones of the SiO_2 and SiOC, recently observed for the PCS-derived por-SiC were found in the spectra. According to literature data [47], the signal at -15 ppm corresponds to cubic "type-A" coordination of Si atoms, while the signals at -20 and -24 ppm belong to "type-C" and "type-B" hexagonal arrangements of Si, appearing in 6H-SiC and 15R-SiC polytypes, respectively. Narrowing and up-field shift of the ^{29}Si NMR signals with the PT indicate the structural ordering of SiC. Taking into account the synthesis temperature (up to 1400 ºC) which favors the formation of 3C-SiC polytype as well as the shape of XRD patterns (Figure 7-13)

and NMR signal positions of hexagonal Si atoms, we assign our data to a presence of disordered hexagonal SiC layers within the 3C-SiC structure rather than to separate crystallites of other polytypes.

Increase of the PT leading to the structural ordering of the SiC results in noticeable improvement of its thermal oxidation stability. The stability towards oxidation was monitored by a significant decrease of the ν(SiO) band intensity in the FTIR spectra of oxidized samples (see Figure 7-12B). Consequent HF leaching led to a removal of oxide (and/or oxocarbide) similarly as it occurred for SiO_2 template after the pyrolysis stage. According to powder XRD data the oxidation and SiO_2 leaching procedure resulted in a noticeable increase of the samples crystallinity, due to partial removal of the "semi-amorphous" SiC. The mesoporous replica structure is disrupted completely after this procedure in the case of SiC-1200 sample, while the replica structure of the SiC-1400 sample withstands the oxidation/leaching steps despite of some pore enlargement and their size distribution widening.
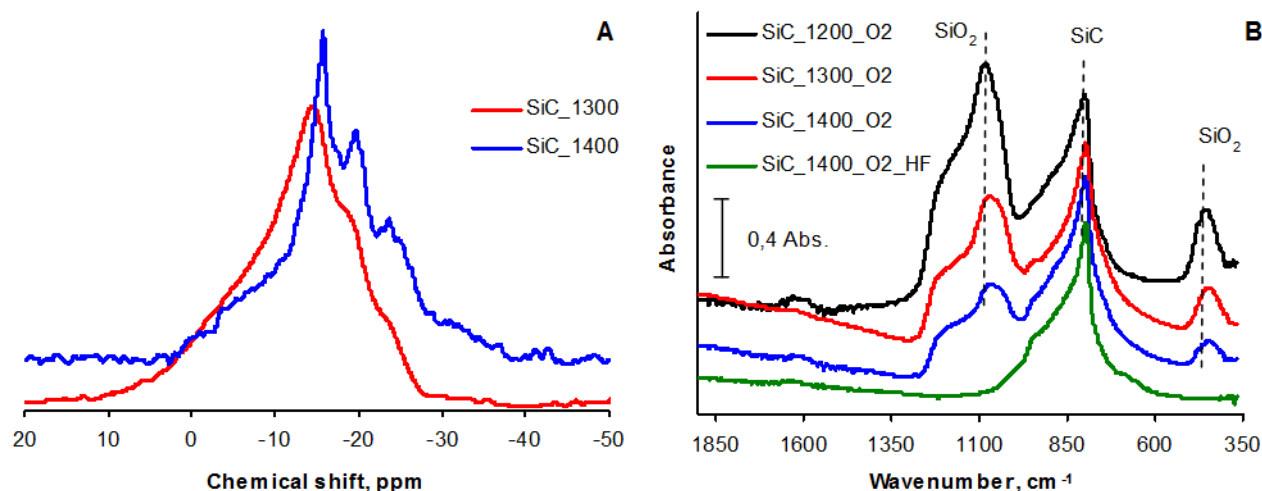

Figure 7-12. A) ^{29}Si MAS NMR spectra for the series of SiC-HS-0.6; B) Normalized absorbance FTIR spectra for the series of SiC-HS-0.6, thermally oxidized in air, and SiC-1400-O$_2$_HF sample (
Table 7-3).

7.2.5.   Understanding chemical processes in low-temperature por-SiC preparation

To understand chemical transformations occurred during pyrolysis and thermal oxidation, the masses of PCS:SiO_2 nanocomposites were monitored at different synthetic stages and were summarized in Table 7-4. XPS characterization of porous silicon carbide and por-SiC after oxidation/leaching steps (SiC-HS-1200-0.6 and SiC-1200-O$_2$_HF, respectively) was also performed (see Figure 7-12). The masses of por-SiC samples were nearly independent on the PT, and were close to the stoichiometric value (SiC/PCS = 69%) according to Equation 1. The sample masses grow slightly during oxidation, and then drop essentially after the SiO_2 leaching. The mass ratio SiC_O$_2$_HF/SiC increases significantly with the PT, confirming growth of the por-SiC oxidation stability, shown above by FTIR (Figure 7-12 B). Comparison of the masses of the por-SiC, SiC_O$_2$ and SiC_O$_2$_HF samples shows that the mass values can be correctly interpreted only if the initial SiC samples contain some excess of matter (carbon or physisorbed H_2O) which is irreversibly desorbed during thermal oxidation.

Table 7-4. Mass ratio (%) between different sample forms.

Sample code	SiC/PCS	SiC_O2/SiC	SiC_O2_HF/SiC

SiC-HS-1200-0.6	69.1	102.5	36.7
SiC-HS-1300-0.6	66.5	103.2	50.2
SiC-HS-1400-0.6	67.1	106.4	66.1

PCS is the initial polycarbosilane; SiC is the silicon carbide after pyrolysis and HF leaching; SiC_O_2 is the silicon carbide sample after oxidation at 500 ^{o}C in air; $SiC\_O_2\_HF$ is the latter sample of oxidized silicon carbide after HF leaching.

The results of XPS characterization confirm the presence of excessive carbon on the surface of as-prepared SiC-HS-1200-0.6 sample (Figure 7-13): except the SiC carbon peak at 282.5 eV, the deconvolution of C 1s line shows intense peaks at 283.8 eV (sub-stoichiometric SiC_{1+x} and free carbon) and 285.8 eV ($Si_xC_{3-x}C–O$ fragments). A minor peak at 287.5 eV can be related to C=O and/or C–F surface fragments. The Si 2p lines are resolved into peaks at 100.5 (SiC) and 102.1 (C_2SiO_2 species of silicon oxocarbide and/or $C_3Si–F$ fragments). Thermal oxidation followed by HF leaching leads to a significant decrease of all "non-SiC" peaks both in C 1s and Si 2p spectra, which indicates the removal of sub-stoichiometric amorphous SiC and "non-SiC" admixtures under oxidation/leaching; the residual peaks (C 1s: 284.1 eV - carbon; 286.4 eV - $C_3C–O$; Si 2p: 101,9 eV - C_2SiO_2 and/or $C_3Si–F$; 102.5 eV - $CSiO_3$ and/or C_2SiF_2) can belong to the SiC surface species. The conclusion on the "SiC purification" via the oxidation/leaching is confirmed by a significant decrease of the O 1s and F 1s XPS lines (presented mainly by Si–O (531.7 eV) and Si–F (686.0 eV) components, and sample color change from black (SiC-1200 and 1300) or dark-grey (SiC-1400) to light-grey after this procedure.
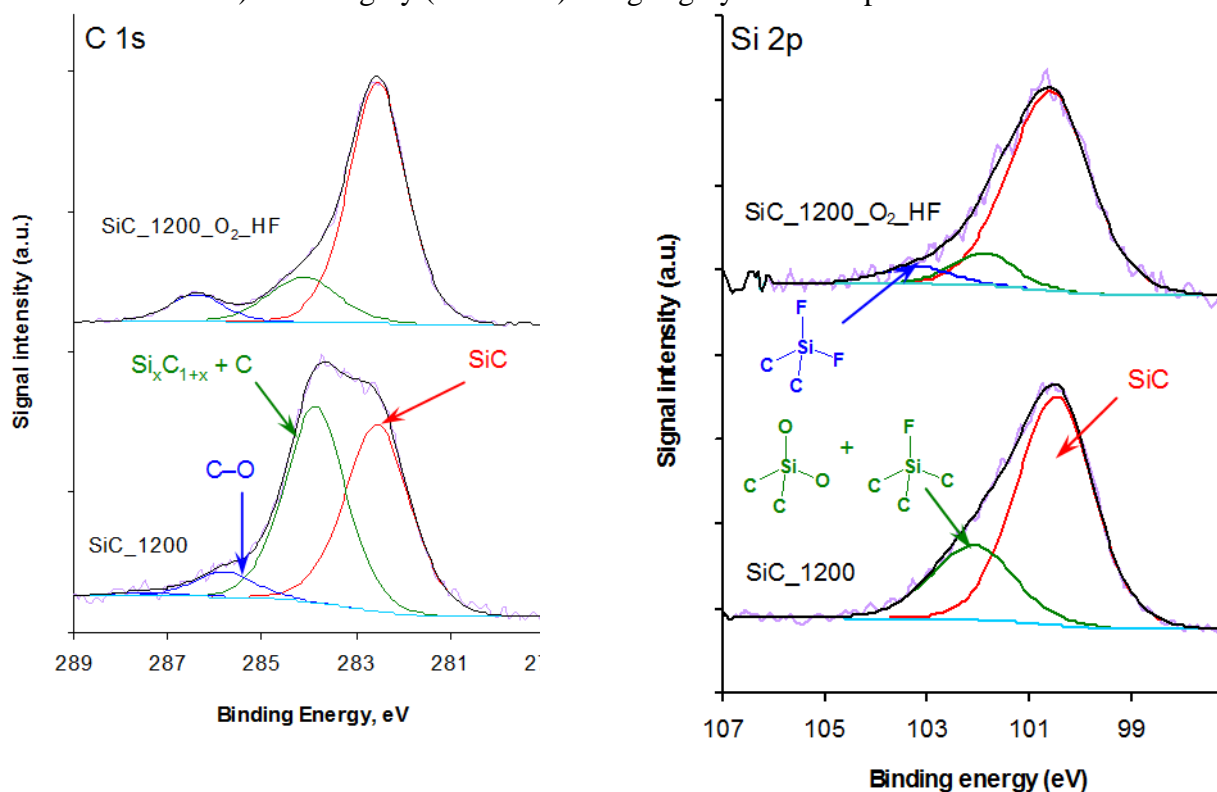

Figure 7-13. The XPS spectra (C 1s and Si 2p) of por-SiC samples SiC-HS-1200-0.6 and SiC-1200-O₂_HF.

7.2.6. Conclusion

The synthesis of porous SiC from the polycarbosilane and SiO$_2$ templates has been extensively studied for the last decade, however in the present work we revealed a number of new features of this process. Application of the Ludox SiO$_2$ NPs xerogels as templates allowed to obtain their sponge-like por-SiC replicas with high pore volume, surface area and spherical pores of uniform size (12 or 22 nm) governed by the initial template particle size. The SiC replicas were formed with the PCS filling of approximately 70% from the template pore volume, whereas at the lower PCS content the replica structure collapsed.

Open texture of the Ludox SiO$_2$ NPs xerogels facilitated the SiC structure ordering. Contrary to PCS-derived por-SiC materials reported in the literature, which show only SiC crystallites of few nanometers size, our por-SiC is consisted of the both, small (2-3 nm) and relatively large (up to 25 nm) crystallites.

XPS characterization of the por-SiC samples, prepared at the pyrolysis temperature of 1200 ºC, demonstrates the presence of carbon/substoichiometric SiC$_{1+x}$, which were removed by consequent thermal oxidation and HF washing steps. The fraction of oxidizable matter in the por-SiC decreased significantly with the PT increase, i.e. with increase of the SiC structural ordering.

The crystallinity of por-SiC was significantly improved by an addition of the Ni acetylacetonate complex into the initial PCS:SiO$_2$ nanocomposites. However, both the PT increase and the Ni catalyst may lead to noticeable degradation of the well-defined porous structure. Optimal synthesis conditions to obtain porous silicon carbide with improved crystallinity and uniform porous structure were determined and could be summarized as follows: mass ratio PCS:SiO$_2$ = 0.6 - 1.0, PT = 1200 or 1300 ºC, Ni:PCS = 1.5 wt.%; or PT = 1400ºC, no Ni. Resulted por-SiC material is a promising candidate for application as a support in the catalysis, where the efficient escape of exothermic heat formation is wanted.

7.2.7. SiC NW

The XRD patterns demonstrate formation of different crystalline phases. If SiC NW features in pure cubic SiC 3C, the commercial sample SiC SA contains two hexagonal phases, 4H and 6H with domination of the 6H configuration (Figure 7-14). Some nSiC samples were used as a support for immobilization of Au nanodots (Au@SiC). Such particles can demonstrate advanced biological as well as environmentally-important catalytic activity.

Demonstrated that the samples do not contain amorphous phase and Au reflexes are not represented on the diffraction diagram, as compared to the standard PDF 04-0784 for Au. The calculated sizes of nanocrystallites do not undergo any change for both neat samples after gold deposition.
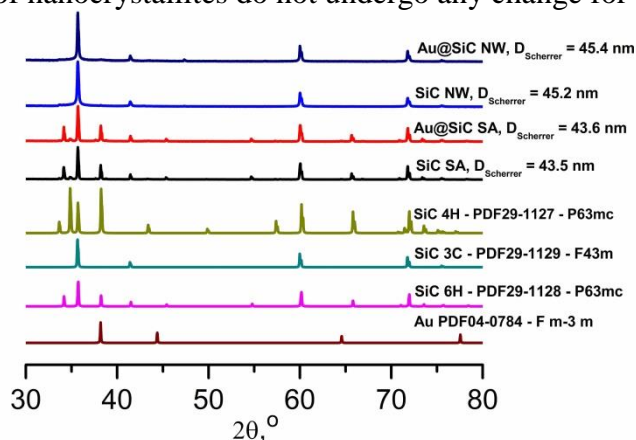
Figure 7-14. XRD patterns of SiC SA, Au@SiC SA, SiC NW, Au@SiC NW and crystalline standard phases: SiC 4H, SiC 3C and SiC 6H.

SiC SA does not exhibit any change either in the surface morphology (Figure 7-15a) or porosity at $S_{BET} = 1$ m^2/g. The model of cylindrical, slit-shaped pores and voids between nanowires for SiC NW was based on the observations of SEM images (Figure 7-15b). The presence of voids among anisotropic bodies of nanowires is significant. Due to anisotropy, a disordered interparticle porosity (gaps) is expected to be responsible for textural properties of SiC NW: the BET curve of the type IV and the loop betoken the mesoporous nature of the synthesized nanowires Figure 7-16a). The calculations indicate that textural profile of nanowires exhibits mesoporosity (the 58.9% contribution to the V_p) with the highest part within R = 10 - 25 nm − 3 times as high as within R = 1 − 3 nm, while the macropores' share is at 37.7 % of the V_p (Figure 7-16b). Correspondingly, the surface area and total pore volume are 31 m^2/g and 0.087 cm^3/g. This is because of the consolidation of raw amorphous carbon-contaminated nanowires while being calcined at 650 °C.

Similar PSD with essential contribution of macroporosity stated and the BET curve shape were observed by Jin and Guo [48] in mesoporous 3C-SiC: $V_p = 0.13$ cm^3/g and $S_{BET} = 47$ m^2/g. However, their 3C-SiC ($d_{Scherrer} = 50$ nm) was synthesized in the form of whiskers through the carbothermal (1250 °C) sol-gel method involving TEOS, oxalic acid and phenolic resin. The simultaneous occurrence of large meso- and macropores is borne out with the view on the adsorption energy distribution illustrated on Figure 7-16c. According to the BET concept, the adsorption energy is identical to the heat of condensation of the adsorbate over the multilayers. The narrow low-energy peak at E < 2 kJ/mol shows that there are uniform macropores (25 < R < 100 nm) and mesopores at high radii (10 < R < 25 nm), whereas the lower signal at E = 3.8 kJ/mol is attributed to the rest of mesopores region - 1 < R < 10 nm at less uniformity due to a large energy lapse (E = 2-8 kJ/mol) of the corresponding peak. Additionally, the latter type of mesopores less participates in the nitrogen adsorption process − hence, gaps are responsible mainly for the pores over R > 10 nm, and slits in the nanowires structure are dominant.
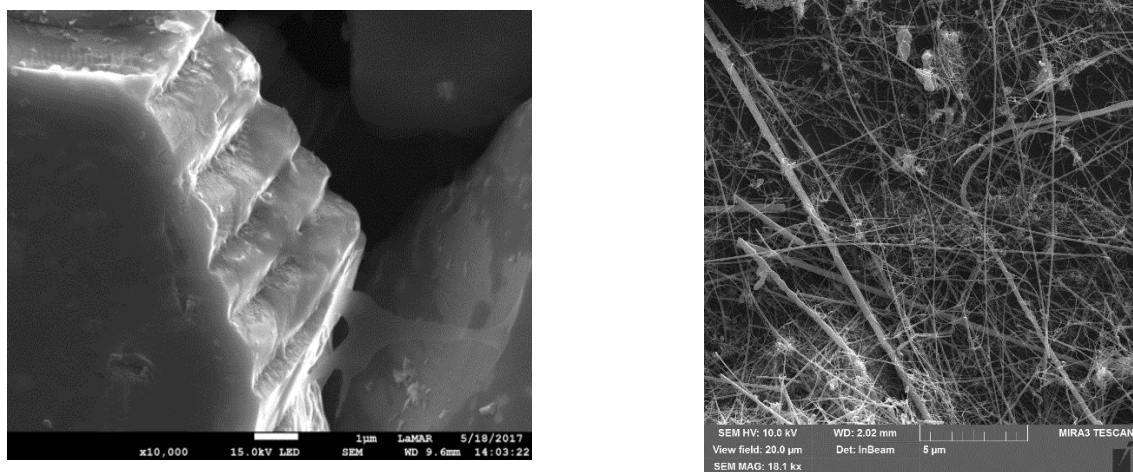

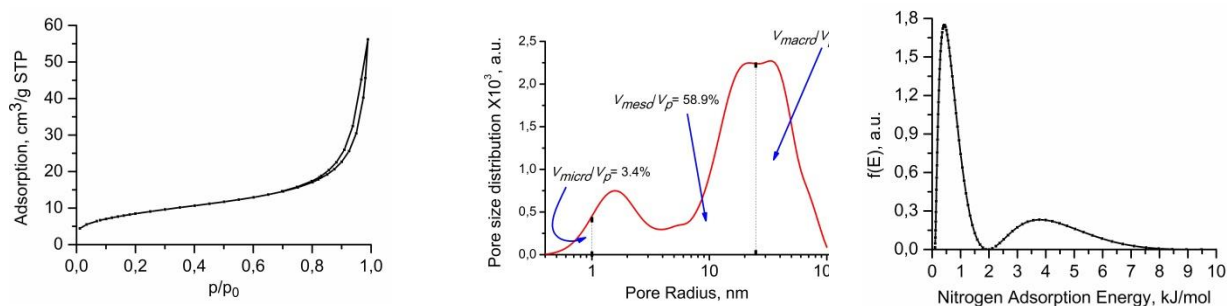**Figure 7-15. The SEM image of commercial SiC SA** *(a)* **and SiC NW** *(b)*

Figure 7-16. The BET curve *(a)*, **pores size distribution** *(b)* **and adsorption energy distribution** *(c)* **of SiC NW.**

The average gold particle size in Au@SiC SA and Au@SiC NW is 3.5 nm (Figure 7-17a), whereas the NPs are well distributed. At room temperature Au nanoparticle do not tend to aggregation. And during heating or mechanical impact, they can migrate leaving a surface and/or forming aggregates – both phenomena are undesirable.
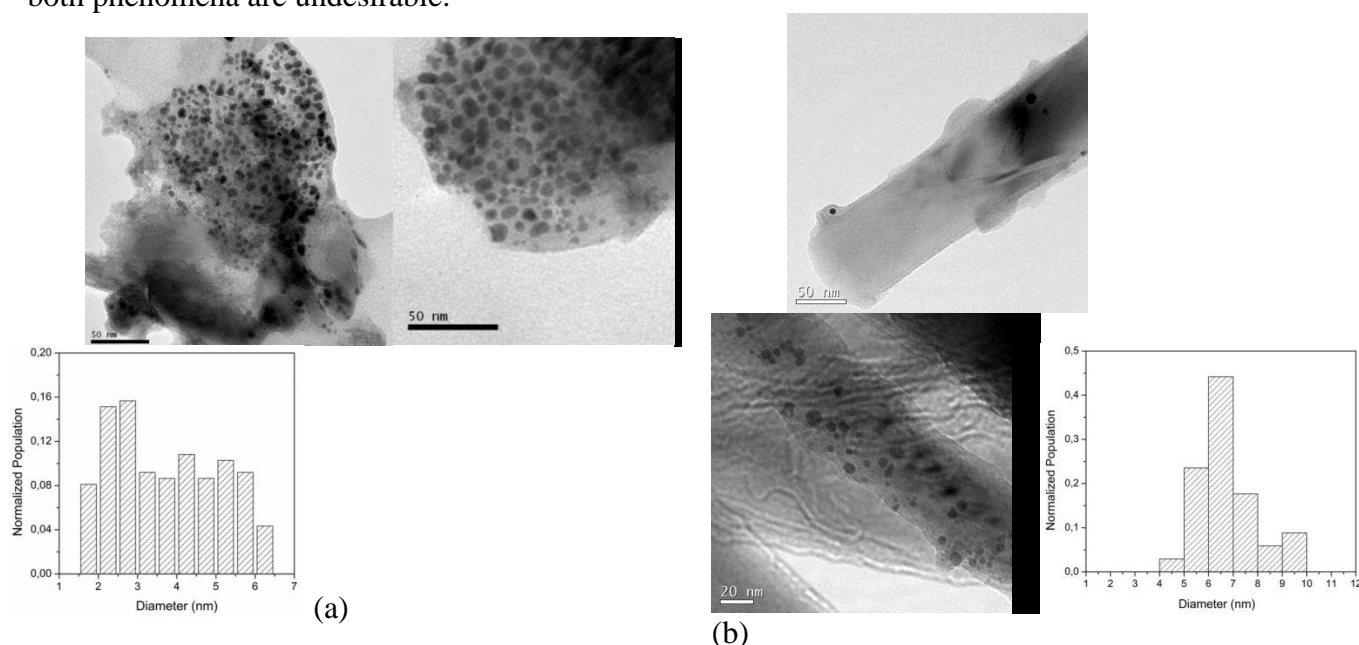

Figure 7-17. The TEM images of Au@SiC SA *(a)* **and Au@SiC NW** *(b)* **before reaction with respective Au particle size distribution profiles on surface.**

We undertook to examine the TEM images for Au@SiC SA and Au@SiC NW after the reaction (4h) to see, if gold nanoparticles are well-behaved to maintain the structure stability of the catalysts. The images have revealed separation and migration of gold nanoparticle from the SiC matrix's structure (Figure 7-18a). As opposed, the nanowires maintain gold nanoparticles after long-term stirring in water (Figure 7-18b). It led us to avoid kinetics studies with Au@SiC SA due to the lack of compositional stability and doubts in the CO_2 reduction results interpretations.
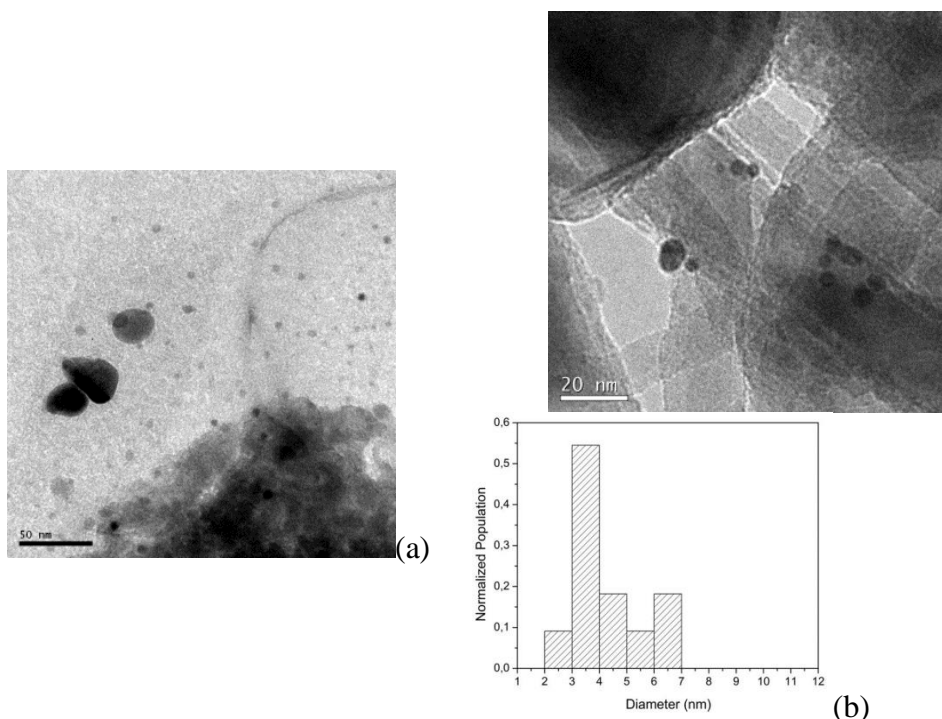
Figure 7-18. The TEM images of Au@SiC SA *(a)* and Au@SiC NW *(b)* after reaction with respective Au particle size distribution profiles on surface.

As it can be seen from the results presented high-temperature approach of SiC preparation not allowed to obtain particles within nanosize boundary. Therefore, they cannot be used as carriers in biomedical application. Nevertheless, we succeed to obtain nanodots of Au evenly distributed on SiC surface. Such materials demonstrated very promising results in the photo-catalytical reduction of CO_2 with water to organic compounds. For example, Au@SiC NW gives up to 66.5 % of ethanol at room temperature, Table 7-5.

Table 7-5. The peak area percentage of intermediate organics during the photocatalytic reduction of CO_2 – CH_3OH, ethanol C_2H_5OH and acetone $(CH_3)_2C=O$

Sample	Compounds, %			
	Methanol	Ethanol	Acetone	Rest
SiC SA	2.0	58.9	8.5	30.6
SiC NW	4.4	26.5	45.0	24.1
Au@SiC NW	1.3	66.5	2.2	30.0

7.3. WP3 Synthesis of photoactive binding molecules

7.3.1. Introduction (in Portuguese)

Grupos protetores fotorremovíveis (chamados de fotoentregador, fotocliváveis ou fotoativáveis) são compostos que, na presença de uma radiação eletromagnética específica, são capazes de clivar seletivamente uma ligação. Devido a essa propriedade, estas moléculas são conhecidas por permitir a liberação controlada de outros compostos químicos tais como bioagentes (neurotransmissores, moléculas de sinalização celular), inseticidas, feromônios, entre outros [49].

Os critérios para um composto ser um bom grupo fotorremovível (PPG, do inglês Protecting Photoremovable Group) são: forte absorção em comprimentos de onda acima de 300 nm, devem ser

estáveis no meio reacional durante a fotólise, atravessar barreiras biológicas (membranas celulares); afinidade a componentes alvo específicos: locais de ligação em células cancerosas ou o local ativo de uma enzima; os subprodutos devem ser transparentes ao comprimento de onda de irradiação.

Como exemplos, grupos cumarina-4-ilmetil são compostos estáveis, com propriedades fluorescentes. Skwarczynski *et al.* desenvolveram um trabalho envolvendo a ativação pela luz visível do paclitaxel (antitumoral) ligado à cumarina. Esta estratégia consiste na clivagem da ligação benzílica pela luz que, por sua vez, permite a liberação do fármaco no local de interesse [50]. Grupos derivados de *o*-nitrobenzeno também são comumente utilizados como espécies fotoclaváveis.

Para a funcionalização dos nanodiamantes, a molécula chave responsável para a liberação controlada de fármaco em questão deverá ser fotorremovível (PPGs) para posteriormente fazer o *link* entre a superfície do ND à molécula bioativa desejada. Entre as porções fotoclaváveis mais populares através das quais se ligam biomoléculas consiste em um grupo contendo uma porção *o*-nitrobenzila, devido às propriedades únicas da função nitro na posição *orto* incluindo sua estabilidade sob luz ambiente, sua clivagem limpa após exposição à irradiação UV, e as reações de fragmentação de nanossegundos que sofre na fotoexcitação.[29]
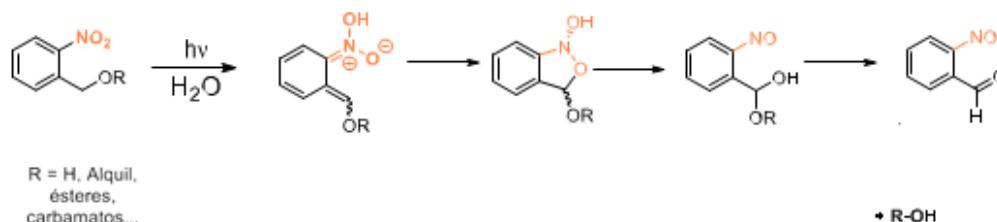
Equation 2. Mecanismo proposto da fotoclivagem de grupos *o*-nitrobenzila

Desta forma, propomos a preparação de dois derivados de um álcool benzílico (**1**), sendo o primeiro a partir da incorporação de um grupo funcional alcino (2) a um grupo hidroxila e incorporando um grupo azida (3), para duas estratégias distintas de imobilização à superfície de NDs.
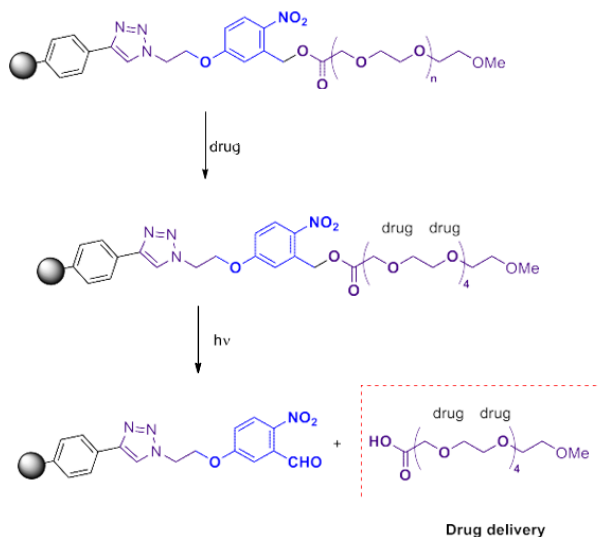
Equation 3. Esquema geral para a preparação de nanodiamantes funcionalizados com grupo fotorremovível para *drug delivery*

A porção em azul consiste no grupo fotoclaável, a porção roxa é referente à cadeia oxialquílica

cuja função é aumentar a solubilidade dos NDs em meios biológicos, adsorver o medicamento através de interações de hidrogênio e diminuir a hidrofobicidade e consequentemente evitar com que os NDs se agreguem.

O primeiro fragmento pode ser ancorado à superfície de ND, através de uma reação de esterificação entre um grupo OH livre presente no ND e um fragmento contendo grupo azida e uma função ácido carboxílico, na presença de um ativador de ácido carboxílico como EDC e DCC e DMAP como base, obtido como produto o ND-N$_3$. As moléculas orgânicas sintetizadas serão caracterizadas por RMN de ^{1}H, RMN de ^{13}C e infravermelho.

Deste modo, o grupo fotorremovível contendo um grupo alcino pode ser ancorado ao ND-N$_3$ através de uma reação de *click chemistry*, metodologia já descrita na literatura para obtenção de 1,2,4-triazóis, compostos conhecidos por suas aplicações biológicas. Assim, a preparação dos *linkers* fotorremovíveis será descrita a seguir.

O desenvolvimento dinâmico dos sistemas de liberação de medicamentos utilizando NDs como veículos abre perspectivas de novas formulações de medicamentos para combater doenças como o câncer e diabetes. Além disso, o uso da luz visível ou ultravioleta para a liberação controlada de fármacos na tentativa de minimizar os problemas causados pela administração convencional (toxicidade e resistência bacteriana) é uma estratégia interessante na presença de grupos fotossensíveis [49]. Visto também a promissora aplicação dos materiais nanoestruturados à base de carbono em Química Medicinal, propõe-se neste projeto a síntese de nanodiamantes funcionalizados com compostos orgânicos fotossensíveis.

7.3.2. Preparação dos linkers fotorremovíveis

O composto de partida tanto para o alcino quanto para a azida fotorremovíveis foi o 5-hidroxi-2-nitrobenzaldeído, comercialmente disponível, e em seguida sintetizou-se o álcool 5-hidroxi-2-nitrobenzílico através de uma reação de redução (Esquema 5).
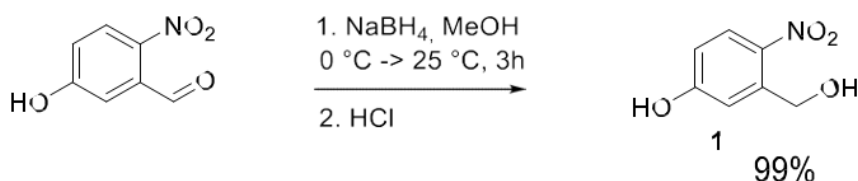
Equation 4. Preparação do álcool 5-hidroxi-2-nitrobenzílico, precursor para os demais grupos fotorremovíveis

A obtenção do álcool (**1**) se deu a partir da redução do aldeído 5-hidroxi-2-nitrobenzaldeído (1,0 equivalente), em metanol (0,15 M) na presença de boroidreto de sódio (4,0 equivalentes) em metanol como solvente a 0 °C. Em seguida, a mistura reacional ficou sob agitação à temperatura ambiente por 3 horas até que todo material de partida pudesse ser convertido no produto (acompanhando-se o curso da reação por CCD, eluente: hexano/AcOEt 8:2). Evaporou-se o solvente em um rotaevaporador sob pressão reduzida e em seguida, adicionou-se uma solução de HCl 1,0 M até atingir o pH 6. Extraiu-se a solução com AcOEt (3 vezes) e a fase orgânica foi secada com sulfato de sódio anidro. Por fim, o solvente foi removido em um rotaevaporador e o produto final consistiu em um sólido amarelo (rendimento quantitativo).

Pela análise do espectro de RMN de ^{1}H, pôde-se observar a evidência reacional a partir do desaparecimento do sinal característico do H de aldeído em torno de 10,0 ppm e o aparecimento de um sinal em 4,82 ppm referente aos hidrogênios benzílicos, além de um sinal largo em 6,54 ppm característico de hidrogênio da hidroxila (Figure 7-19).
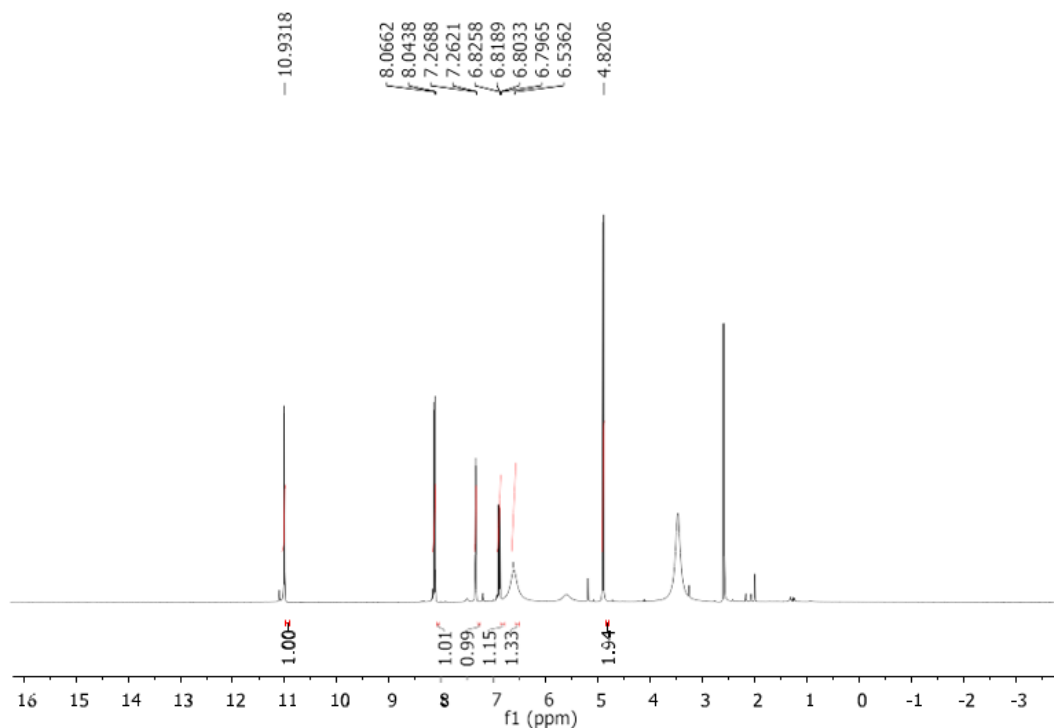
Figure 7-19. Espectro de RMN de ¹H do álcool 5-hidroxi-2-nitrobenzílico 1 (DMSO-*d₆*, 400 MHz)

Pela análise do espectro de RMN de ¹³C, pôde-se observar sinais entre 163-114,3 ppm referentes aos carbonos aromáticos e um sinal em 60,8 referente ao carbono benzílico.
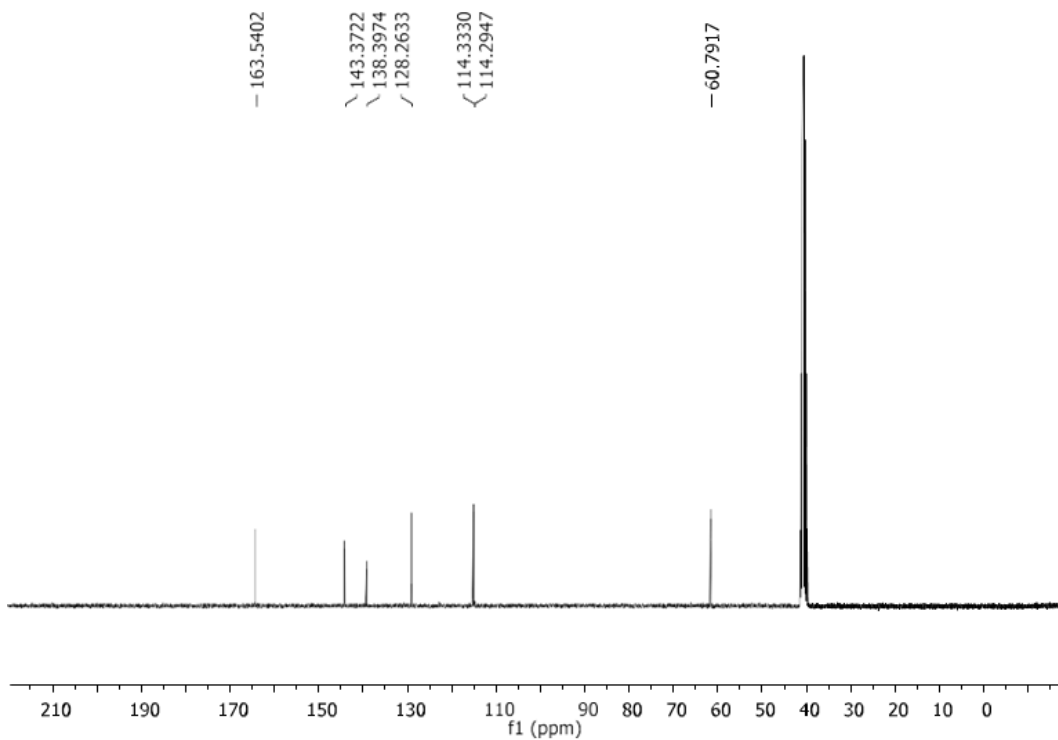
Figure 7-20. Espectro de RMN de ^{13}C do álcool 5-hidroxi-2-nitrobenzílico (DMSO-*d₆*, 100 MHz)

Pela análise do espectro na região do infravermelho, pôde-se observar uma banda em 3293 referente à presença de grupos hidroxila, em 1600 cm^{-1} referente ao estiramento C=C na região de aromáticos, em 1313 cm^{-1} referente ao grupo nitro. Além disso, não se observou banda característica de aldeídos (estiramento C=O na região de 1700 cm^{-1}).
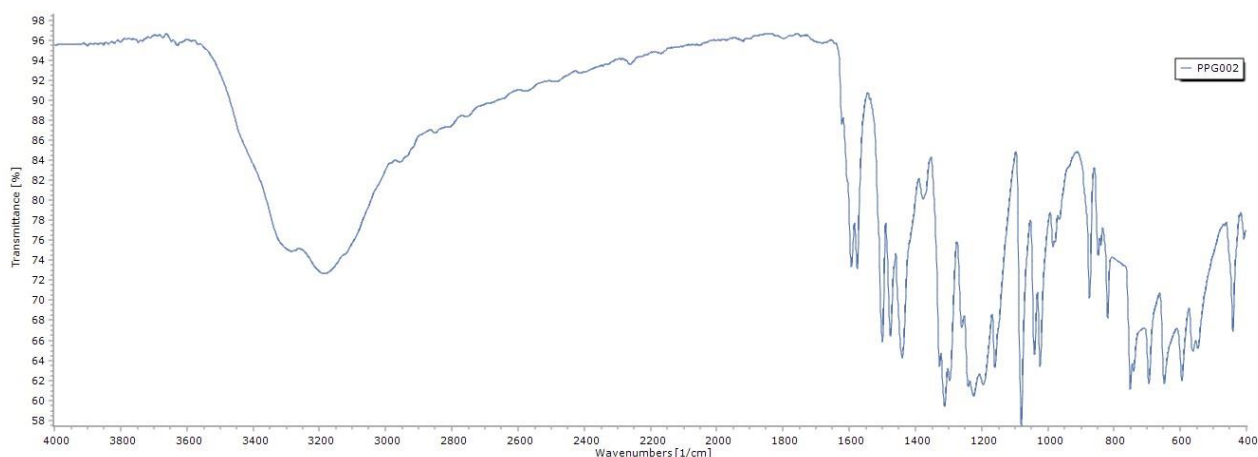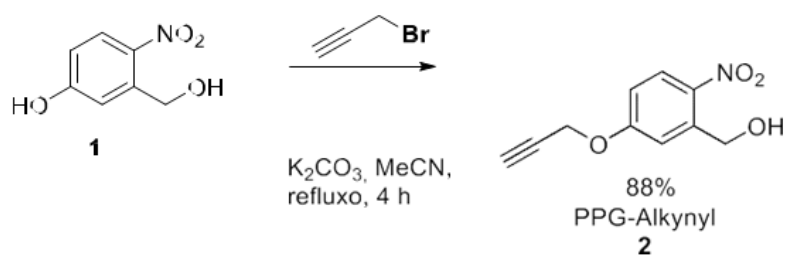

Figure 7-21. Espectro de Infravermelho do álcool 1.

7.3.3. Development of click-chemistry procedures for immobilization of PRL

Preparação do alcino

Tendo o álcool em mãos, previamente caracterizados, prosseguiu-se com a obtenção do éter propargílico **2** (PPG-Alkynyl) a partir da alquilação do mesmo com brometo de propargila, como é mostrado no Esquema 6.[31]

Equation 5. Preparação do grupo fotorremovível contendo o grupo alcino 2 (PPG-Alkynyl)

A metodologia consistiu na preparação da solução do álcool 1 (1,0 equivalente) em acetonitrila (0,5 M) sob agitação vigorosa. Em seguida adicionou-se bicarbonato de potássio (1,5 equivalente), éter de coroa (0,15 equivalente), agitando por meia hora. Adicionou-se o brometo de propargila (1,2 equivalente) e a reação ficou em refluxo por 4 horas. Após o fim da reação (acompanhada por CCD, eluente Hex/AcOEt 8:2), evaporou-se o solvente sob pressão reduzida e em seguida o produto foi solubilizado em uma pequena quantidade de diclorometano e purificado através de uma coluna filtrante, obtendo-se um sólido amarelo com 88% de rendimento.

Pela análise do espectro de RMN de ^{1}H, pôde-se observar um simpleto em 5,03 ppm referente

aos hidrogênios benzílicos; um dupleto centralizado em 4,83 ppm (J = 2,32 Hz) referente aos hidrogênios metoxílicos, e por fim, o aparecimento de um tripleto centralizado em 2,61 ppm (J = 2,28 Hz) referente ao H metínico.
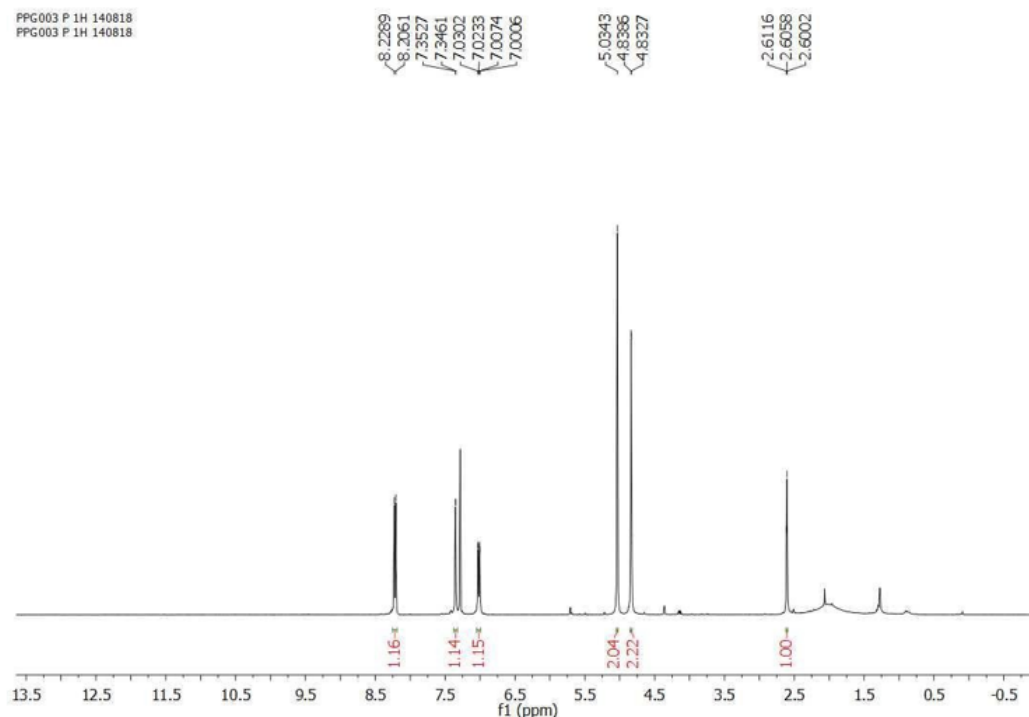

Figure 7-22. Espectro de RMN de ¹H do grupo fotorremovível-alquinil (PPG-Alkynyl)

(CDCl₃, 400 MHz)

Pela análise do espectro de RMN de ¹³C, pôde-se observar sinais entre 161,9-114,0 ppm referentes aos carbonos aromáticos; dois sinais em 77,2 e 77,1 ppm referente aos carbonos alquínicos; um sinal em 62,9 ppm referente ao carbono benzílico; e um sinal em 56,3 ppm referente ao carbono sp³ do grupo propargila.

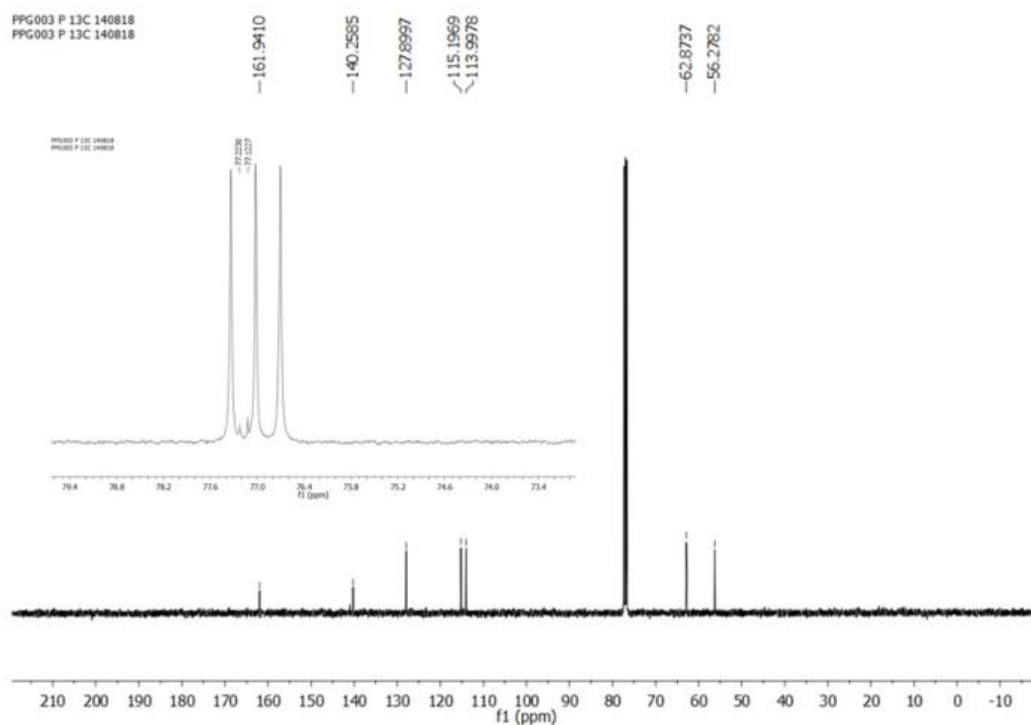Pela análise do espectro de infravermelho, pôde-se observar uma banda em 2125 cm⁻¹, característica de grupos alcinos.

Figure 7-23. Espectro de RMN de ^{13}C do grupo fotorremovível-alquinil (PPG-Alkynyl)
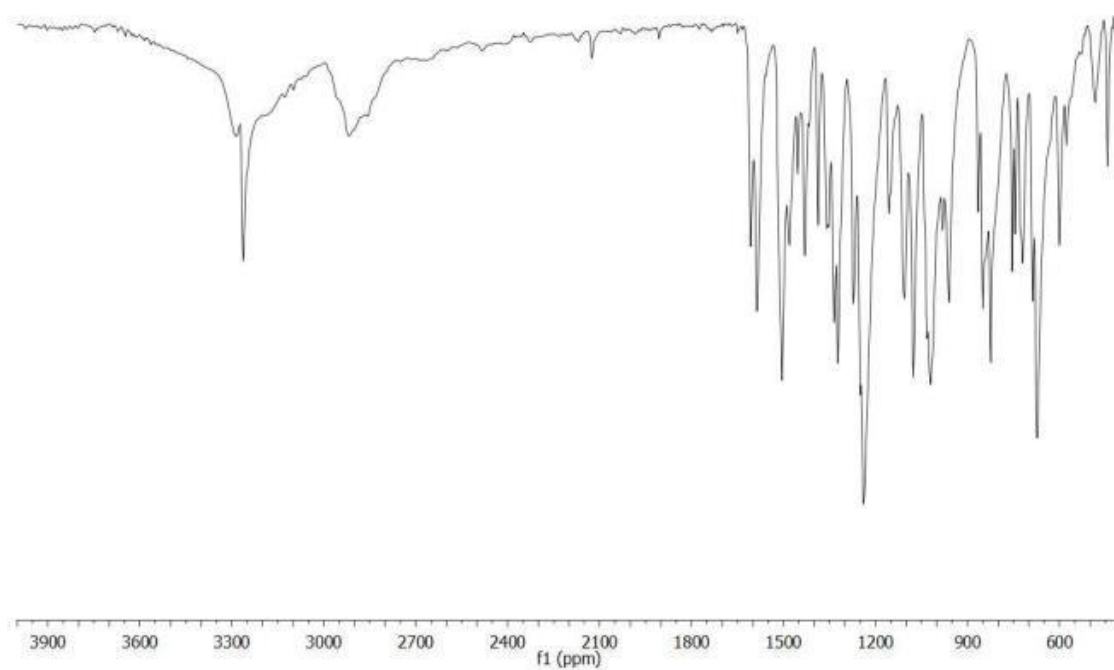(CDCl$_3$, 100 MHz)

Figure 7-24. Espectro de Infravermelho do composto 2 (PPG-Alkynyl)

O segundo *linker* fotorremovível consiste em uma azida terminal para ancorar em superfícies de nanodiamantes contendo um alcino terminal (ND-Alkynyl). A estratégia utilizada consistiu em uma reação de alquilação do fenol utilizando 1,3-dihaletos, que por sua vez, ao reagir com um grupo azida, obtém-se a azida fotorremovível (PPG-N$_3$).

Preparação do grupo azida

A obtenção da azida foi realizada a partir de duas etapas: a primeira consistiu na alquilação do aldeído com um haleto terminal e a segunda a reação de obtenção da azida. Para a obtenção do haleto a reação foi otimizada. Em um primeiro momento, utilizou-se uma metodologia já descrita na literatura partindo-se de 1,3-diiodopropano, uma vez que o iodo é um bom grupo abandonador e desta forma, obter-se-ia o composto **3** almejado.

Baseado na metodologia descrita por Yan e colaboradores, utilizou-se 1,3-diiodopropano como agente alquilante (eletrófilo), uma vez que o iodo é um bom grupo abandonador.[32] As condições reacionais da literatura consistiu no uso de um pequeno excesso (1,2 equivalente) do eletrófilo e base (1,5 equivalente) em DMF (0,67 M) como solvente a 25 °C. A reação foi acompanhada por CCD e após 4 horas de reação, todo o material de partida havia sido consumido. A caracterização do composto obtido foi feita por RMN de ^{1}H e para a surpresa, o produto obtido era de dimerização, ou seja, o haleto intermediário sofreu ataque intermolecular pelo fenóxido. Outras tentativas foram realizadas na tentativa de diminuir a reatividade do sistema, como a diminuição da concentração e temperatura, variando as bases (como o uso de carbonato e bicarbonato de potássio), e mesmo assim os resultados não foram almejados.
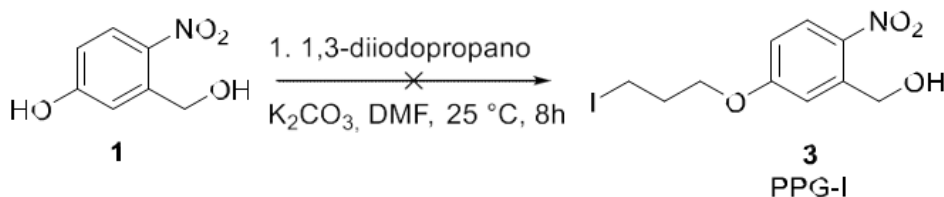
Equation 6. Tentativa de obtenção do álcool 5-(3-Iodopropóxi)-2-nitro benzílico, intermediário para a obtenção da azida

Uma outra alternativa consistiu no uso de um eletrófilo menos reativo. Desta forma, utilizou-se o 1,3-dibromopropano, uma vez que o bromo é menos reativo que o iodo. Após diversas tentativas modificando temperatura, concentração e as bases, a condição ideal consistiu-se no uso de 4 equivalentes do eletrófilo, pequeno excesso (1,2 equivalente) de Cs$_2$CO$_3$, em DMF (0,13 M em relação ao reagente limitante), e após 36 horas, todo o material de partida havia sido consumido (acompanhamento da reação por CCD).
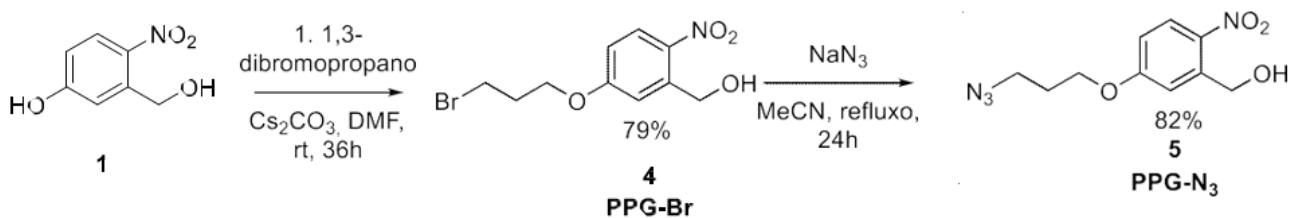
Equation 7. Preparação do álcool 5-(3-azidopropóxi)-2-nitro benzílico (PPG-N$_3$)

Após a caracterização do composto por RMN de ^{1}H e ^{13}C, a evidência de obtenção do produto

se deu através do desaparecimento do sinal largo em 10 ppm característico de hidrogênio fenólico; o aparecimento de hidrogênios alquílicos: um tripleto centralizado em 4,26 ppm referente aos hidrogênios metoxílicos (H_{10}), $J = 6,10$ Hz, um tripleto centralizado em 3,63 ppm referente aos hidrogênios metilênicos vicinais ao bromo (H_{12}), $J = 6,10$ Hz, um quinteto em 2,38 ppm referente aos hidrogênios metilênicos centrais (H_{11}), $J = 6,10$ Hz.
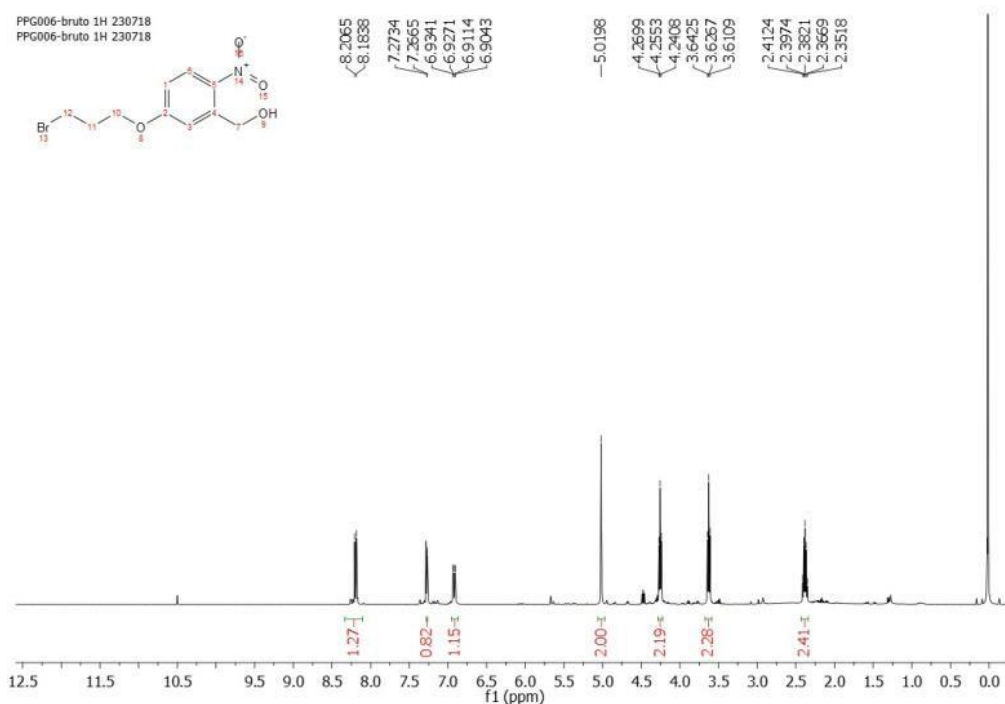

Figure 7-25. Espectro de RMN de ^{1}H do composto 4 (PPG-Br) (CDCl$_3$, 400 MHz)

Pela análise do espectro de RMN de ^{13}C pôde-se observar os carbonos alquílicos: 29,4 ppm referente ao C_{11}; 31,9 ppm referente ao C_{12} e 62,9 ppm referente ao carbono metoxílico.
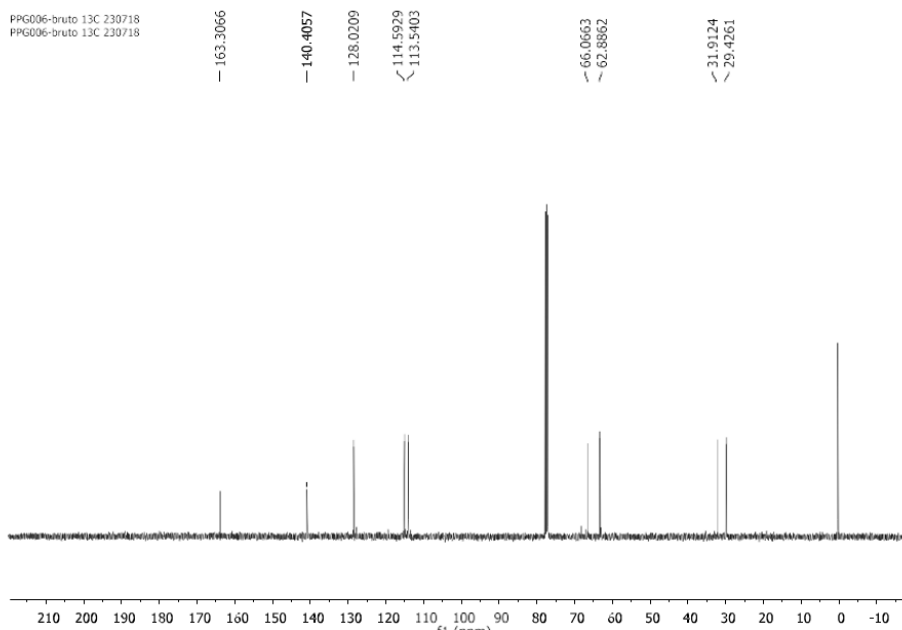
Figure 7-26. Espectro de RMN de ^{13}C (CDCl$_3$,100 MHz) do composto 4 (PPG-Br)

Tendo em mãos o intermediário **4** (PPG-Br), a próxima etapa consistiu na obtenção da azida (PPG-N$_3$) utilizando-se uma metodologia da literatura desenvolvida por Shakiba e colaboradores[33]. Em uma solução contendo o intermediário **4** em MeCN, na presença de 5,0 equivalentes de azida de sódio, a mistura foi mantida em agitação e sob refluxo por 24 horas (a reação foi acompanhada por CCD). O solvente foi removido sob pressão reduzida e o sólido obtido extraído com água para remover o excesso de azida de sódio e o produto obtido foi então caracterizado por RMN de ^1H e ^{13}C.

Pela análise do espectro de RMN de ^1H, pôde-se observar a sutil mudança na região alquílica, onde o bromo foi substituído pela azida (Figure 7-27). Pôde-se observar tripleto em 4,20 ppm, $J = 6,0$ ppm; referente aos hidrogênios metoxílicos, um tripleto em 3,57 ppm, $J = 6,2$ Hz referente aos hidrogênios vicinais ao grupo azida; um quinteto centralizado em 2,12 ppm, $J = 6,2$ Hz, referente aos hidrogênios metilênicos, $J = 6,2$ Hz.
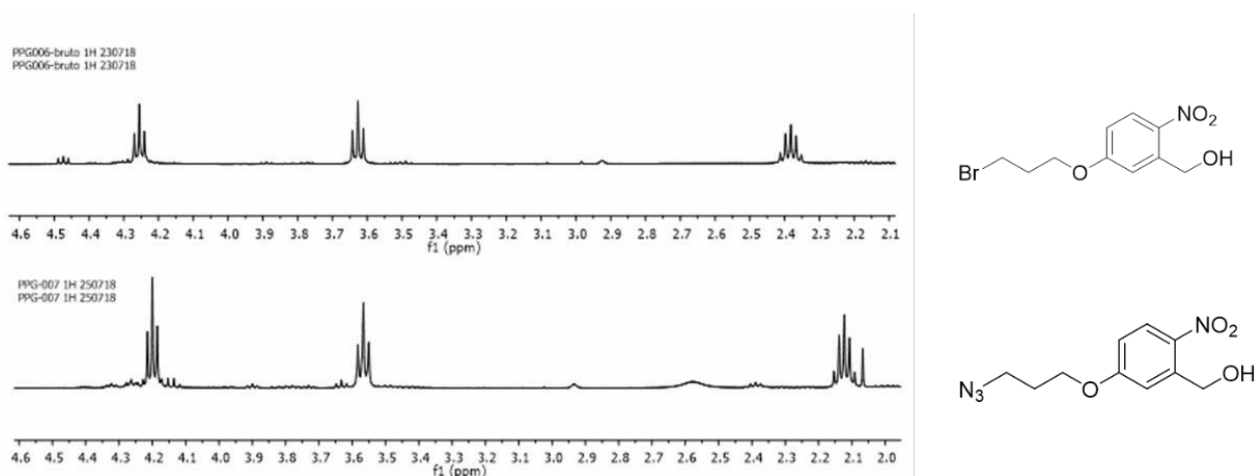

Figure 7-27. Expansão da região alquílica do intermediário PPG-Br e PPG-N$_3$

Pelo espectro na região do infravermelho, a evidência reacional pôde ser observada através da banda em 2101 cm^{-1}, característico do grupo azida.
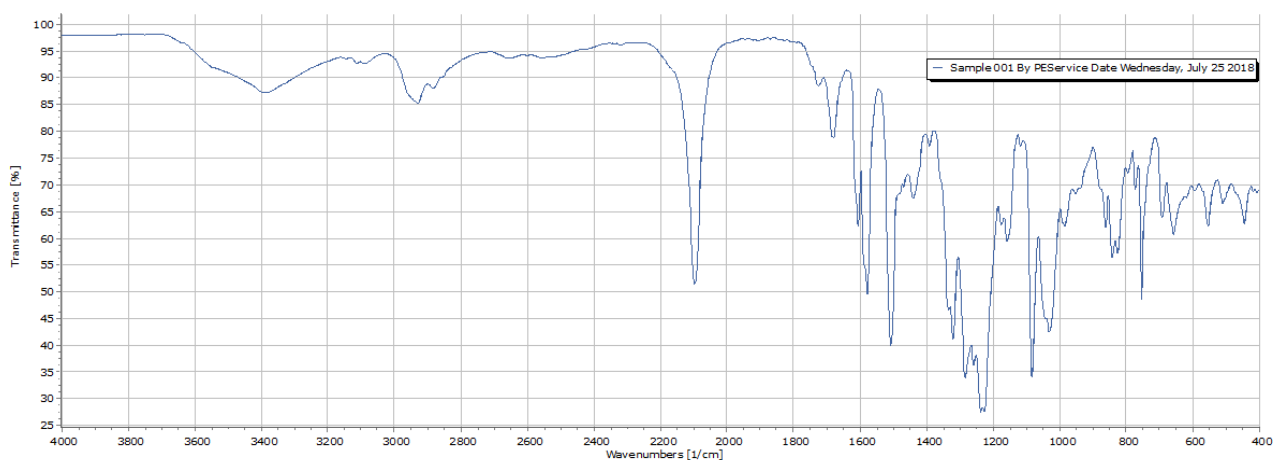

Figure 7-28. Espectro de infravermelho do composto PPG-N$_3$

Preparação do 4-azido-N-(3,4-dihydroxyphenethyl)-2,3,5,6-tetrafluorobenzamide (1)

To a solution of dopamine hydrochloride (113.4 mg, 0.6 mmol) in DMF (4 mL) were added TEA (108.4 mL, 0.77 mmol) and N-succinimidyl 4-azidotetrafluorobenzoate (200 mg, 0.6 mmol). The mixture was stirred overnight at room temperature under argon. Then water was added, and the resulting precipitate was filtered and washed with water several times and then dried at 1008C carefully to give 203 mg (91.4% yield) of white powder, Equation 8. H NMR (300 MHz, DMSO): d=8.96–8.92 (t, 1H, amide), 8.80 (s, 1H, OH), 8.74 (s, 1H, OH), 6.65–6.13 (m, 2H, arom) 6.49–6.46 (d, 1H, arom), 3.42–3.36 (q, 2H, CH$_2$NHCO), 2.65–2.60 ppm (t, 2H, CH$_2$).
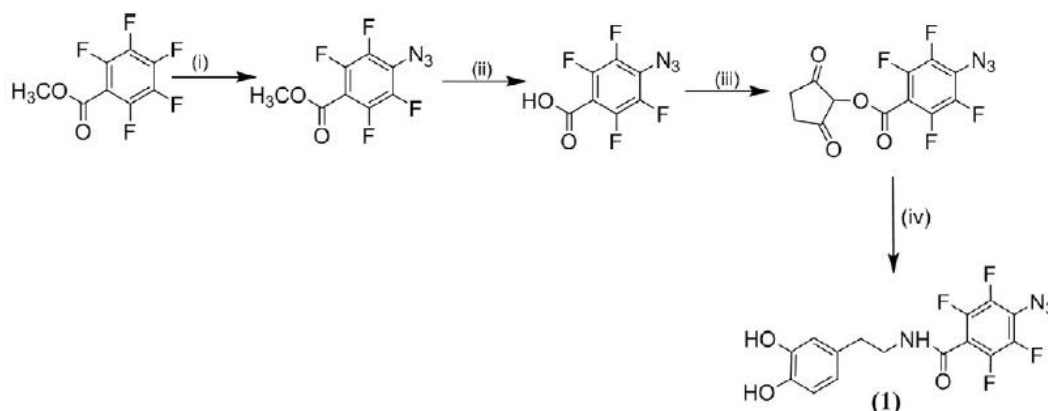
Equation 8. Preparação do 4-azido-N-(3,4-dihydroxyphenethyl)-2,3,5,6-tetrafluorobenzamide

7.3.4. Preparação de um 1,2,4-triazol fotorremovível

Tendo em mãos os grupos fotorremovíveis para serem imobilizados nos NDs, testou-se uma reação de *click chemistry* entre o composto **2** (PPG-Alkynyl) e o ácido 4-azidobenzóico (Esquema X) para primeiro testar a reatividade dos grupos fotorremovíveis neste tipo de reação e em segundo para tentar ancorar ao ND pela porção ácida através de reações de esterificação.
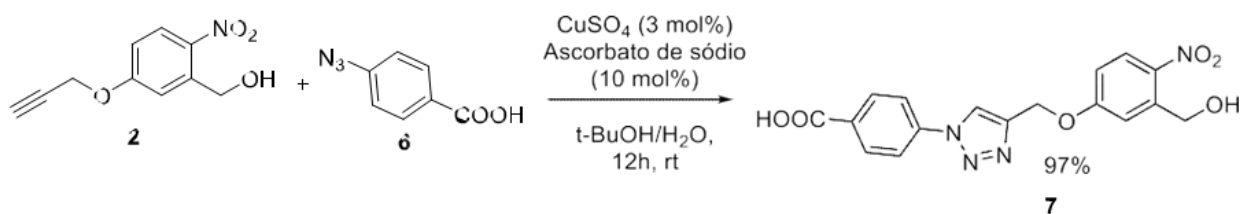
Equation 9. Reação *click chemistry* entre o composto 2 **(PPG-Alkynyl) e ácido azido benzóico: obtenção do 1,2,4-triazol fotorremovível** 7

A metodologia utilizada consistiu no uso de sulfato de cobre e ascorbato de sódio como catalisadores, uma vez que o Cu^{2+} é reduzido a Cu^{+1} pelo ascorbato *in situ* e desta forma se complexa ao grupo alcino diminuindo a energia do sistema para posteriormente formar o triazol frente ao grupo azida.

A reação ficou sob agitação por 12 horas e o sólido formado foi filtrado e lavado com água gelada e diclorometano, para eliminar as impurezas inorgânicas e orgânicas respectivamente. O sólido marrom isolado foi caracterizado por RMN de ^{1}H e ^{13}C.

A evidência reacional se deu através da análise do espectro de RMN de ^{1}H com o aparecimento de um simpleto em 9,09 ppm, referente ao hidrogênio da porção triazólica. O tripleto centralizado em 2,61 ppm, referente ao alcino desapareceu; os hidrogênios metoxílicos e benzílicos apareceram como simpletos em 5,44 e 4,86 ppm respectivamente.
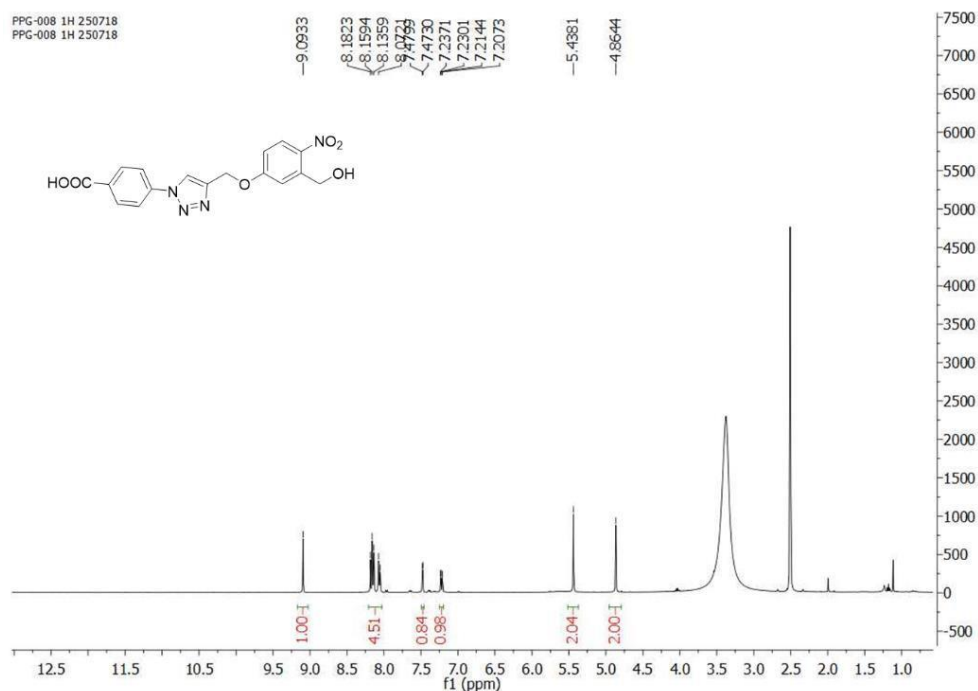
Figure 7-29. Espectro de RMN de ^{1}H do 1,2,4-triazol fotorremovível (X) (400 MHz, DMSO-d_6)

7.4. WP4. NDs particles activation and characterization.

7.4.1.   Introduction (in Portuguese)

Nanodiamantes (NDs) consistem em partículas de carbono com tamanho de aproximadamente 5 nm. Sua forma geral é esférica ou elíptica; no centro se encontra uma rede de diamante principalmente de arranjo cúbico, composta principalmente por carbono. Sua superfície se assemelha à estrutura de grafite enquanto o núcleo se assemelha à estrutura do diamante [51], Figure 7-30. A natureza versátil desses materiais está ligada à possibilidade de se adaptar de forma controlada as propriedades físicas e químicas dos materiais.

Figure 7-30 a) Estrutura interna do Nanodiamante; b) superfície "like" grafite e a imagem de nanodiamantes individuais agrupados e sua representaçã

Estudos recentes mostram que a superfície contém grupos funcionais como hidroxilas, epóxidos, cetonas, entre outros. Desta forma, é possível funcionalizar sua superfície através de ligações covalentes com compostos orgânicos [51]. Suas principais va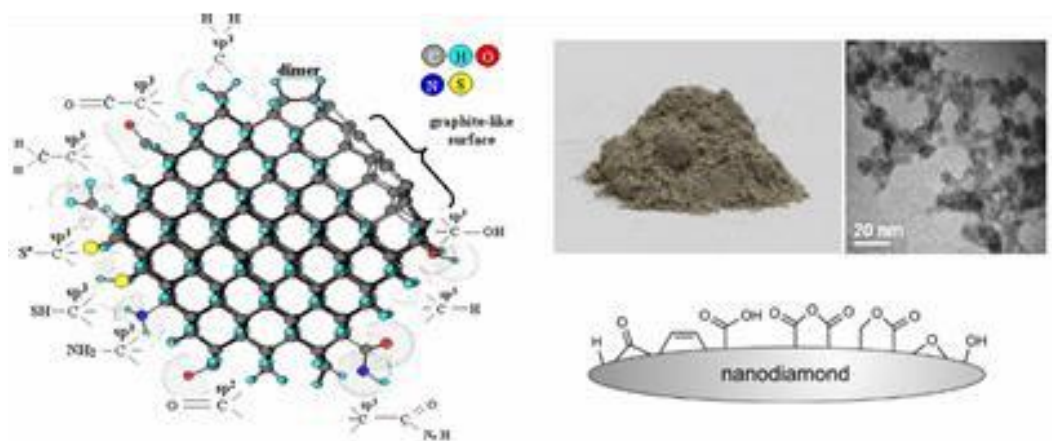ntagens são o baixo custo de produção, alta biocompatibilidade e baixa citotoxicidade [52]. Com isso, estas partículas têm sido amplamente estudadas para aplicações principalmente biológicas e eletrônicas.

O potencial terapêutico dos NDs como transportadores de droga foi mostrado pela primeira vez por Ho e colaboradores que conseguiram sintetizar NDs adsorvidos com doxorrubicina, medicamento utilizado na terapia contra o câncer [3]. Diabetes e câncer são apenas dois exemplos em que o tratamento com o fármaco funcionalizado com NDs podem ter um potencial terapêutico real [4]. A insulina adsorvida sobre NDs foi mostrada para dessorver ao longo do tempo. Daqui se conclui que este último sistema pode potencialmente servir como uma terapia de libertação controlada para os diabéticos, negando assim a necessidade de injeções de insulina [6].

7.4.2. Surface chemistry of nDS

Os nanodiamantes foram obtidos comercialmente com "Alitex" (Israel), e "DAICEL" (Japão), Figure 7-31 e em sua forma pura, estes materiais apresentam baixa quantidade de grupos funcionais reativos frente a compostos orgânicos. Assim, diversos grupos de pesquisa desenvolveram metodologias para aumentar a quantidades de grupos funcionais, como grupos amino (ND-NH$_2$), ácidos carboxílicos (ND-COOH) e hidroxilas (ND-OH) em suas superfícies.

Figure 7-31 Suspension of nanodiamonds in water from DAICEL, Japan

Pelo espectro de infravermelho do ND-puro, pôde-se observar uma banda em 3424 cm^{-1} característico de hidroxilas; uma banda em 1627 referente à grupos cetônicos; uma banda em 1095, característica de ligações C-O *bending* (Figure 7-32).

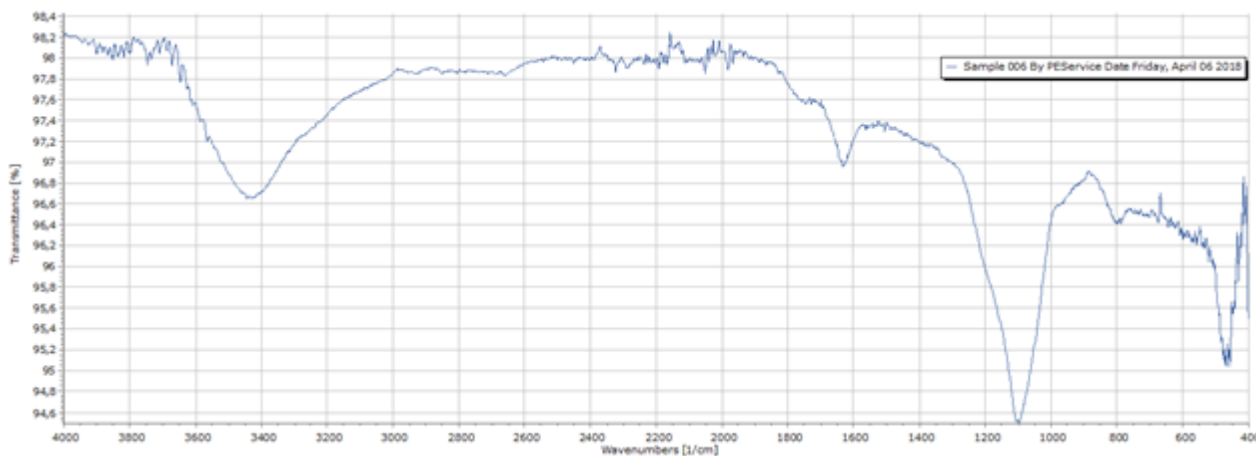**Figure 7-32. Espectro de infravermelho do ND comercial**

Desta forma, propõe-se neste tópico, sintetizar NDs ricos em grupos carboxílicos (ND-COOH) e ricos em hidroxilas (ND-OH) para serem ancorados a compostos orgânicos (linkers).

7.4.3.   Preparação dos ND-COOH

Preparação dos ND-COOH com Plasma Cleaner

Os nanodiamantes são sólidos insolúveis na maioria dos solventes. Desta forma, para escolher

um procedimento experimental para a oxidação de sua superfície requer alguns cuidados, pois o uso de agentes oxidantes (como permanganato de potássio, reagente de Jones, entre outros) se torna inviável devido a problemas de purificação. Sendo assim, decidiu-se buscar por duas alternativas: uso de *Plasma Cleaner,* que gera oxigênio nascente e assim poderia oxidar a superfície dos NDs. A segunda consiste na oxidação térmica, onde os NDs, na presença de oxigênio e temperaturas elevadas podem ser oxidados.

O uso de plasma de oxigênio é explorado na área de química de materiais. Devido ao seu comportamento de não-equilíbrio e não-isotérmico, esses gases ionizados podem levar a novos resultados quando usados como como uma alternativa para o tratamento de superfícies de materiais. Alguns trabalhos relataram seu uso em grafites, microesferas de carbono e carbonos vítreos. Como fonte de plasma, utilizou-se o equipamento *Plasma Cleaner,* uma câmara que sob vácuo e na presença de radiofrequência, emite plasma.

Assim, decidiu-se primeiramente utilizar esta estratégia para os NDs, uma vez que estes consistem em materiais de carbono. Preparou-se uma suspensão de ND em água, sonicada por 30 minutos, e então dispersou-se em uma placa de Petri para a obtenção de um filme. Deixou-se no dessecador por 24 horas e então colocado em uma câmara geradora de plasma de oxigênio, *Plasma Cleaner.*

O filme foi deixado de 10 em 10 minutos, sob uma frequência específica, até completar uma hora. As amostras foram coletadas para posterior caracterização por infravermelho.

Pela análise do espectro de infravermelho das amostras, pôde-se observar que apenas a banda na região de 1025 cm^{-1} diminuiu, mas bandas características de grupos carboxílicos não foram detectados (Figure 7-33).

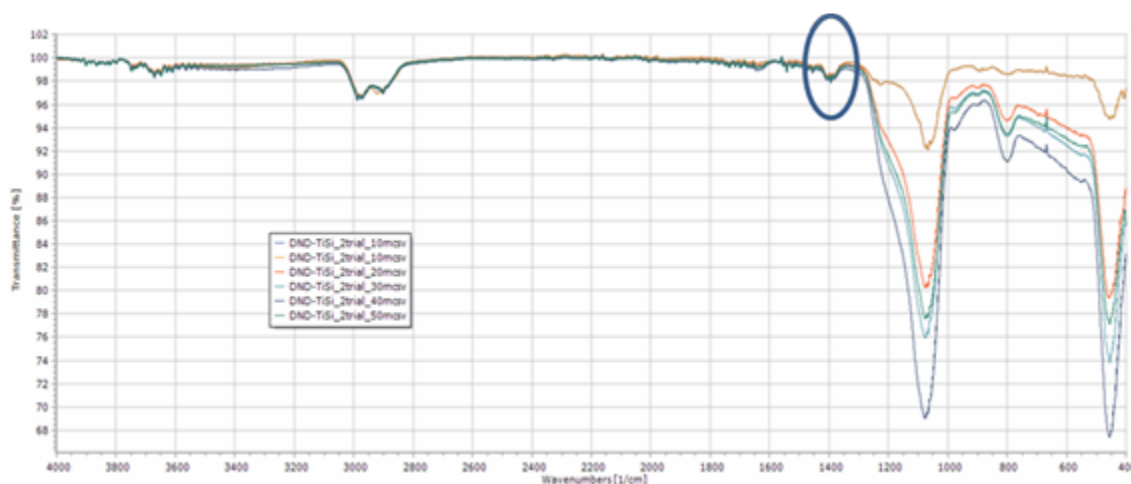**Figure 7-33. Monitoramento do tratamento com *Plasma Cleaner* por infravermelho (ATR)**

Uma outra alternativa consistiu da oxidação térmica, seguindo o protocolo experimental descrito por Ryan e colaboradores.[35]

Oxidação térmica de NDs

A oxidação térmica foi realizada através do aquecimento destes materiais na presença de O$_2$.[34,35]

A metodologia consistiu no aquecimento dos NDs, comercialmente disponíveis, em uma

mufla a 475 °C (Figure 7-34).

Figure 7-34. Protocolo descrito por Simpson e colaboradores para a oxidação térmica de NDs (Fonte: Adaptado de Ryan *et al.* 2018)

Após esfriar a 25 °C, uma amostra foi caracterizada por infravermelho (Figure 7-35). A principal mudança observada foi a formação de uma banda característica de ácido carboxílico (estiramento da carbonila em 1800 cm^{-1}).
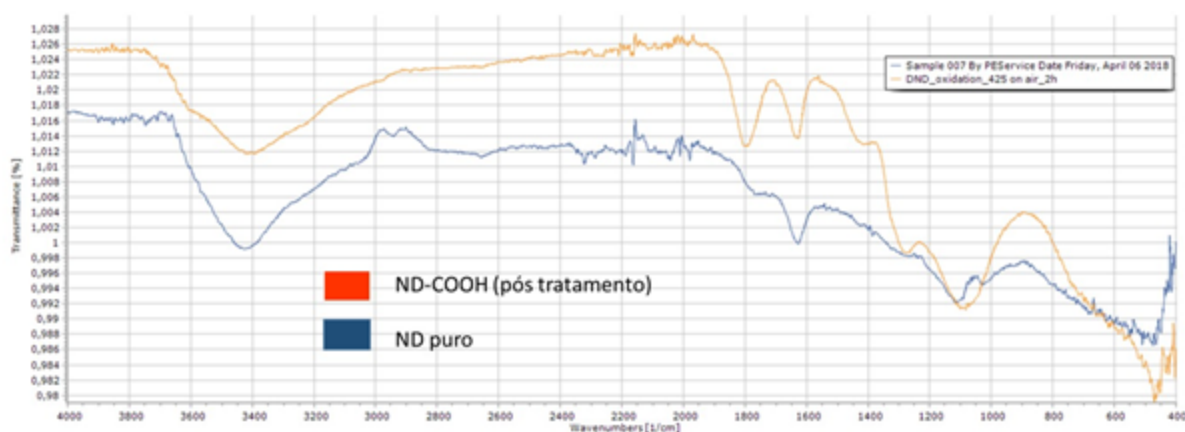
Figure 7-35. Espectro de infravermelho do ND-puro comercialmente disponível (azul) e do ND-COOH (laranja) pós tratamento de oxidação

A etapa seguinte consistiu no tratamento dos ND-COOH em meio ácido. Assim, preparou-se uma suspensão em uma solução de HCl (0,001 M) e sonificou-se por 40 minutos, para garantir a protonação de quaisquer grupos carboxilatos presentes na superfície. Centrifugou-se numa rotação de 12 mil rpm e lavou-se o sólido por cinco vezes com água Miliq, até a condutividade da suspensão chegar a zero.

Figure 7-36. Suspensão de ND-COOH em pH 3

7.4.4.   Characterization of ND-COOH suspensions

Posteriormente mediu-se a estabilidade desta suspensão pela análise de potencial Zeta, potencial eletrocinético utilizado para medir a estabilidade de suspensões, ou seja, potencial zeta é a diferença de potencial entre o meio de dispersão e a camada estacionária de fluido preso à partícula dispersa. A magnitude do potencial zeta indica o grau de repulsão eletrostática entre partículas adjacentes de carga similar em uma dispersão. Em partículas pequenas, um elevado potencial zeta conferirá estabilidade, isto é, a solução ou dispersão resistirá à agregação (referência 3 e 4 wiki). Pela Tabela 1, pôde-se observar o aumento da magnitude do potencial zeta, tanto os ND-COOH dispersos sem tratamento ácido, quanto em condições pós tratamento ácido.

Table 7-6. Potencial Zeta para os NDs e ND-COOH

Potencial Zeta	ND puro	ND-COOH	ND-COOH (pós tratamento ácido)
Medida 1	0,8 mV	-55.6, mV	-71,9 mV
Medida 2	-0,3 mV	-60,4, mV	-73,7 mV
Medida 3	-0,5 mV	-56,5, mV	-68,6 mV
Medida 4	0,2 mV	-44,5, mV	-67,6 mV

As medidas para os ND puros próximos de zero, nos mostra a baixa estabilidade coloidal, isto é, possuem uma maior tendência em coagular[36].

Por fim, realizou-se a dispersão dinâmica de luz (DLS), uma técnica física amplamente utilizada para medir o tamanho de partículas em solução ou suspensão. Os diâmetros encontrados obtidos foram próximos, tanto para os NDs puros quanto ND-COOH no valor de 48 nm.
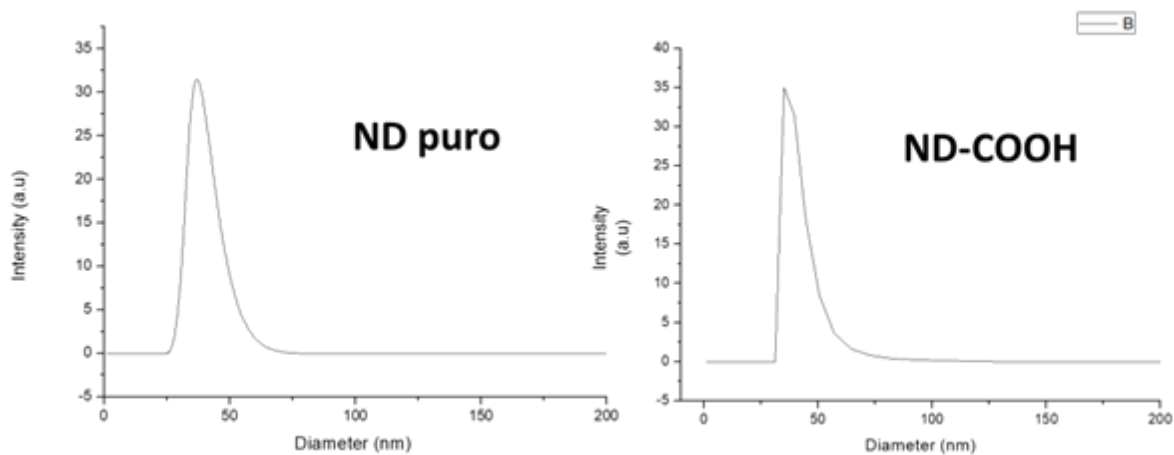
Figure 7-37. DLS dos ND puro e ND-COOH

7.4.5.   Preparação dos ND-OH

A preparação dos ND-OH se deu a partir da redução dos NDs ricos em grupos ácidos carboxílicos, os ND-COOH obtidos anteriormente na presença de um agente redutor. Para este procedimento, optou-se pelo uso de hidreto de lítio e alumínio (LiAlH$_4$), uma vez que este redutor é mais reativo[37].

Uma suspensão de ND-COOH em THF foi sonificada por 40 minutos e em seguida adicionou-se o redutor, numa razão de 1:1 (m/m). A mistura reacional ficou em agitação e sob refluxo por 24 horas, e posteriormente, o sobrenadante foi removido por centrifugação (12 mil rpm). O sólido obtido foi lavado três vezes, separado por centrifugação e o sólido foi tratado com NaOH 6,0 M, sob agitação a 90 °C *overnight*, tratada com HCl 0,1 M e lavada com água até atingir o pH neutro, e por fim, a suspensão obtida foi purificada através de lavagem com uma membrana semipermeável, permitindo

a troca iônica. O solvente foi removido sob pressão reduzida e o sólido obtido secado em alto vácuo por 24 h. Em seguida, caracterizou-se por infravermelho (Figura 22). Pôde-se observar a diminuição da banda característica de ácidos carboxílicos, além das demais bandas em 3400 referente ao estiramento OH, bandas nas regiões de 2900 cm^{-1} referente a C-H presentes.
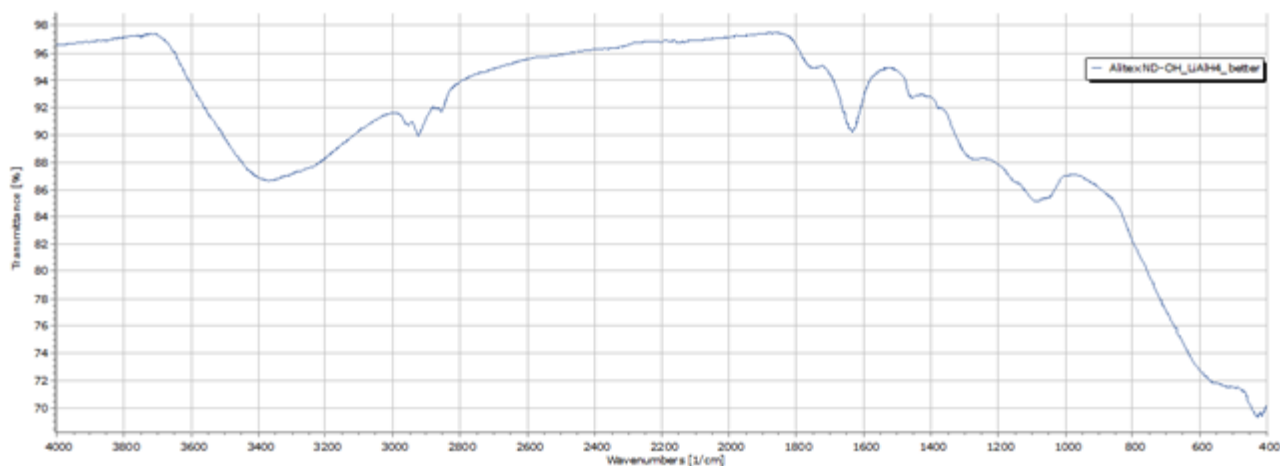
Figure 7-38. Espectro de infravermelho do ND-OH
Table 7-7. Potencial Zeta medidos para ND-OH

Potencial Zeta	ND-OH
1	-44,9 mV
2	-46,0 mV
3	-44,7 mV
4	-47,3 mV

A medida de DLS também foi realizada, entretanto observou-se um aumento significativo do diâmetro da nanopartícula para 270 nm.

7.5. WP5. Immobilization of functional groups on ND surface. Functionalization the particles modified with photoactive linkers

7.5.1. Funcionalização do ND-OH

A primeira estratégia

A primeira estratégia consistiu na imobilização do 1,2,4-triazol através de uma reação de esterificação. Desta forma, o ácido carboxílico presente no triazol pode ser ativado por uma carbodiimida e ser reativa frente a nucleófilos. Preparou-se uma suspensão de ND- OH em DMF e sonificou-se por 40 minutos, em seguida, uma solução do composto **7**, na presença de EDC e DMAP em DMF foi adicionada e mantida sob agitação a 80 °C por 24 horas (Equation 10).[16]
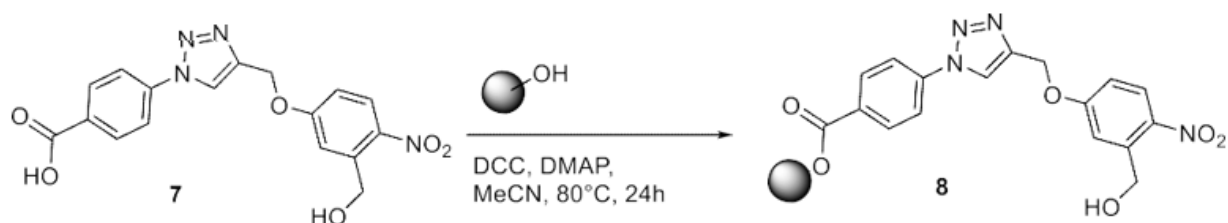
Equation 10. Tentativa de imobilização do 1,2,4-triazol em ND-OH

O solvente da suspensão foi removido sob pressão reduzida e o sólido obtido foi lavado em um *Soxhlet* por 5 dias utilizando metanol como solvente e posteriormente, acetato de etila para remover as impurezas orgânicas. O sólido foi então secado em alto vácuo e analisado por infravermelho e pôde-se observar uma quantidade muito grande de resíduos que não foram possíveis de serem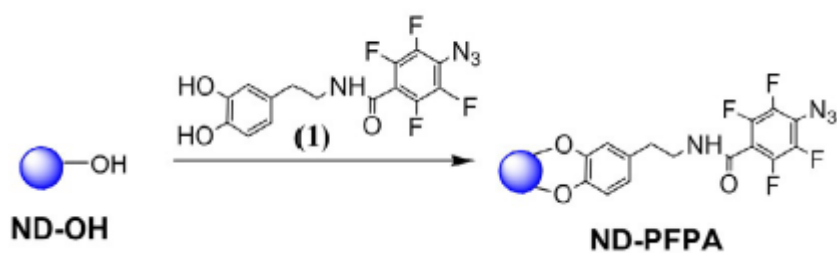 removidos, além da baixa solubilidade do triazol na maioria dos solventes orgânicos ser um problema para a implementação desta metodologia.

A segunda estratégia

Igualmente outros compostos com azida aromática perfluorada (Equation 8) foram imobilizados em ND-OH, como é ilustrado no Equation 11.

Equation 11 Immobilization of aromatic azid om ND-OH surface

The FTIR spectrum of the ND-OH shows a broad peak at 3447 cm^{-1} assigned to the vibration of surface hydroxyl groups or/and adsorbed water molecules, and an additional sharper one at 1633 cm^{-1} due to the bending mode d(OH) of surface hydroxyl groups on the NDs. In addition, the band at 1107 cm^{-1} is indicative of the presence of C-O-C- functional groups of cyclic ethers. After reaction of ND-OH particles with ligand a new vibration peak at 2125 cm^{-1} characteristic of the ν_{as}(N3) stretching appears. The C-H stretching vibration modes are detected at 2850–2970 cm^{-1} and are partially masked by the large band at 3447 cm^{-1}. The ND-PFPA particles display in addition a band at 2125 cm^{-1} characteristic of the ν_{as}(N3) stretching mode and a band at 2936 cm^{-1} characteristic of the presence of C-H bonds. The band at 1546 cm^{-1} is most likely associated with the -NH-C=O bond present in ligand.

The presence of the azide group on ND-PFPA is in addition confirmed by the N^{1s} high resolution XPS spectrum (Figure 7-39). Bands at 405.2 (Ar-N=N$^+$=N-) and 401.9 eV (Ar-N=N$^+$=N-), characteristic for the -N$_3$ groups, are observed.
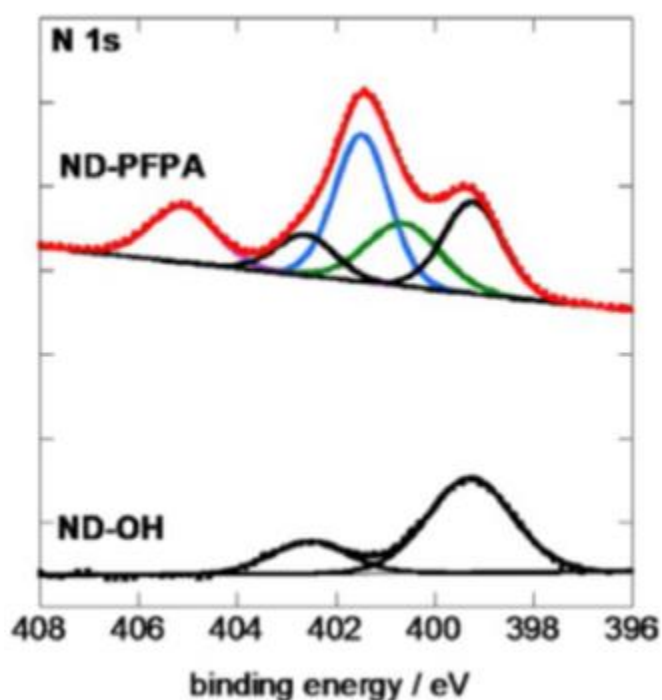
Figure 7-39. N^{1s} high resolution XPS spectra of ND-OH (black) and ND-PFPA (red), Equation 11

The contribution of the -NH-C=O linkage is seen at 400.6 eV. Bands at 402.7 and 399.2 eV are also observed in the initial ND-OH. These correspond most likely to nitrogen functions such as N-O and C-N most likely generated during the detonation process of trinitrotoluene with formation of NDs. As seen in Table 7-8, the nitrogen content accounts for 1.5 at% and might be responsible for the positive surface potential of ND-OH, as also reported by others. The level of N^{1s} is increased in ND-PFPA particles to 8.4 at % with a F/(N-1.5) ratio of 1.28, close to the theoretical value of 1.33.

Table 7-8. Physical properties of the NDs modified with PFPA ligands (Equation 11).

NDs	Diameter, nm	PDI[a]	Zeta Potential, mV	N[b], %	F[b], %
ND-OH	79±13	0.246±0.002	35±2	1.5	0.0
NDPFPA	126±3	0.168±0.021	34± 2	8.4	6.9

- a Polydispersity index, -b Atomic percent according to XPS spectrum

A terceira estratégia

A terceira estratégia consistiu em imobilizar a azida na superfície do ND-OH e em seguida, prosseguir com a reação de *click chemistry* (Equation 12).[16]

Equation 12. Imobilização do grupo fotorrremovível em duas etapas: obtenção da azida seguida de click chemistry

Em ambas as etapas, a suspensão foi centrifugada a 12 mil rpm e lavada exaustivamente com água, para remover as impurezas inorgânicas, metanol e acetonitrila para remover as impurezas orgânicas e novamente foram centrifugadas. O sólido obtido foi secado em alto vácuo e caracterizado por infravermelho (Figura 23).
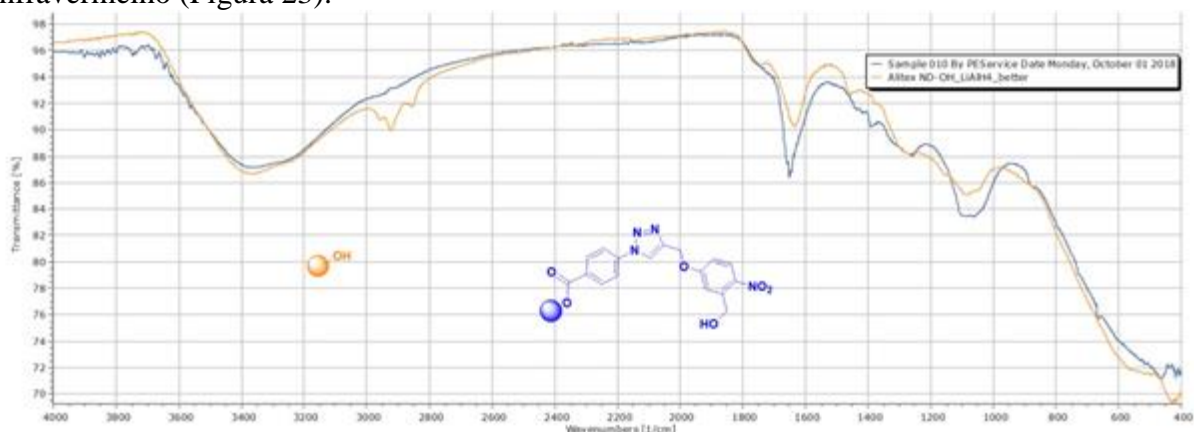
Figure 7-40. Espectro de infravermelho comparativo entre ND-OH (laranja) e ND-PPG
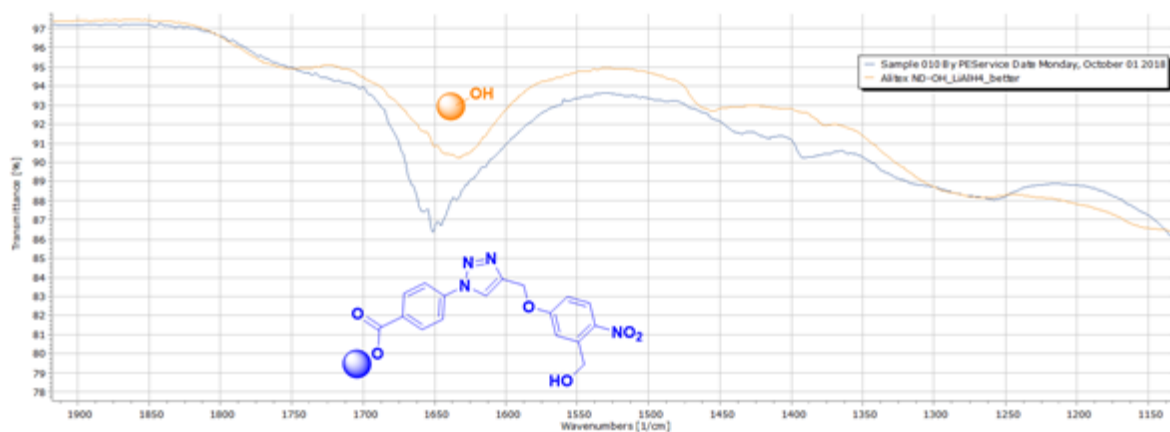
Figure 7-41. Expansão da região entre 1900 e 1150 cm^{-1}

Pela análise das bandas apresentaram, pôde-se observar um aumento na região entre 1700 a 1600 cm^{-1}, o que indica o aparecimento de uma banda C=N, presente no triazol.

7.5.2. Funcionalização do ND-COOH

A primeira etapa consistiu na reação de amidação entre o ND-COOH e a *p*-propargil anilina. A metodologia consistiu na preparação de uma suspensão de 15 mg de ND-COOH em THF (3 mg/mL, previamente sonificado por 40 minutos). Em seguida, adicionou-se uma solução de THF contendo EDC (0,22 mmol) como ativador de ácido carboxílico, DMAP (0,066 mmol) como base. A mistura reacional foi mantida sob agitação vigorosa por 48 h à temperatura ambiente).
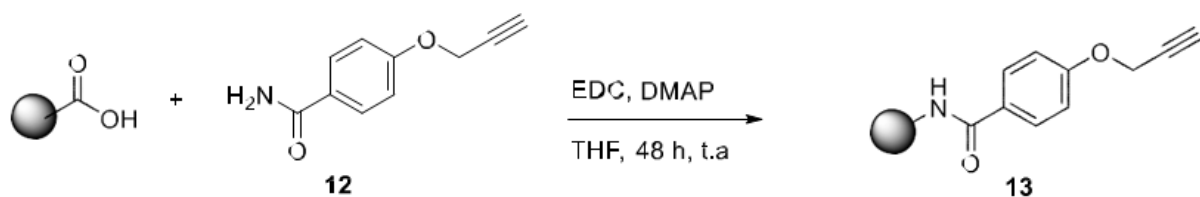
Equation 13. Imobilização da anilina através da reação de amidação com ND-COOH

Pela análise do espectro de infravermelho, pôde-se observar o aparecimento de uma banda característica de alcino na região de 2100 cm^{-1}, um deslocamento sutil na região de estiramento de carbonilas, 1781 cm^{-1} referente à C=O da amida formada.
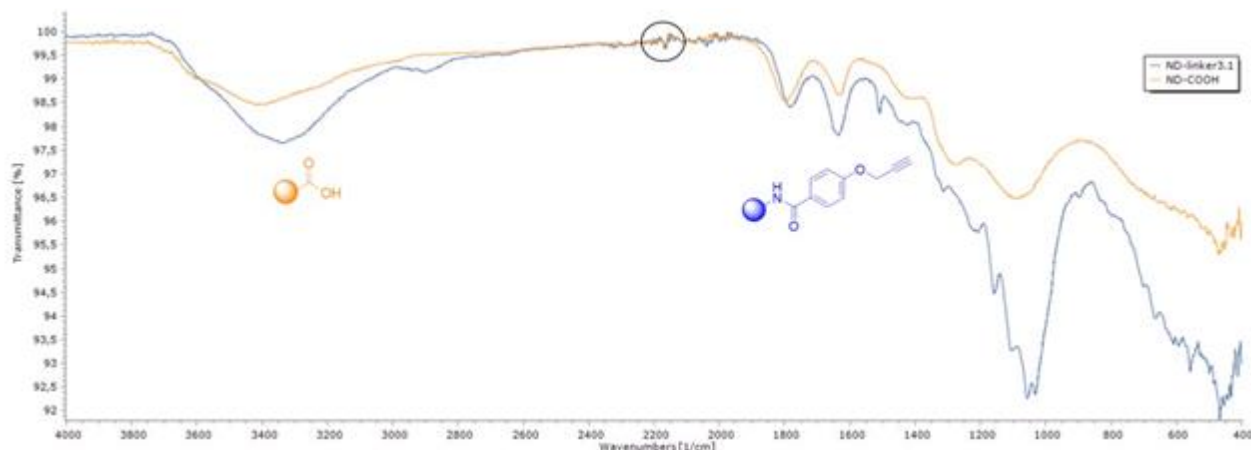
Figure 7-42. Espectro de infravermelho comparativo entre ND-Alkynyl (azul) e ND-COOH (laranja)

O alcino imobilizado na superfície dos NDs podem ser imobilizados utilizando grupos fotorremovíveis contendo azida (PPG-N₃).

7.6. WP6. Biomedical application of NDs

To apply NDs in biotechnology they have to be in form of suspension in water and better in physiological solution. Such suspensions have to be stable. It was demonstrated earlier that stability of NS suspensions varied a lot and depends from many factors such as: particle size, charge, surface chemistry, etc. Therefore, suspension stability has to be studied for each sample of NDs.

7.6.1. Bio-functionalization of ND-OH

Hydroxylated nanodiamonds (ND-OH) were functionalized with azide-derivative as it is described in paragraph 7.5.1 and then by different glycans (see list below) as it is illustrated on Equation 14.
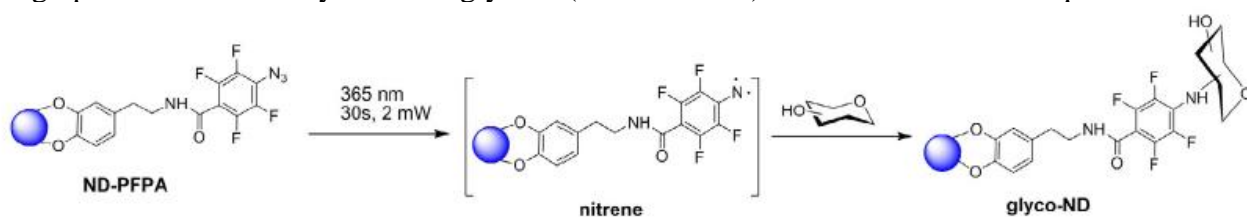
Equation 14 Immobilization of glycans on ND-PFPA

Photochemical linkage of glycans to NDs takes advantage of the photochemistry of arylazides, which upon light activation convert to reactive nitrenes (Equation 14). The highly reactive nitrenes can interact directly with any glycan through C-H and/ or N-H insertion reactions, creating highly robust covalent linkage. Mono-, di- and a polysaccharide were photochemically integrated onto ND-PFPA particles by mixing a solution of ND-PFPA in acetonitrile with aqueous solutions of the respective glycan and irradiating the mixtures at 365 nm for 30 s at 2 mW.

In FTIR spectrum of mannose and mannan-modified NDs the complete disappearance of the characteristic -N₃ vibration band at 2128 cm⁻¹, suggesting that all the azido groups were consumed in the photochemical process. The N^{1s} XPS spectra after photochemical linking of mannose also changed significantly, Figure 7-41.

monosaccharides / polysaccharides

(i) mannose (ii) glucose (iii) galactose (vii) mannan

disaccharides

(iv) lactose (v) sucrose (vi) maltose
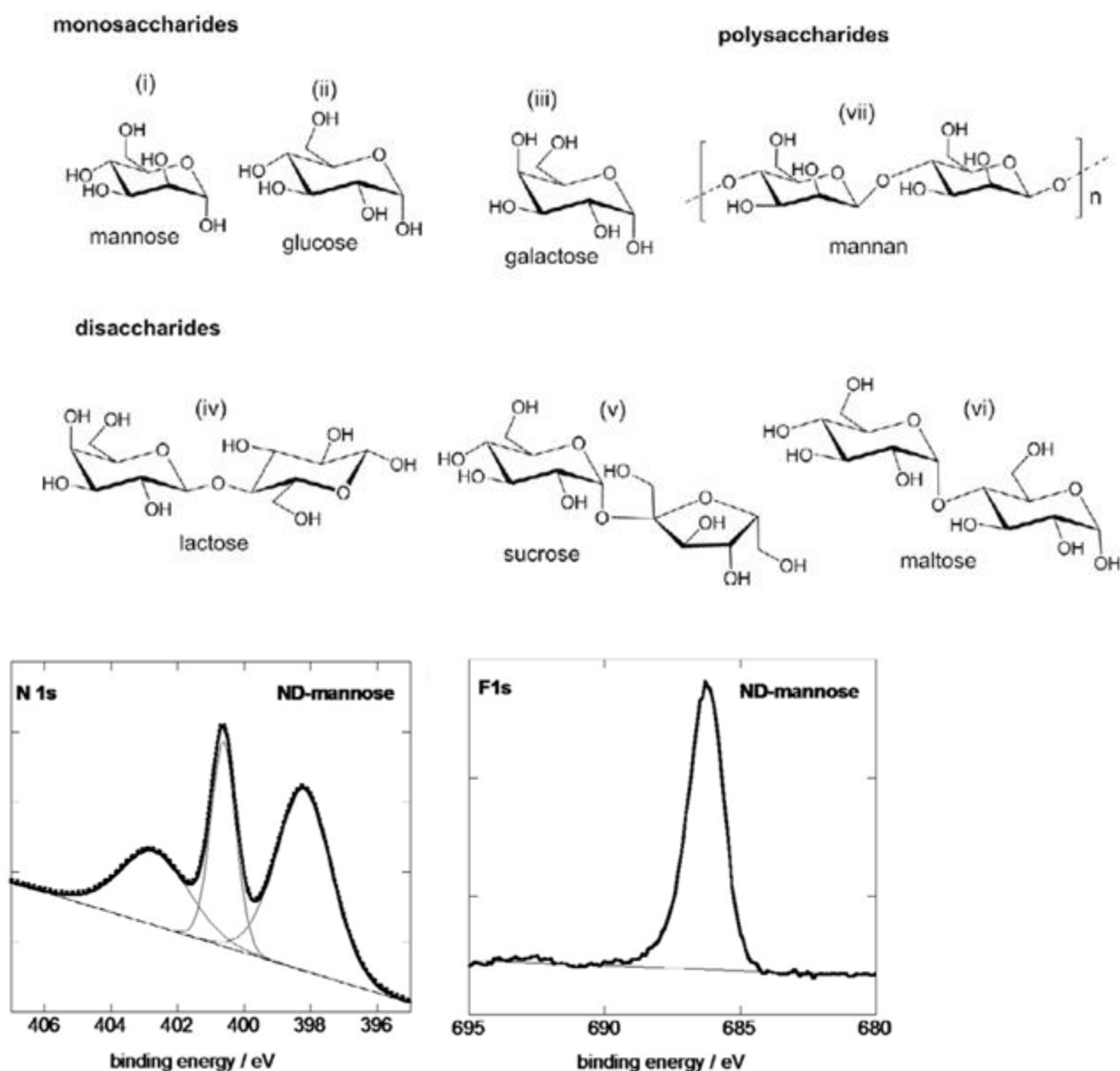
Figure 7-43. N^{1s} and F^{1s} spectrum of ND-mannoses

The conversion of the azide group into C-N bonds is evidenced by the disappearance of the bands at 405.2 (Ar-N=N$^+$=N-) and 401.9 eV (Ar-N=N$^+$=N-) and the appearance of a band at 400.6 eV due to the formation of C-N bonds. The presence of F^{1s} signal at 686 eV is an additional indication of the formation of ND-mannose (Figure 7-43). To validate further the covalent linking of the glycan to ND-PFDA, a solution of ND-PFPA in acetonitrile was mixed with an aqueous solution of mannan and left for 24 h. The characteristic -N$_3$ vibration band at 2128 cm^{-1} was still present on ND-PFPA confirming the interaction of the glycan with the dopamine ligand on the NDs.

The amount of glycan integrated onto ND-PFPA was analyzed using the well-established phenol–sulfuric acid assay and proved to be glycan dependent (Table 7-9). In the case of mannose, the sugar loading is comparable to mannose-ND formed via "click" chemistry. In the case of disaccharide-modified NDs, the amount of incorporated saccharides is about twice that of mannose, with the highest sugar loading observed for mannan-NDs.

Table 7-9. Physical properties of different glycan-NDs.

Materials	Diameter [nm]	PDI[a]	Zeta potential [mV]	Sugar loading [ug/mg ND]

mannose-NDs	127±7	0.190±0.020	32±2	95±9
glucose-NDs	104±3	0.163±0.031	28±2	89±7
galactose-NDs	113±3	0.145±0.026	30±2	96± 10
lactose-NDs	97±3	0.148±0.030	31±2	110±12
sucrose-NDs	105±3	0.159±0.026	25±2	138±15
maltose-NDs	98±3	0.167±0.024	25±2	120±15
mannan-NDs	101±3	0.187±0.025	17±2	315±20

a - Polydispersity index

7.6.2. Investigation of suspension stability of NDs and hybrid materials (with TiO_2/SiO_2) in water and in physiological solutions.

À formação de suspensões estáveis, onde a fase dispersa é composta por nanodiamantes, várias pesquisas foram didacadas, em que a modificação de superfície, estabilização estérica (com polímeros ou surfactantes) são abordagens preferíveis [1–4]. Como o foco desta seção está no envolvimento do TiO_2 como um agente anticâncer para o tratamentos clínicos avançados, neste projeto, a estabilidade de suspensões foi analisada, usando nanodiamantes comerciais cujas propriedades foram descritas na *Parte I* acima.

A titânia, o TiO_2, pode gerar um oxigênio singleto (em paralelo a outros radicais livres chamados principalmente de espécies reativas de oxigênio, ROS) com o tratamento fotoquímico [5–7]. Recentemente, foi demonstrado que o tratamento com ultra-som da mistura contendo TiO_2 pode gerar ROS em solução [8]. Levando em conta que a sonicação da solução também pode gerar $^1O_2$ em água[9], pode-se supor que as partículas de TiO_2 catalisem a geração de ROS sob sonicação.

As propriedades físico-químicas do TiO_2 são muito dependentes de sua estrutura cristalina e estrutura eletrônica e da estrutura dos sítios ativos da superfície. Por exemplo, no contexto da funcionalidade, a fase rutilo do TiO_2 é foto-inativa, e a anatase contrária pronuncia as propriedades fotocalíticas. O TiO_2 individual não é prospectivo para aplicação biomédica, pois possui baixa área superficial (5-20 m^2/g), tem tendência a aglomeração e formação de cristais inativos do tipo rutilo. No entanto, a atividade fotoativa dos nanocristais de TiO_2 pode ser estabilizada se forem distribuídos em matriz inerte (por exemplo, sílica, SiO_2). Tal material compósito SiO_2/TiO_2 pode: *a)* estabilizar a estrutura cristalina de anatase de TiO_2, e *b)* assegurar tamanho de partícula pequeno (5-10 nm) de TiO_2 para maior eficiência fotoelétrica - este óxido tem uma aplicação biomédica muito promissora para anticâncer fotodinâmico e ultrassônico terapia.

Em contraste com o TiO_2, a sílica pode formar partículas amorfas não porosas com área superficial de até 380 m^2/g ou é representada com partículas nano-porosas na área superficial até 1800 m^2/g. A combinação de óxidos de TiO_2 e SiO_2 pode contribuir para as vantagens do material híbrido de ambos os óxidos individuais: alta área superficial de sílica e atividade catalítica da titânia. Por essa razão, as metodologias de preparação e as propriedades catalíticas dos óxidos mistos de SiO_2/TiO_2 foram exaustivamente investigadas, principalmente para aplicação catalítica e óptica[10]. Por exemplo, em compostos de SiO_2/TiO_2, a fase fotoativa da titânia, anatase, é impossível no caso de mistura mecânica de óxidos individuais [11]. Outra característica importante do compósito SiO_2/TiO_2 é a estabilização de nanocristais de TiO_2 com tamanho médio de partícula de 5 nm[11]. Isto aumenta a atividade fotocatalítica global do material comparativamente a qualquer combinação de óxidos individuais e suas misturas. A maior atividade fotocatalítica do compósito SiO_2/TiO_2 foi detectada na relação Ti/Si de 70/30 [12]. Também foi reportada a relação de rutilo/anatase ótimizada na faixa de 0,43-0,33 [13–16]. A área superficial do nanocompósito SiO_2/TiO_2 é de cerca de 300 m^2/g com o diâmetro médio dos poros de 10 nm.

A estrutura porosa do compósito SiO_2/TiO_2 resultante permite a imobilização adicional de fotossensibilizadores orgânicos e inorgânicos, para aumentar a eficiência do SiO_2/TiO_2 na geração de ROS. Entre outros, o azul de metileno (MB) é um corante de baixo custo usado como protótipo de fotossensibilizador, aprovado para uso em várias outras condições clínicas, bem como terapia fotodinâmica para infecções por fungos [17].

Para uma adaptação com fisiológico, a solução de NaCl (0,9%) foi selecionada. Como eletrólito, NaCl pode suprimir a estabilidade em contraste com o meio aquoso.

Objetivo geral

O objetivo é investigar a estabilização de nanodiamantes e nanocompósitos de sílica-titânia em água e solução fisiológica (NaCl 0,9% em peso) com a caracterização de suas propriedades físico-químicas, incluindo espalhamento dinâmico de luz (DLS) e microscopia eletrônica de varredura (MEV).

Objetivos específicos

Este projeto de pesquisa tem como foco a elaboração e investigação de novos nanomateriais híbridos que podem ser utilizados na terapia fotodinâmica e sonodinâmica de câncer como transportadores ativos, que poderão liberar componentes ativos de oxigênio para o tratamento na terapia de raio-X ou sonodinâmica. Os nanomateriais propostos devem ter alta estabilidade coloidal em líquidos fisiológicos e baixa citotoxicidade. Nanocompósitos híbridos à base de NDs e nanocristais de TiO_2.

Os NDs fornecerão alta capacidade do portador para componentes ativos, estabilizarão nanopartículas de TiO_2 e aumentarão sua biocompatibilidade.

Resultados e discussões

As suspensões das nanodiamantes puros sofrem perda de estabilidade (direita), enquanto as suspensões híbridas (esquerda) revelam forte estabilização agregativa e de sedimentação dentro 24 h do exame em soro fisiológico (Figure 7-44).

0 h   *3 h*   *4h*   *24 h*
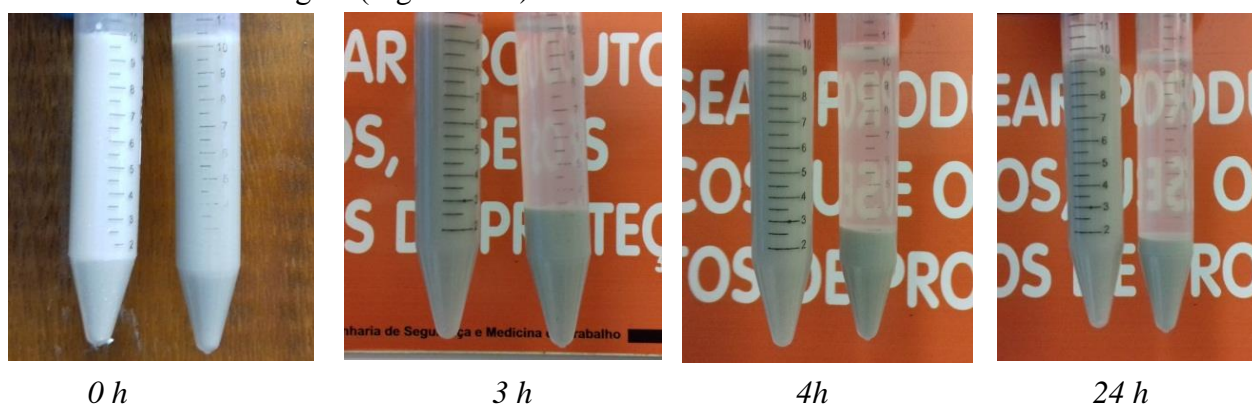
Figure 7-44. Suspensões de nanodiamantes+silica/deóxido de titânia 6% em peso (esquerda) e nanodiamante, 1% em peso (direita)

A suspensão mista possui uma interfase carregada negativa a ξ = - 28,8 mV. Ao diluir as suspensões misturadas com soro fisiológico a carga tende a zero perdendo a estabilidade agregativa devido à formação de aglomerados (Figure 7-45). No entanto, a estabilidade sedimental foi salva. Os respectivos valores do potencial zeta para as diluições de ×2 e ×4 são de -0,1 e 0,0 mV.

Figure 7-45. A distribuição do tamanho das partículas nas suspensões misturadas – antes da diluição *(a)*, a 1.25 *(b)*, 1.5 *(c)*, 2 *(d)* e 4 *(e)* vezes de diluição.

A estabilidade da suspensão foi explicada por Goncharuk *et al.* [18], apesar de seus sistemas não conterem anatase (apenas sílica pura) e, ao invés de soluções fisiológicas, os autores usaram água. Assim, podemos concluir que a presença de NaCl não neutralizou a carga nem provocou o estreitamento da dupla camada elétrica.

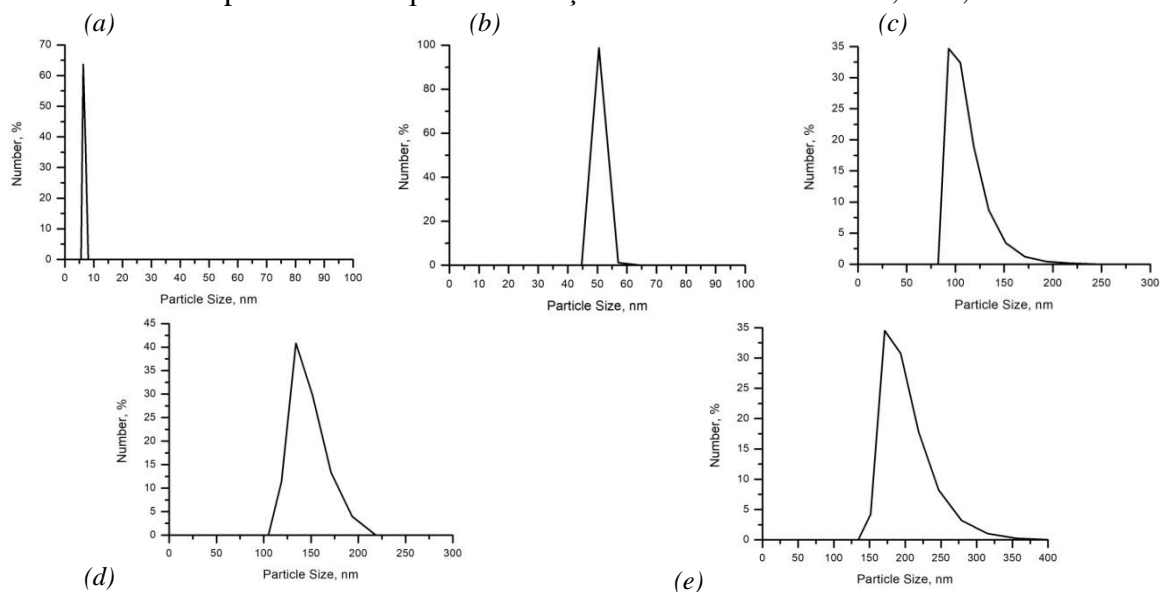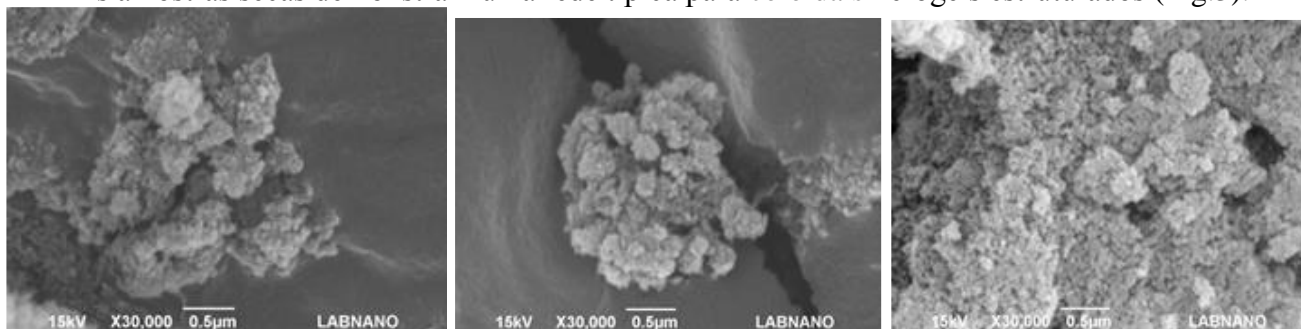As amostras secas demonstram uma rede típica para coloidais xerogéis estruturados (Fig.3).

Fig. 3. Imagens de MEV da fase sólida de NDs + sílica/titânia depois de secar as suspensões.

Esta estrutura serve como uma prova do fato que a água e mantida nos poros entre os aglomerados. Além disso, essa observação apoia a suposição que os aglomerados mistos são fortemente ligados sem separação de fases.

Parte Experimental

Os nanocompósitos de sílica/titânia foram sintetizados por Nazarkovsky e descritos antes [19]. Os nanodiamantes foram fornecidos por Ray Techniques Ltd (Israel).

A suspensão foi composta de 1% em peso de NDs e 5% em peso de compósitos de sílica-titânia suspendidos em 0,9 % em peso de solução aquosa de NaCl que foi sonicada em um processador UP200S (Hielscher) a 70% da potência nominal (200 W).

A distribuição do tamanho das partículas foi analisada em SZ-100 (HORIBA), e a microestrutura foi examinada com o auxílio do JEOL JSM-6490LV (LabNano, CBPF, Brasil).

Conclusões

Novas suspensões híbridas a 1% em peso de nanodiamantes e 5% em peso de nanocompósitos de sílica-titânia em a sulução de NaCl (0,9 % em peso) para futura aplicação biomédica de câncer.

As suspensões híbridas obtidas mostraram uma estabilidade essencial em altas concentrações da fase sólida (6% em peso) em solução fisiológica com distribuição de partículas monomodal a $d = 7,5$ nm e negativa Z-carga ($\xi = -28,8$ mV). A análise da microestrutura revelou que a fase sólida é construída na forma coloidal de xerogéis de nanodiamantes-sílica/titânia estáveis devida dos sítios ativos de ambos os materiais, envolvendo propriedades de superfície hidrofílicas e hidrofóbicas.

7.6.3.   Investigation of cellular toxicity of ND suspension.

Biocompatibility of sugar-modified NDs were studied in FioCruz. On Figure 7-46 some preliminary results of the investigation have been presented. It can be seen that ND particles (small blue dots) can penetrate to the cell without any damage of the cellular membrane
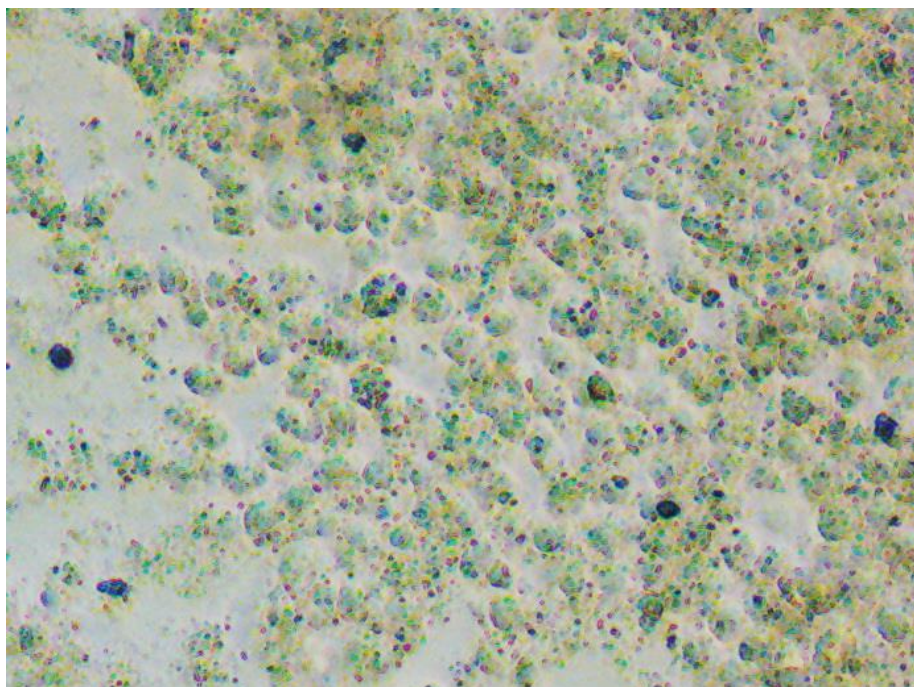
Figure 7-46. Optical microscopy of the macrophage cells J774g8 treated with ND suspension

7.6.4. Referências

1   N. Gibson, O. Shenderova, T. J. M. Luo, S. Moseenkov, V. Bondar, A. Puzyr, K. Purtov, Z. Fitzgerald and D. W. Brenner, *Diam. Relat. Mater.*, , DOI:10.1016/j.diamond.2008.10.049.

2   X. Xu, Z. Yu, Y. Zhu and B. Wang, *Diam. Relat. Mater.*, , DOI:10.1016/j.diamond.2004.11.004.

3   Y. Liu, Z. Gu, J. L. Margrave and V. N. Khabashesku, *Chem. Mater.*, 2004, **16**, 3924–3930.

4   V. N. Mochalin, O. Shenderova, D. Ho and Y. Gogotsi, *Nat. Nanotechnol.*, 2011, **7**, 11.

5   M. Buchalska, P. Labuz, Ł. Bujak, G. Szewczyk, T. Sarna, S. Maćkowski and W. Macyk, *Dalton Trans.*, 2013, **42**, 9468–75.

6   G. Munuera, A. Navio and V. Rives-Arnau, *J. Chem. Soc. Faraday Trans. 1*, 1981, **77**, 2747.

7   Y. Nosaka, T. Daimon, A. Y. Nosaka and Y. Murakami, *Phys. Chem. Chem. Phys.*, 2004, **6**, 2917.

8   K. Tachibana, H. Endo, L. B. Feril, S. M. Nejad, H. Takahashi, K. Narihira and T. Kikuta, *J. Med. Ultrason.*, 2015, **42**, 449–455.

9   Y. Matsumura, A. Iwasawa, T. Kobayashi, T. Kamachi, T. Ozawa and M. Kohno, *Chem. Lett.*, 2013, **42**, 1291–1293.

10 X. Gao and I. E. Wachs, *Catal. Today*, 1999, **51**, 233–254.

11 D. A. Kumar, J. A. Xavier, J. M. Shyla and F. P. Xavier, 2013, 3700–3707.

12 K. Y. Jung and S. Bin Park, *Appl. Catal. B Environ.*, 2000, **25**, 249–256.

13 R. J. Berry and M. R. Mueller, *Microchem. J.*, 1994, **50**, 28–32.

14 T. Ohno, K. Tokieda, S. Higashida and M. Matsumura, *Appl. Catal. A Gen.*, 2003, **244**, 383–391.

15 D. C. Hurum, A. G. Agrios, K. A. Gray, T. Rajh and M. C. Thurnauer, *J. Phys. Chem. B*, 2003, **107**, 4545–4549.

16 R. . Bacsa and J. Kiwi, *Appl. Catal. B Environ.*, 1998, **16**, 19–29.

17 M. Wainwright, D. A. Phoenix, L. Rice, S. M. Burrow and J. Waring, *J. Photochem. Photobiol. B Biol.*, 1997, **40**, 233–239.

18 O. V Goncharuk, V. I. Zarko, V. M. Bogatyrev and E. Terpilowski, K. Chibowski, *Him. Fiz. ta Tehnol. Poverhni*, , DOI:10.15407/hftp05.02.

19 M. a. Nazarkovsky, E. V Goncharuk, E. M. Pakhlov, E. I. Oranska, E. Skwarek, J. Skubiszewska-Zięba, R. Leboda, W. Janusz and V. M. Gun'ko, *Prot. Met. Phys. Chem. Surfaces*, 2013, **49**, 541–547.

8. Transfer of Knowledge

The research project brings together research centres from France, Brazil, Ukraine and USA . The project further promoted and strengthen such collaboration and stimulated cross-fertilization in the area of bio-medical applications on nanomaterials. Particularly Professor Sabine Szunerits (PVE) visited PUC-Rio and worked here for two months Also Dr. Kostiantyn Turcheniuk (France, USA), visited Rio and provided scientific advises concerning NDs properties and stabilization. PhD student Olena Artiushenko (PUC-Rio) visited Call Tech, USA (Dr. Dr. Kostiantyn Turcheniuk) to receive experimental training in nanoparticles preparation, manipulation and characterization. She also visited Ukraine (Kiev University) to learn from Prof. Sergey Alekseev experimental methodology in low-temperature SiC nanoparticles preparation. Most scientific results were obtained and published in results of such international collaboration.

8.1. Workshop

During visit of PUC-Rio. Professor Sabine Szunerits (PVE) gave two workshops for the group members and researchers of chemistry department PUC-Rio titled: 1) Modification of Nanodiamond surface, 2) Modern techniques for investigation of nanomaterials

8.2. Seminars

A comprehensive training for the project-involved stuff has been facilitated on the specific seminars dedicated to the proposed research program. The target audience of these seminars was not only the members of the research team but also staff, PhD and master students. Professor Sabine Szunerits gave a seminal titled "Diamond nanoparticles: new jewelry for chemistry, biology and medicine"

Diamond nanoparticles: new jewelry for chemistry, biology and medicine

Sabine Szunerits

Institut de Recherche Interdisciplinaire, (IRI, USR-3078), Parc de la Haute Borne, 50 avenue de Halley, BP 70478, 59658 Villeneuve d'Ascq, France
Email : Sabine.Szunerits @iri.univ-lille1.fr

Integrating biological components with nanomaterials for applications in drug delivery or medical diagnostics has been widely explored using a spectrum of approaches. Recent studies have shown that nanomaterials enabling drug delivery, such as cancer therapeutics, could revolutionize the field of pharmacology and help tackle diseases at a molecular level. Among the nanomaterials being considered, nanoscale diamond particles also referred as nanodiamonds (NDs) are very promising. This presentation will discuss the different surface functionalization strategies employed by us to make NDs suitable for biological applications. The are based on "click" chemistry approaches and the sue of dopamine derivatives. The interest of glycan-functionalized NDs as potent *E. coli* anti-adhesives will be in particular shown. Some recent results on the use of boronic acid modified NDs as potential antiviral therpatutics will be presented.
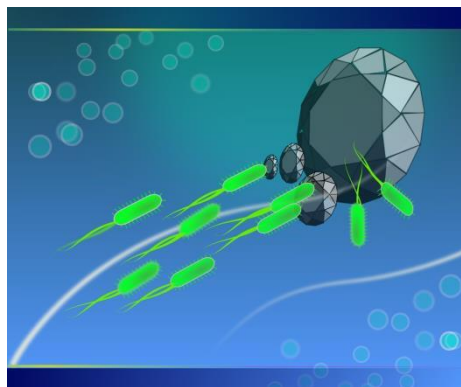
8.3. Potential to develop lasting collaboration

The IRI team (Prof S. Szunerits) is currently collaborating with Prof Volodymyr Zaitsev at PUC-Rio through a joined PhD-program (PhD student Vladimir Turcheniuk). French partner possess comprehensive knowledge in nanoparticle preparation and modification while scientists at PUC-Rio have advanced experience in chromatographic characterisation of unknown compounds. The partner in the PUC-Rio is interested in the competences of the French partner in the different use and fabrication of carbon based interfaces such as diamond, graphene, diamond nanowires, nanodiamond etc. The French team on the other hand uses currently the knowledge of the Brazilian group on the use of mass spectrometry and analytical application of nanomaterials. Professor Sabine Szunerits demonstrated great research potential. She has impressive list (more than 160) and outstanding quality of her scientific

publication. She demonstrated positive results in research collaboration with Prof Volodymyr Zaitsev and her visit to Brazil can initiate development in PUC-Rio of such an important direction – preparation and bio-analytical application of new biocompartable hybrid nanoparticles.

9. Acknowledgements

10. References

[1] C.F. van Nostrum, Polymeric micelles to deliver photosensitizers for photodynamic therapy., Adv. Drug Deliv. Rev. 56 (2004) 9–16. http://www.ncbi.nlm.nih.gov/pubmed/14706442.

[2] G. Han, P. Ghosh, V.M. Rotello, Functionalized gold nanoparticles for drug delivery, Nanomedicine. 2 (2007) 113–123. doi:10.2217/17435889.2.1.113.

[3] D. Ho, Beyond the Sparkle: The Impact of Nanodiamonds as Biolabeling and Therapeutic Agents, ACS Nano. 3 (2009) 3825–3829. doi:10.1021/nn9016247.

[4] H. Huang, E. Pierstorff, E. Osawa, D. Ho, Active Nanodiamond Hydrogels for Chemotherapeutic Delivery, Nano Lett. 7 (2007) 3305–3314. doi:10.1021/nl071521o.

[5] T. Serdiuk, S.A. Alekseev, V. Lysenko, V.A. Skryshevsky, A. Géloën, Charge-driven selective localization of fluorescent nanoparticles in live cells, Nanotechnology. 23 (2012) 315101. doi:10.1088/0957-4484/23/31/315101.

[6] R.A. Shimkunas, E. Robinson, R. Lam, S. Lu, X. Xu, X.-Q. Zhang, H. Huang, E. Osawa, D. Ho, Nanodiamond–insulin complexes as pH-dependent protein delivery vehicles, Biomaterials. 30 (2009) 5720–5728. doi:10.1016/j.biomaterials.2009.07.004.

[7] K.-K. Liu, W.-W. Zheng, C.-C. Wang, Y.-C. Chiu, C.-L. Cheng, Y.-S. Lo, C. Chen, J.-I. Chao, Covalent linkage of nanodiamond-paclitaxel for drug delivery and cancer therapy, Nanotechnology. 21 (2010) 315106. doi:10.1088/0957-4484/21/31/315106.

[8] E. Neu, C. Arend, E. Gross, F. Guldner, C. Hepp, D. Steinmetz, E. Zscherpel, S. Ghodbane, H. Sternschulte, D. Steinmüller-Nethl, Y. Liang, A. Krueger, C. Becher, Narrowband fluorescent nanodiamonds produced from chemical vapor deposition films, Appl. Phys. Lett. 98 (2011) 243107. doi:10.1063/1.3599608.

[9] M. Smet, L.-X. Liao, W. Dehaen, D. V. McGrath, Photolabile Dendrimers Using o - Nitrobenzyl Ether Linkages, Org. Lett. 2 (2000) 511–513. doi:10.1021/ol991373b.

[10] X. She, A.Q. Huang, Ó. Lucía, B. Ozpineci, Review of Silicon Carbide Power Devices and Their Applications, IEEE Trans. Ind. Electron. 64 (2017) 8193–8205. doi:10.1109/TIE.2017.2652401.

[11] A. Sanger, A. Kumar, A. Kumar, P.K. Jain, Y.K. Mishra, R. Chandra, Silicon Carbide Nanocauliflowers for Symmetric Supercapacitor Devices, Ind. Eng. Chem. Res. 55 (2016) 9452–9458. doi:10.1021/acs.iecr.6b02243.

[12] K. Koumoto, M. Shimohigoshi, S. Takeda, H. Yanagida, Thermoelectric energy conversion by porous SiC ceramics, J. Mater. Sci. Lett. 6 (1987) 1453–1455. doi:10.1007/BF01689320.

[13] J.G. KIM, Y.Y. CHOI, D.J. CHOI, J. Il KIM, B.S. KIM, S.M. CHOI, A study on the thermoelectric properties of chemical vapor deposited SiC films with temperature and diluent gases variation, J. Ceram. Soc. Japan. 117 (2009) 574–577. doi:10.2109/jcersj2.117.574.

[14] H.S. Chin, K.Y. Cheong, A.B. Ismail, A Review on Die Attach Materials for SiC-Based High-Temperature Power Devices, Metall. Mater. Trans. B. 41 (2010) 824–832. doi:10.1007/s11663-010-9365-5.

[15] K.Z. and K. Rogdakis, SiC nanowires: material and devices, J. Phys. D. Appl. Phys. 44

(2011) 133001.

[16] X. Qiang, H. Li, Y. Zhang, Z. Wang, Z. Ba, X. Zhang, Mechanical and oxidation protective properties of SiC nanowires-toughened SiC coating prepared in-situ by a CVD process on C/C composites, Surf. Coatings Technol. 307 (2016) 91–98. doi:10.1016/J.SURFCOAT.2016.08.072.

[17] C.M. Lieber, One-dimensional nanostructures: Chemistry, physics & applications, Solid State Commun. 107 (1998) 607–616. doi:10.1016/S0038-1098(98)00209-9.

[18] K.M. Prewo, J.J. Brennan, High-strength silicon carbide fibre-reinforced glass-matrix composites, J. Mater. Sci. 15 (1980) 463–468. doi:10.1007/BF00551699.

[19] P. Vijayan P, D. Puglia, A. Dąbrowska, P. Vijayan P, A. Huczko, J.M. Kenny, S. Thomas, Mechanical and thermal properties of epoxy/silicon carbide nanofiber composites, Polym. Adv. Technol. 26 (2015) 142–146. doi:10.1002/pat.3437.

[20] J.B. Casady, R.W. Johnson, Status of silicon carbide (SiC) as a wide-bandgap semiconductor for high-temperature applications: A review, Solid. State. Electron. 39 (1996) 1409–1422. doi:10.1016/0038-1101(96)00045-7.

[21] P. Käckell, B. Wenzien, F. Bechstedt, Electronic properties of cubic and hexagonal SiC polytypes from ab initio calculations, Phys. Rev. B. 50 (1994) 10761–10768. doi:10.1103/PhysRevB.50.10761.

[22] A. Qteish, V. Heine, R.J. Needs, Polarization, band lineups, and stability of SiC polytypes, Phys. Rev. B. 45 (1992) 6534–6542. doi:10.1103/PhysRevB.45.6534.

[23] M. Hofmann, A. Zywietz, K. Karch, F. Bechstedt, Lattice dynamics of SiC polytypes within the bond-charge model, Phys. Rev. B. 50 (1994) 13401–13411. doi:10.1103/PhysRevB.50.13401.

[24] S. Limpijumnong, W.R.L. Lambrecht, Total energy differences between SiC polytypes revisited, Phys. Rev. B. 57 (1998) 12017–12022. doi:10.1103/PhysRevB.57.12017.

[25] C. Persson, U. Lindefelt, Relativistic band structure calculation of cubic and hexagonal SiC polytypes, J. Appl. Phys. 82 (1997) 5496–5508. doi:10.1063/1.365578.

[26] R.A. Stein, P. Lanig, S. Leibenzeder, Influence of surface energy on the growth of 6H- and 4H-SiC polytypes by sublimation, Mater. Sci. Eng. B. 11 (1992) 69–71. doi:10.1016/0921-5107(92)90193-D.

[27] H. Nienhaus, T.U. Kampen, W. Mönch, Phonons in 3C-, 4H-, and 6H-SiC, Surf. Sci. 324 (1995) L328–L332. doi:10.1016/0039-6028(94)00775-6.

[28] G. Pensl, W.J. Choyke, Electrical and optical characterization of SiC, Phys. B Condens. Matter. 185 (1993) 264–283. doi:10.1016/0921-4526(93)90249-6.

[29] P. Pirouz, J.W. Yang, Polytypic transformations in SiC: the role of TEM, Ultramicroscopy. 51 (1993) 189–214. doi:10.1016/0304-3991(93)90146-O.

[30] P. Ščajev, M. Kato, K. Jarašiūnas, A diffraction-based technique for determination of interband absorption coefficients in bulk 3C-, 4H- and 6H-SiC crystals, J. Phys. D. Appl. Phys. 44 (2011) 365402. doi:10.1088/0022-3727/44/36/365402.

[31] A. Lohrmann, S. Castelletto, J.R. Klein, T. Ohshima, M. Bosi, M. Negri, D.W.M. Lau, B.C. Gibson, S. Prawer, J.C. McCallum, B.C. Johnson, Activation and control of visible single defects in 4H-, 6H-, and 3C-SiC by oxidation, Appl. Phys. Lett. (2016). doi:10.1063/1.4939906.

[32] A. Csóré, H.J. Von Bardeleben, J.L. Cantin, A. Gali, Characterization and formation of NV centers in 3C, 4H, and 6H SiC: An ab initio study CHARACTERIZATION and FORMATION of NV CENTERS ... CSÓRÉ, von BARDELEBEN, CANTIN, and GALI, Phys. Rev. B. (2017). doi:10.1103/PhysRevB.96.085204.

[33] W. Zhou, Y. Zhang, X. Niu, G. Min, One-Dimensional SiC Nanostructures: Synthesis and Properties, in: One-Dimensional Nanostructures, 2008. doi:10.1007/978-0-387-74132-1_2.

[34] G. Gundiah, G. V Madhav, A. Govindaraj, M.M. Seikh, C.N.R. Rao, Synthesis and characterization of silicon carbide, silicon oxynitride and silicon nitride nanowires, J. Mater. Chem. 12 (2002) 1606–1611. doi:10.1039/B200161F.

[35] T. Kimoto, A. Itoh, H. Matsunami, Step-Controlled Epitaxial Growth of High-Quality SiC Layers, Phys. Status Solidi. 202 (2001) 247–262. doi:10.1002/1521-3951(199707)202:1<247::AID-PSSB247>3.0.CO;2-Q.

[36] P. Zhang, X.L. Hou, J.L. Mi, Q. Jiang, H. Aslan, M.D. Dong, Curvature effect of SiC nanotubes and sheets for CO_2 capture and reduction, RSC Adv. 4 (2014) 48994–48999. doi:10.1039/C4RA07542K.

[37] A. Dąbrowska, A. Huczko, A. Katunin, SiC Nanofibres Produced by the Combustion Synthesis as the Nanocomposites Fillers, Macromol. Symp. 327 (2013) 94–98. doi:10.1002/masy.201350511.

[38] C. Nguyen, D.D. Do, A new method for the characterization of porous materials, Langmuir. 15 (1999) 3608–3615. doi:10.1021/la981140d.

[39] C. Nguyen, D.D. Do, Effects of Probing Vapors and Temperature on the Characterization of Micro-Mesopore Size Distribution of Carbonaceous Materials, Langmuir. 16 (2000) 7218–7222. doi:10.1021/la991596a.

[40] V.M. Gun'ko, Composite materials: Textural characteristics, Appl. Surf. Sci. 307 (2014) 444–454. doi:https://doi.org/10.1016/j.apsusc.2014.04.055.

[41] V.M. Gun'ko, D.D. Do, Characterisation of pore structure of carbon adsorbents using regularisation procedure, Colloids Surfaces A Physicochem. Eng. Asp. 193 (2001) 71–83. doi:https://doi.org/10.1016/S0927-7757(01)00685-9.

[42] S.W. Provencher, A constrained regularization method for inverting data represented by linear algebraic or integral equations, Comput. Phys. Commun. 27 (1982) 213–227. doi:https://doi.org/10.1016/0010-4655(82)90173-4.

[43] S.W. Provencher, CONTIN: A general purpose constrained regularization program for inverting noisy linear algebraic and integral equations, Comput. Phys. Commun. 27 (1982) 229–242. doi:https://doi.org/10.1016/0010-4655(82)90174-6.

[44] J. Choma, M. Jaroniec, Energetic and Structural Heterogeneity of Synthetic Microporous Carbons, Langmuir. 13 (1997) 1026–1030. doi:10.1021/la950959d.

[45] C.P. Jaroniec, M. Jaroniec, M. Kruk, Comparative studies of structural and surface properties of porous inorganic oxides used in liquid chromatography, J. Chromatogr. A. 797 (1998) 93–102. doi:https://doi.org/10.1016/S0021-9673(97)00998-9.

[46] V. Gun'ko, T.J. Bandosz, Heterogeneity of adsorption energy of water, methanol and diethyl ether on activated carbons: effect of porosity and surface chemistry, Phys. Chem. Chem. Phys. 5 (2003) 2096–2103. doi:10.1039/B301399P.

[47] J.R. Guth, W.T. Petuskey, Silicon-29 magic-angle-spinning NMR characterization of silicon carbide polytypes, J. Phys. Chem. 91 (1987) 5361–5364. doi:10.1021/j100304a044.

[48] G.-Q. Jin, X.-Y. Guo, Synthesis and characterization of mesoporous silicon carbide, Microporous Mesoporous Mater. 60 (2003) 207–212. doi:https://doi.org/10.1016/S1387-1811(03)00378-0.

[49] P. Klán, T. Šolomek, C.G. Bochet, A. Blanc, R. Givens, M. Rubina, V. Popik, A. Kostikov, J. Wirz, Photoremovable Protecting Groups in Chemistry and Biology: Reaction Mechanisms and Efficacy, Chem. Rev. 113 (2013) 119–191. doi:10.1021/cr300177k.

[50] M. Skwarczynski, M. Noguchi, S. Hirota, Y. Sohma, T. Kimura, Y. Hayashi, Y. Kiso,

Development of first photoresponsive prodrug of paclitaxel, Bioorg. Med. Chem. Lett. 16 (2006) 4492–4496. doi:10.1016/j.bmcl.2006.06.030.

[51] V.N. Mochalin, O. Shenderova, D. Ho, Y. Gogotsi, The properties and applications of nanodiamonds, Nat. Nanotechnol. 7 (2012) 11–23. doi:10.1038/nnano.2011.209.

[52] S. Nazir, T. Hussain, A. Ayub, U. Rashid, A.J. MacRobert, Nanomaterials in combating cancer: therapeutic applications and developments., Nanomedicine. 10 (2014) 19–34. doi:10.1016/j.nano.2013.07.001.